

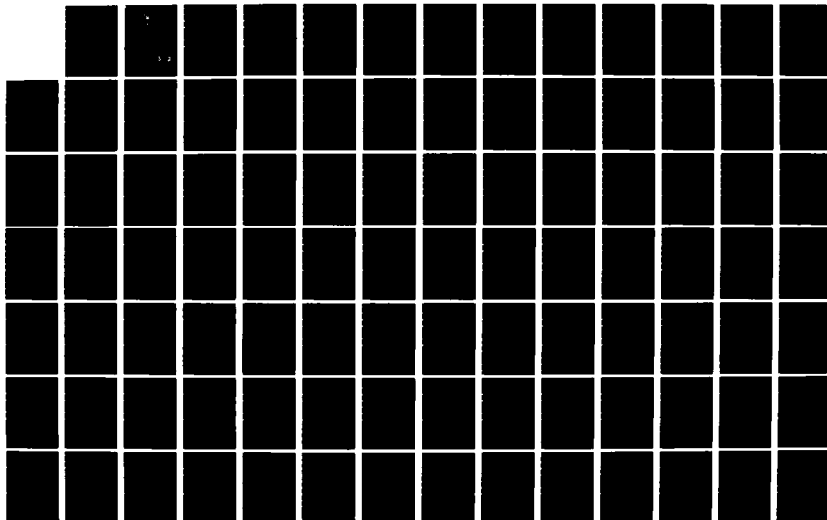
AD-A124 739

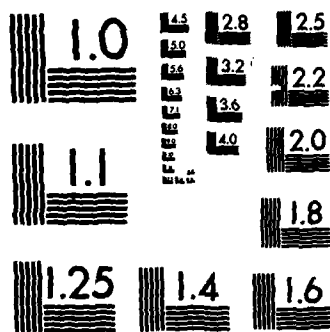
A PARAMETRIC STUDY OF SURFACE IMPERFECTIONS AND SMALL
CUTOUTS IN A COMPOSITE PANEL(U) AIR FORCE INST OF TECH
WRIGHT-PATTERSON AFB OH SCHOOL OF ENGI. T C JANISSE
DEC 82 AFIT/GRE/AA/82D-15 F/G 12/1

1/2

UNCLASSIFIED

NL

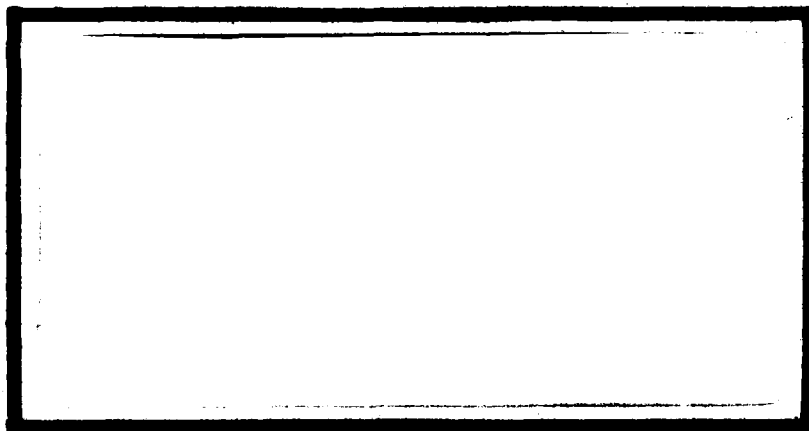




MICROCOPY RESOLUTION TEST CHART
NATIONAL BUREAU OF STANDARDS-1963-A

①

AD A124739



DTIC
ELECTE
FEB 22 1983
S D E

DEPARTMENT OF THE AIR FORCE
AIR UNIVERSITY (ATC)

AIR FORCE INSTITUTE OF TECHNOLOGY

Wright-Patterson Air Force Base, Ohio

This document has been approved
for public release and sales in
distribution is unlimited.

88 02 022123

A PARAMETRIC STUDY OF SURFACE
IMPERFECTIONS AND SMALL CUTOUTS
IN A COMPOSITE PANEL

THESIS

AFIT/GAE/AA/82D-15 Thomas C. Janisse
Capt. USAF

DTIC
SELECTE
FEB 2 1983
S D
E

This document has been approved
for public release and sale; its
distribution is unlimited.

AFIT/GAS/AA/82D-15

A PARAMETRIC STUDY OF SURFACE
IMPERFECTIONS AND SMALL CUTOUTS
IN A COMPOSITE PANEL

THESIS

Presented to the Faculty of the School of Engineering
of the Air Force Institute of Technology
Air University
in Partial Fulfillment of the
Requirements for the Degree of
Master of Science

by

Thomas C. Janisse, B.S.
Capt USAF



Accession For	
NTIS GRA&I	<input checked="checked" type="checkbox"/>
DTIC TAB	<input type="checkbox"/>
Unannounced	<input type="checkbox"/>
Justification	
By _____	
Distribution/ _____	
Availability Codes	
Dist	Avail and/or Special
A	

Graduate Aeronautical Engineering

December 1982

Approved for public release; distribution unlimited.

ACKNOWLEDGEMENTS

I wish to express my sincere gratitude to Dr. A. N. Palazotto for the sharing of his time with me and the guidance he gave during this course of study. Thanks also goes to Dr. N. S. Khot for providing the unlimited amount of computer resources needed to complete a project of this magnitude. I also wish to thank Maj. M. M. Wallace for providing the office space and large table needed to study the hundreds of plots and massive computer runs.

Most of all, I wish to thank my wife, Donna, and my sons, Kyle and Philip, for giving up their time with me so that I could complete this research. Without their love and encouragement, this project would have been impossible to complete.

Thomas C. Janisse

Table of Contents

	Page
ACKNOWLEDGEMENTS	ii
LIST OF FIGURES	v
LIST OF TABLES	ix
ABSTRACT	x
I. INTRODUCTION	1
Background	1
Approach	2
II. THEORY	3
Basic Theory	3
Nonlinear Solution Algorithm Theory	12
III. MODELLING	18
Panel Properties	18
Element Selection	20
Grid Selection	22
IV. DISCUSSION AND RESULTS	26
411 Element	26
Analytical Model Versus Experimental Study	27
Analytical Imperfection Study	37
Analytical Study of Panels With Cutouts	67
Experimental Analysis Versus Analytical Study	119
V. CONCLUSIONS	131
BIBLIOGRAPHY	134

	Page
APPENDIX A	138
APPENDIX B	150
VITA	153

LIST OF FIGURES

Figure	Page
1. Positive Forces and Moments Acting on a Laminate	8
2. Geometry of an N Layered Laminate	9
3. Residual Forces Versus Assumed Displacements .	14
4. Nonlinear Solution Algorithm	17
5. Panel Notation	19
6. Element DOF	21
7. Grid Selection Data	23
8. Convergence Study for Cutout Panel	24
9. Load Versus Top Edge Displacement On BCP 9824-A-31-AS Panel	29
10. W Component Displacement Contours	30
11. W Component Displacement Contours	32
12. W Component Displacement Contours	33
13. M_x at Different Load Levels	34
14. Relative Load Versus Relative Displacement . .	39
15. Relative Load Versus Relative Displacement . .	40
16. W Component Displacement Contours	43
17. W Component Displacement Contours	44
18. W Component Displacement Contours	45
19. W Component Displacement Contours	46
20. W Component Displacement Contours	47
21. W Component Displacement Contours	48

Figure		Page
22.	Maximum Radial Displacement Versus Top Edge Load $[90, 0]_{2s}$	50
23.	Maximum Radial Displacement Versus Top Edge Load $[90, 0]_{2s}$	51
24.	Maximum M_x Resultant Versus Top Edge Load	53
25.	Maximum M_y Resultant Versus Top Edge Load	54
26.	Maximum M_x Resultant Versus Top Edge Load	55
27.	Maximum M_y Resultant Versus Top Edge Load	56
28.	Linear and Nonlinear Moment Resultants	57
29.	M_x Moment Resultant Versus Top Edge Load	60
30.	M_y Moment Resultant Versus Top Edge Load	61
31.	Eigenvector Contours	63
32.	Eigenvector Contours	64
33.	Top edge Load Versus Top Edge Displacements	69
34.	W Component Displacement Contours	74
35.	W Component Displacement Contours	75
36.	W Component Displacement Contours	76
37.	W Component Displacement Contours	77
38.	W Component Displacement Contours	78
39.	Radial Displacement Profiles	81
40.	Radial Displacement Profiles	82
41.	Radial Displacement Profiles	83

Figure		Page
42.	Radial Displacement Profiles	84
43.	Radial Displacement Profiles	85
44.	Radial Displacement Contours	86
45.	Moment Resultant Profiles	88
46.	Moment Resultant Profiles	89
47.	Moment Resultant Profiles	90
48.	Moment Resultant Profiles	91
49.	Moment Resultant Profiles	92
50.	Moment Resultant Profiles	93
51.	Moment Resultant Profiles	94
52.	Moment Resultant Profiles	95
53.	Moment Resultant Profiles	96
54.	Moment Resultant Profiles	97
55.	Moment Resultant Profiles	98
56.	Moment Resultant Profiles	99
57.	Moment Resultant Profiles	100
58.	Moment Resultant Profiles	101
59.	Moment Resultant Profiles	102
60.	Moment Resultant Profiles	103
61.	Eigenvector Contours	106
62.	Eigenvector Contours	107
63.	W Component Displacement Contours	109
64.	W Component Displacement Contours	110
65.	W Component Displacement Contours	111

Figure		Page
66.	W Component Displacement Contours	112
67.	Eigenvector Contours	114
68.	W Component Displacement Contours	117
69.	W Component Displacement Contours	118
70.	Experimental Setup	120
71.	Radial Displacements of Panel at Collapse . .	121
72.	Load Versus Top Edge Displacement	123
73.	Load Versus Radial Displacement	124
74.	Load Versus Radial Displacement	125
75.	Load Versus Radial Displacement	126
76.	Load Versus Radial Displacement	127
77.	Load Versus Radial Displacement	130

LIST OF TABLES

Tables	Page
1. Imperfection Patterns	37
2. Linear Versus Nonlinear Comparison	58
3. Ply Layup and Cutout Size	67

Abstract

A finite element computer code, STAGS C-1, was used to study the effects surface imperfections and cutouts have on the load bearing capability and the displacement patterns of a graphite-epoxy panel. A nonlinear collapse analysis was conducted on two different ply layups each with five different surface imperfection patterns. In addition three different ply orientations were studied each having two different size cutouts (a two inch by two inch square and a four inch by four inch square).

The nonlinear branch of STAGS C-1 uses a energy technique using the nonlinear stiffness matrix that was generated by using the Sanders' strain displacement equations. STAGS did a very good job in calculating the collapse load and displacements of a panel with surface imperfections when compared with an experimentally tested panel.

It was found that as the number of surface imperfections is increased, the collapse load decreases until there are nine surface waves. After that, the collapse load increases with increasing imperfections. An imperfection pattern that models the linear bifurcation eigenvector did not have the lowest collapse load as was believed. The displacement pattern followed the initial surface imperfections in all cases.

The collapse characteristics of composite panels are dependent on the ply layup and size of the cutout. Small cutouts had a displacement pattern that was not expected and is different than the larger cutouts. Changing the vertical boundary conditions on the panel with the small cutout had a negligible effect.

INTRODUCTION

Background

Composite materials are being used more frequently in the aircraft industry. Because of their high strength to weight ratio when compared to conventional materials, composite materials are proving to be invaluable in the design and manufacture of high performance aircraft. However, in order to use composite materials in the aircraft industry, a higher level of understanding of the materials behavior and the effects of imperfections and cutouts will have to be known.

Various studies have been done on the buckling of composite panels and plates under axial compression both experimentally and analytically [1-11]. In the analytical studies done, the authors in references [1-7] assumed no surface imperfections in the panels. However, they stated in their work that composite panels are very sensitive to surface imperfections. This imperfection sensitivity was demonstrated both analytically and experimentally by Bauld et. al. in references [8-11]. In the analytical studies referenced with surface imperfections, all imperfections were axially symmetric. Bauld, in his experimental study for the Air Force Flight Dynamic Lab [10], actually measured surface imperfections on graphite epoxy panels, and tested them to the collapse load.

Therefore, little is known about how different surface imperfections affect the behavior of composite panels.

Very little information on composite panels with cutouts could be found. There have been studies done on cutout reinforcement in composite shells [12] and two studies by Starnes et.al. have been done on flat rectangular graphite-epoxy plates with either surface damage or cutouts [13,14]. No studies were found relating the effect of cutouts on curved composite panels. Thus, in order to use composite panels in the aircraft industry, a greater understanding of the effect of surface imperfections and cutouts on a composite panel is needed. This thesis is an attempt to bring a greater understanding to this area.

Approach

A nonlinear analysis using the STAGS C-1 computer code has been used. A nonlinear analysis was chosen for two reasons. First, an imperfection on the surface of a panel is a true geometric imperfection. In order to handle this satisfactorily, a nonlinear analysis must be performed. Secondly, a cutout produces a geometric discontinuity within the panel. Therefore, in both situations a nonlinear solution algorithm will have to be used.

The imperfections are going to be input using features built into STAGS. Thus, the imperfections that are incorporated become more abstract than discrete. They will be

symmetric about a point and will be described as sine waves with given maximum amplitudes and wavelengths generating vertically and horizontally from a specified point. This type of imperfection is more design oriented and can be measured as the variance in the surface of a composite panel. Experimental comparisons have been carried out for a panel whose surface imperfections were measured and tested. An analytical study has also been carried out on the effect of various shapes of surface imperfections on a composite panel.

After completing the surface imperfection portion, a study has been made on the effect of ply layup and cutout size. The cutouts considered are located at the center of the panel. Two different size cutouts have been studied with three different composite panel ply orientations. Also, an experimental investigation has been conducted on panels with small cutouts to verify the results of the analytical study.

THEORY

Basic Theory

STAGS is a computer code developed by B. O. Almroth, F. A. Brogan, and G. M. Stanley of the Lockheed Palo Alto Research Laboratory for the structural analysis of general shells. The code was originally developed in 1967 using finite differences and was sponsored by the Lockheed Missile and Space Company [15]. There have been many revisions and

improvements added since the initial development. The current version C-1 (last revised in 1979) is an energy based finite element code using the Kirchhoff-Love hypothesis [16, 17]. This thesis is investigating the static nonlinear collapse of composite panels. Therefore, the problem is that of satisfying the equations of static equilibrium.

$$\Sigma F = 0 \quad (1)$$

With the sum of the forces equal to zero, the total potential energy must be stationary and the first variation of potential energy will equal zero. The total potential energy of a body is the strain energy of the body minus the work done on the body.

$$V = U - W \quad (2)$$

The work done on the body is the sum of the displacements times the externally applied forces.

$$W = \{X\}^T \{F\} \quad (3)$$

$\{X\}$ is the vector of displacements and

$\{F\}$ is the vector of externally applied forces.

The strain energy of a body is [18]

$$U = \frac{1}{2} \int_{\text{Volume}} (\sigma_x \epsilon_x + \sigma_y \epsilon_y + \tau_{xy} \gamma_{xy}) d\text{Volume}. \quad (4)$$

STAGS uses the strain displacement relations based on the middle surface kinematic relations of the Sanders' equations.

Therefore, the midsurface strains are [9]

$$\epsilon_x^0 = U_{,x} + \frac{1}{2} \phi_x^2 - W_{0,x} \phi_x \quad (5)$$

$$\epsilon_y^0 = V_{,y} + \frac{W}{R} + \frac{1}{2} \phi_y^2 - \frac{1}{2} \phi^2 - W_{0,x} \phi_y \quad (6)$$

$$2\epsilon_{xy}^0 = V_{,x} + U_{,y} + \phi_x \phi_y - W_{0,y} \phi_y - W_{0,y} \phi_x \quad (7)$$

and the midsurface curvature are

$$\kappa_x = \phi_{x,y} \quad (8)$$

$$\kappa_y = \phi_{y,y} \quad (9)$$

$$2\kappa_{xy} = 2\kappa_{yx} = \phi_{y,x} + \phi_{x,y} + \phi/R \quad (10)$$

where ϕ_x , ϕ_y , and ϕ are the components of rotation about the coordinate lines and about the normal to the surface. The rotations in terms of the displacement are

$$\phi_x = -W_{,x} \quad (11)$$

$$\phi_y = -W_{,y} + V/R \quad (12)$$

$$\phi = \frac{1}{2} (V_{,x} - U_{,y}) \quad (13)$$

In equations 5-13, w_0 is the initial geometric imperfection and R is the radius of curvature. By knowing the middle surface strains and curvatures and using the Kirchhoff-Love hypothesis, the corresponding strain at any point in the panel can be found.

$$\begin{bmatrix} \epsilon_x \\ \epsilon_y \\ \gamma_{xy} \end{bmatrix} = \begin{bmatrix} \epsilon_x^0 \\ \epsilon_y^0 \\ \gamma_{xy}^0 \end{bmatrix} + z \begin{bmatrix} \kappa_x \\ \kappa_y \\ \kappa_{xy} \end{bmatrix} \quad (14)$$

Further, using the orthotropic stress-strain relations, the stresses for any layer of a composite panel can be found [18].

$$\begin{bmatrix} \sigma_x \\ \sigma_y \\ \tau_{xy} \end{bmatrix}_k = \begin{bmatrix} \bar{Q} \end{bmatrix}_k \begin{bmatrix} \epsilon_x \\ \epsilon_y \\ \gamma_{xy} \end{bmatrix}_k \quad (15)$$

or using the midsurface strains and curvatures

$$\begin{bmatrix} \sigma_x \\ \sigma_y \\ \tau_{xy} \end{bmatrix}_k = \begin{bmatrix} \bar{Q} \end{bmatrix}_k \begin{bmatrix} \epsilon_x^0 \\ \epsilon_y^0 \\ \gamma_{xy}^0 \end{bmatrix} + z_k \begin{bmatrix} \bar{Q} \end{bmatrix}_k \begin{bmatrix} \kappa_x \\ \kappa_y \\ \kappa_{xy} \end{bmatrix} \quad (16)$$

where $[\bar{Q}]_k$ is the transformed reduced stiffness matrix and is composed of

$$\begin{bmatrix} \bar{Q} \end{bmatrix}_k = \begin{bmatrix} \bar{Q}_{11} & \bar{Q}_{12} & \bar{Q}_{16} \\ & \bar{Q}_{22} & \bar{Q}_{26} \\ \text{sym} & & \bar{Q}_{66} \end{bmatrix}_k \quad (17)$$

in which

$$\bar{Q}_{11} = Q_{11}c^4 + 2(Q_{12} + 2Q_{66})s^2c^2 + Q_{22}s^4 \quad (18)$$

$$\bar{Q}_{12} = (Q_{11} + Q_{22} - 4Q_{66})s^2c^2 + Q_{12}(s^4 + c^4) \quad (19)$$

$$\bar{Q}_{22} = Q_{11}s^4 + 2(Q_{12} + 2Q_{66})s^2c^2 + Q_{22}c^4 \quad (20)$$

$$\bar{Q}_{16} = (Q_{11} - Q_{12} - 2Q_{66})sc^3 + (Q_{12} - Q_{22} + 2Q_{66})s^3c \quad (21)$$

$$\bar{Q}_{26} = (Q_{11} - Q_{12} - 2Q_{66})sc^3 + (Q_{12} - Q_{22} + 2Q_{66})sc^3 \quad (22)$$

$$\bar{Q}_{66} = (Q_{11} - Q_{22} - 2Q_{16} - 2Q_{66})s^2c^2 + Q_{66}(s^4 + c^4) \quad (23)$$

where $S = \sin \theta$ and $C = \cos \theta$

and

$$Q_{11} = E_1/(1 - \nu_{21}\nu_{12}) \quad (24)$$

$$Q_{12} = \nu_{12}E_2/(1 - \nu_{12}\nu_{21}) = \nu_{21}E_1/(1 - \nu_{12}\nu_{21}) \quad (25)$$

$$Q_{22} = E_2/(1 - \nu_{12}\nu_{21}) \quad (26)$$

$$Q_{66} = G_{12} \quad (27)$$

The resultant laminate forces and moments can be found from the appropriate stress components. (See Figure 1 for sign notation for the forces and moments and Figure 2 for the geometry of the laminate.)

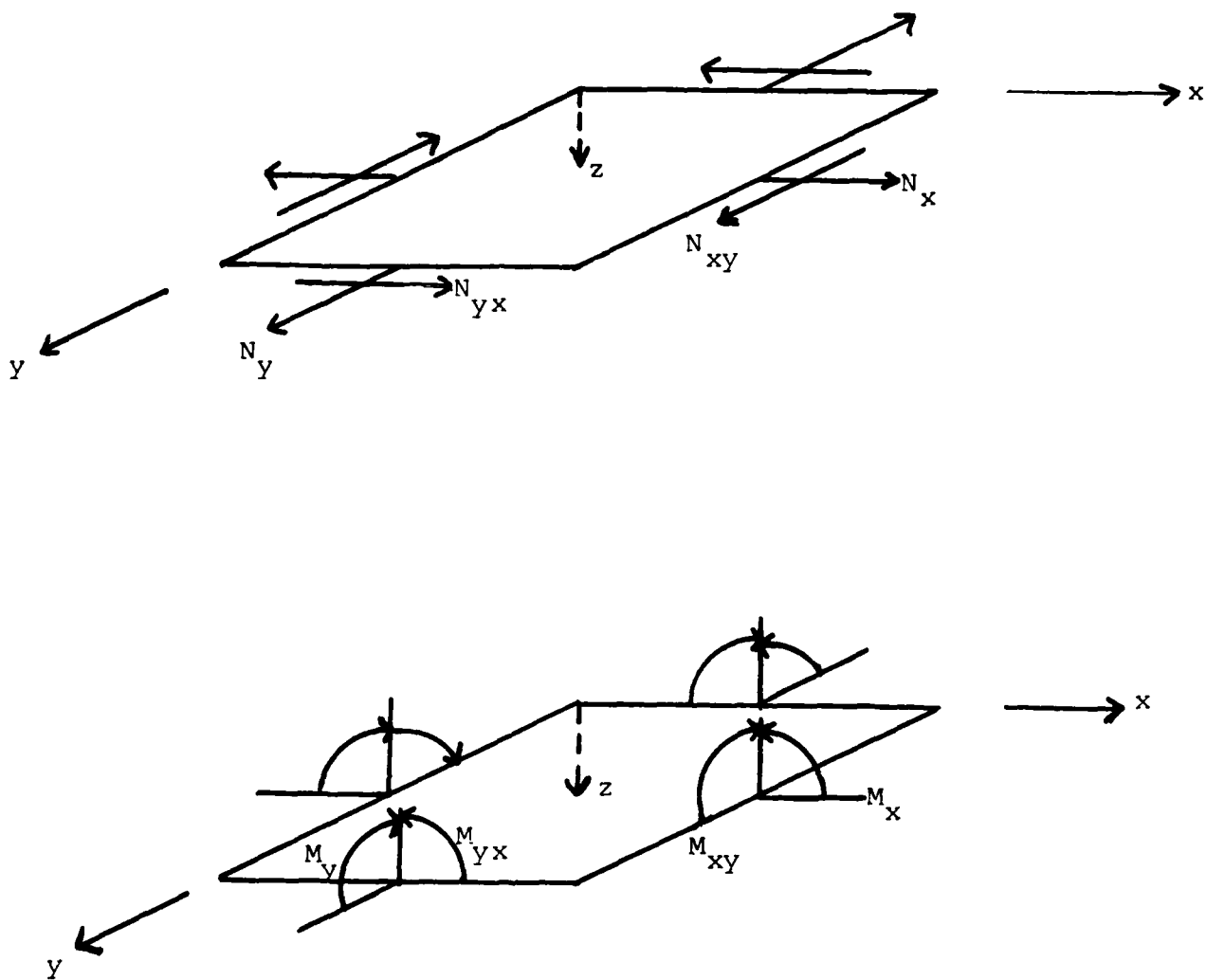


FIGURE 1: Positive Forces and Moments Acting on a Laminate

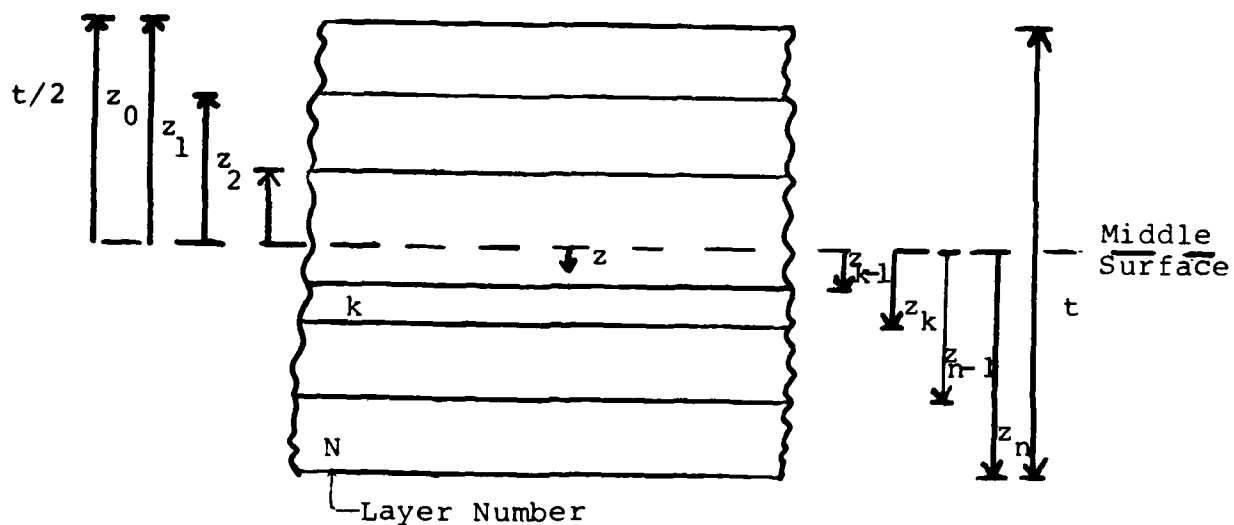


FIGURE 2: Geometry of an N Layered Laminate

The resultant forces and moments are defined as [17].

$$\begin{bmatrix} N_x \\ N_y \\ N_{xy} \end{bmatrix} = \int_{-t/2}^{t/2} \begin{bmatrix} \sigma_x \\ \sigma_y \\ \tau_{xy} \end{bmatrix}_k dz = \sum_{k=1}^N \int_{z_{k-1}}^{z_k} \begin{bmatrix} \sigma_x \\ \sigma_y \\ \tau_{xy} \end{bmatrix} dz \quad (28)$$

$$\begin{bmatrix} M_x \\ M_y \\ M_{xy} \end{bmatrix} = \int_{-t/2}^{t/2} \begin{bmatrix} \sigma_x \\ \sigma_y \\ \tau_{xy} \end{bmatrix}_k z dz = \sum_{k=1}^N \int_{z_{k-1}}^{z_k} \begin{bmatrix} \sigma_x \\ \sigma_y \\ \tau_{xy} \end{bmatrix} z dz \quad (29)$$

Where the N's are resultant force per unit length and the M's are the resultant moment per unit length. If one substitutes the stresses in, the resulting forces and moments become

$$\begin{bmatrix} N_x \\ N_y \\ N_{xy} \end{bmatrix} = \sum_{k=1}^N \begin{bmatrix} \bar{Q} \end{bmatrix}_k \left[\int_{z_{k-1}}^{z_k} \begin{bmatrix} \epsilon_x^0 \\ \epsilon_y^0 \\ \gamma_{xy}^0 \end{bmatrix} dz + \int_{z_{k-1}}^{z_k} \begin{bmatrix} \kappa_x \\ \kappa_y \\ \kappa_{xy} \end{bmatrix} z dz \right] \quad (30)$$

$$\begin{bmatrix} M_x \\ M_y \\ M_{xy} \end{bmatrix} = \sum_{k=1}^N \begin{bmatrix} \bar{Q} \end{bmatrix}_k \left[\int_{z_{k-1}}^{z_k} \begin{bmatrix} \epsilon_x^0 \\ \epsilon_y^0 \\ \gamma_{xy}^0 \end{bmatrix} z dz + \int_{z_{k-1}}^{z_k} \begin{bmatrix} \kappa_x \\ \kappa_y \\ \kappa_{xy} \end{bmatrix} z^2 dz \right] \quad (31)$$

However, recalling that the middle surface strains and curvatures are not a function of z , they can be removed from under the summation sign. The equations can then be integrated through the thickness of each composite layer to yield.

$$\begin{bmatrix} N_x \\ N_y \\ N_{xy} \end{bmatrix} = \begin{bmatrix} A_{11} & A_{12} & A_{16} \\ & A_{22} & A_{26} \\ \text{Sym} & & A_{66} \end{bmatrix} \begin{bmatrix} \epsilon_x^0 \\ \epsilon_y^0 \\ \gamma_{xy}^0 \end{bmatrix} + \begin{bmatrix} B_{11} & B_{12} & B_{16} \\ & B_{22} & B_{26} \\ \text{Sym} & & B_{66} \end{bmatrix} \begin{bmatrix} \kappa_x \\ \kappa_y \\ \kappa_{xy} \end{bmatrix} \quad (32)$$

$$\begin{bmatrix} M_x \\ M_y \\ M_{xy} \end{bmatrix} = \begin{bmatrix} B_{11} & B_{12} & B_{16} \\ & B_{22} & B_{26} \\ \text{Sym} & & B_{66} \end{bmatrix} \begin{bmatrix} \epsilon_x^0 \\ \epsilon_y^0 \\ \gamma_{xy}^0 \end{bmatrix} + \begin{bmatrix} D_{11} & D_{12} & D_{16} \\ & D_{22} & D_{26} \\ \text{Sym} & & D_{66} \end{bmatrix} \begin{bmatrix} \kappa_x \\ \kappa_y \\ \kappa_{xy} \end{bmatrix} \quad (33)$$

where $[A_{ij}]$ is the extensional stiffness matrix and

is defined as

$$A_{ij} = \sum_{k=1}^N (\bar{Q}_{ij})_k (z_k - z_{k-1}) \quad (34)$$

$[B_{ij}]$ is the coupling stiffness matrix and is

$$B_{ij} = \frac{1}{2} \sum_{k=1}^N (\bar{Q}_{ij})_k (z_k^2 - z_{k-1}^2) \quad (35)$$

Finally, $[D_{ij}]$ is the bending stiffness matrix which is

$$D_{ij} = \frac{1}{3} \sum_{k=1}^N (\bar{Q}_{ij})_k (z_k^3 - z_{k-1}^3) \quad (36)$$

It may be stated that by using the finite element technique to find the displacement vector of the middle surface of a panel using numerical differentiation to solve Sanders' equations the midsurface strains and curvatures can be calculated. If one incorporates the midsurface strains and curvatures, the strain at any point can be found by using the Kirchhoff-Love hypothesis. Since the material properties, ply layup and individual laminae thickness are known, the transformed reduced stiffness matrix can be generated which is then used with the corresponding strains to formulate the individual laminae stresses and the corresponding resultant laminate forces and moments. All the forces are now known in order to calculate the potential energy and check for static equilibrium. All that is needed is the displacement vector generated by finite element techniques. Through the strain relationship, remember that in solving this problem in the nonlinear case, the displacement vector being established is determined by a prior solution. Thus, a nonlinear solution algorithm is needed.

Nonlinear Solution Algorithm Theory

The solution technique used by STAGS in the nonlinear analysis branch is a modified Newton-Raphson interaction scheme with a periodic updating of the stiffness matrix [13]. The difference between the modified and full Newton-Raphson technique is in the modified technique, a previous stiffness matrix is factored and its inverse is used instead of reforming the stiffness matrix and inverting for every load increment (load step). The stiffness matrix is then inverted only when there is convergence difficulties, that is, the solution is slow to converge or the solution diverges [18]. In order to understand the solution technique, some equations will be developed.

The problem that will be dealt with is that of static equilibrium, and the solution as previously stated, is nonlinear. But since the basic problem is static equilibrium, the sum of the applied, residual, and restoring force vectors must equal zero at any load step, or the body is not in equilibrium.

$$\{F(X_{n+1})\} = \{FX_n\} = 0 \quad (37)$$

where $\{F(X_{n+1})\}$ is the vector sum of all forces corresponding to the $\{X_{n+1}\}$ displacement vector for the $n+1$ load step. If one uses Taylors series expansion $\{F(X_{n+1})\}$ can be

expressed as

$$0 = \{F(X_{n+1})\} = \{F(X_n)\} + \frac{\delta\{F(X_n)\}}{\delta\{X_n\}} (\{X_{n+1}\} - \{X_n\}) + \text{H.O.T.} \quad (38)$$

$$0 = \{F(X_n)\} + \frac{\delta\{F(X_n)\}}{\delta\{X_n\}} \{\Delta X\} + \text{H.O.T.} \quad (39)$$

therefore

$$\frac{-\delta\{F(X_n)\}}{\delta\{X_n\}} \{\Delta X\} = \{F(X_n)\} + \text{H.O.T.} \quad (40)$$

where H.O.T. represent higher order terms. However, noting that the derivative of the force vector is the negative of the nonlinear stiffness matrix $[K(X_n)]$ one may write.

$$[K(X_n)] \{\Delta X\} = \{F(X_n)\} + \text{H.O.T.} \quad (41)$$

Another way the force vector can be written is

$$\{F(X_n)\} = \{R\} + \text{H.O.T.} \quad (42)$$

where $\{R\}$ is the vector of externally applied forces and the H.O.T. are the forces generated by the strain energy and residual forces. If one substitutes Equation (42) into Equation (41) and combines the H.O.T. the result becomes

$$[K(X_n)] \{\Delta X\} = \{R\} + \text{H.O.T.} \quad (43)$$

or

$$[K(X_n)] \{\Delta X\} - \{R\} + \text{H.O.T.} = 0 = \{F(X_{n+1})\} \quad (44)$$

STAGS treats $[K(X_n)] \{\Delta X\}$ as a nonlinear operator L acting on the displacements

$$0 = \{F(X_{n+1})\} = L(X_n) - R + \text{H.O.T.} = \{F(X_n)\} \quad (45)$$

Thus, the operator L is the first derivative of the strain energy functional and the first derivative of L is the nonlinear stiffness matrix $[K(X_n)]$ [13]. The above equations can be incorporated into a modified Newton-Raphson iteration scheme, but first (referring to Figure 3) notice that for the one dimensional case.

$$\frac{\delta \phi}{\delta X} = \frac{\{\Delta \phi_n\}}{\{\Delta X_n\}} \quad (46)$$

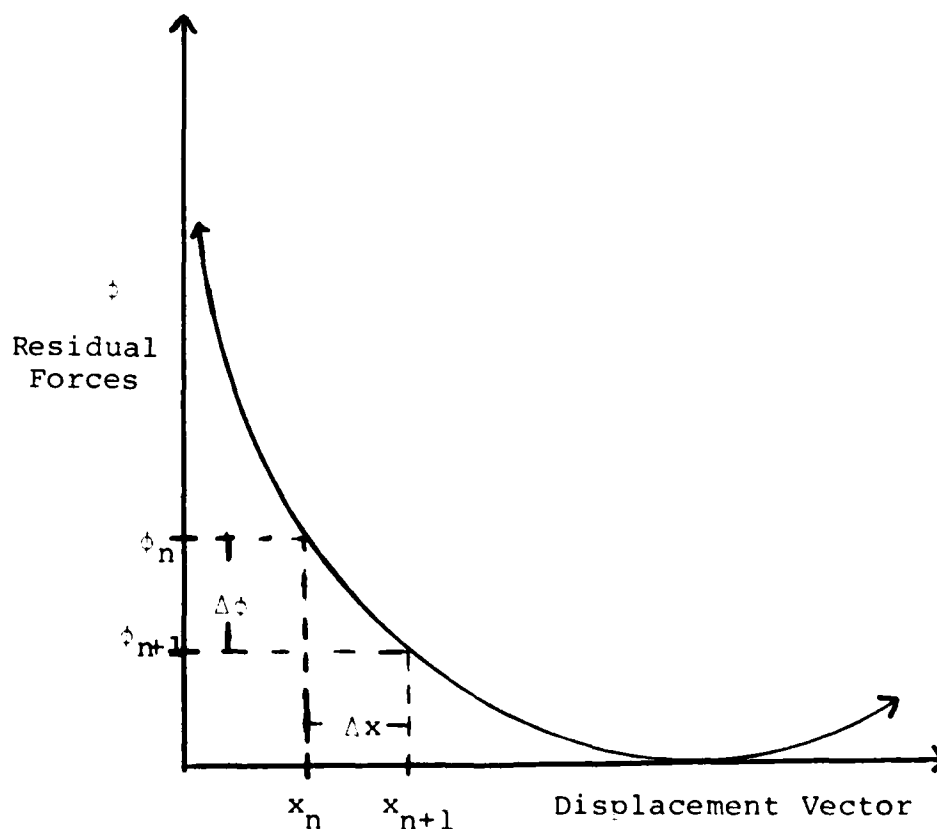


FIGURE 3: Residual Forces Versus Assumed Displacement

Where $\{\Delta\phi\}$ is the change of residual forces for an assumed change in the displacement vector considering a given applied external force vector $\{R\}$. $\{\Delta X\}$ vector can be found by

$$\{\Delta X\} = \{X_{n+1}\} - \{X_n\} = - \{\Delta\phi\} / \begin{bmatrix} \frac{\delta\phi_n}{\delta X_n} \end{bmatrix} \quad (47)$$

Recalling Equation (45)

$$\text{H.O.T.} = L(X_n) - \{R\} \quad (48)$$

and noting that the change in the residual forces $\{\Delta\phi\}$ are the higher order terms, it is possible to write

$$\{X_{n+1}\} - \{X_n\} = \frac{-(L(x_n) - \{R\})}{\frac{\delta\phi}{\delta X_n}} \quad (49)$$

But, the $[\delta\phi/\delta X]$ is the nonlinear stiffness matrix at that given load step $[K(X_n)] = L'(X_n)$. Therefore, the modified Newton-Raphson solution scheme can be written using a previously factored matrix

$$\{X_{n+1}\} = \{X_n\} + L'(X_m)^{-1} (\{R\} - L(X_n)) \quad (50)$$

where $L'(X_m)^{-1}$ is the previously factored stiffness matrix. The nonlinear operator L can be removed and the solution scheme in terms of the nonlinear stiffness matrix $[K(X_n)]$, becomes

$$\{X_{n+1}\} = \{X_n\} + [K(X_m)]^{-1} (\{R\} - [K(X_n)]\{\Delta X\}) \quad (51)$$

The complete flow chart for the nonlinear solution algorithm is shown in Figure 4. Therefore, by using finite element techniques and formulating the nonlinear stiffness matrix directly, along with using a modified Newton-Raphson iteration scheme, the displacement vector can be found for a given load vector knowing the previous displacement and load vectors. As noted earlier, once the displacement vector is known, all the strains, stresses and resultant forces can then be calculated.

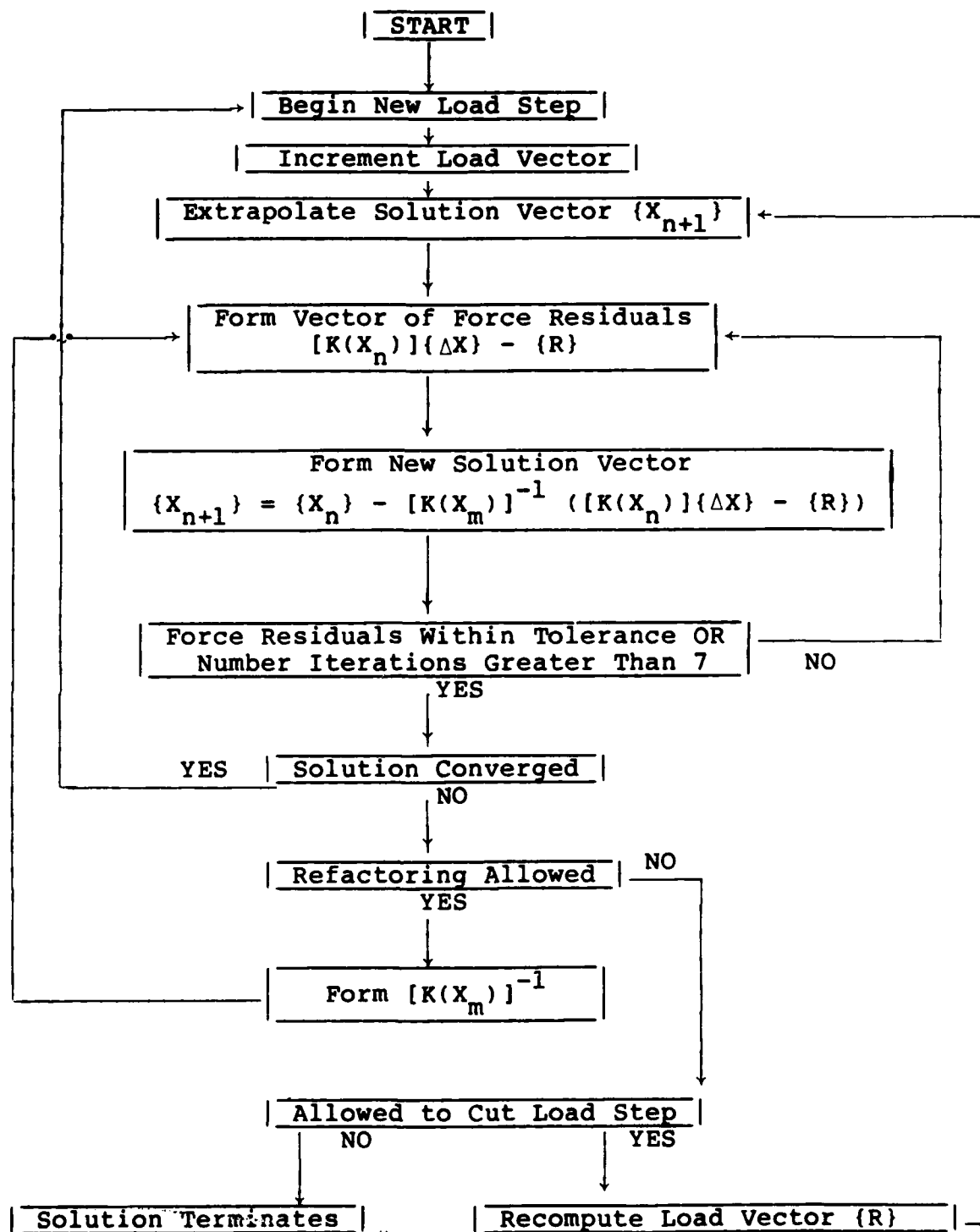


FIGURE 4: Nonlinear Solution Algorithm

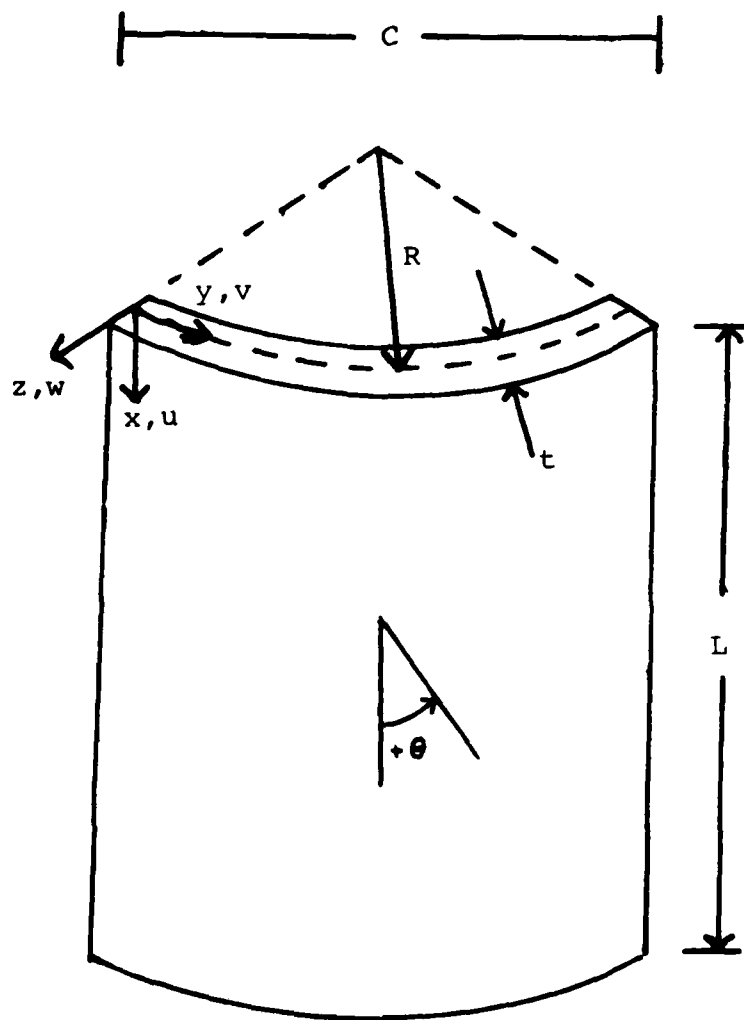
MODELLING

Panel Properties

This thesis will model a graphite epoxy composite panel that is 12 inches long, a chord length of 12 inches, and a radius of curvature of 12 inches. The panels dimensions and sign convention are shown in Figure 5. The panel has eight .005 inch plies for a total panel thickness of .04 inches. Four different ply orientations will be used, $[0, +45, -45, 90]_s$, $[0, -45, +45, 90]_s$, $[90, 45, -45, 0]_s$, and $[90, 0]_{2s}$. Also, two sets of boundary conditions will be used. In both sets of boundary conditions the top of the panel will be clamped with only the u degree of freedom (DOF) free and the bottom of the panel will be clamped with no DOF's. The vertical sides of the panel will be simply supported with u, v, and rotation about u free in one set of boundary conditions and only u, and the rotation about u free in the second set of boundary conditions. The panel will be loaded along the top edge. The material properties of each ply are:

$$E_1 = 20.5 \times 10^3 \text{ KSI} \quad E_2 = 1.3 \times 10^3 \text{ KSI} \quad G_{12} = .75 \times 10^3 \text{ KSI}$$
$$\nu_{12} = .335$$

These are the same material properties used by M. L. Becker in his paper [3] and N. R. Bauld, Jr. in his report [10].



t = thickness = 8 plies @ 0.005" = 0.04"

R = radius = 12"

C = width = chord length = 12"

L = length = 12"

x, y, z = structural coordinate directions

θ = ply orientation

u, v, w = displacements

FIGURE 5: Panel Notation

Element Selection

The current version of STAGS has 20 different elements incorporated into it. There are 6 transition elements, 6 triangular elements, and 8 quadrilateral elements. The triangular and quadrilateral elements are divided into two types, a membrane type and a plate type element. Since all the membrane type elements have no out of plane DOF, they are not a good choice for this study. In the plate type elements, STAGS breaks the quadrilateral element down further into type 1 and type 2. The triangular plate elements and the type 2 quadrilateral plate elements do not have normal rotations as a DOF, therefore, they are not suitable for shell elements. The type 1 plate element, called the QUAF elements are composed of the 410 element and the 411 element, both of which have the basic 6 DOF at each of the corner nodes (See Figure 6). In addition to these basic 6 DOF, the QUAF 411 element has an additional 8 DOF. There are 4 midside nodes that have a tangential displacement DOF and at each of the corner nodes there is an additional rotational DOF. This DOF is the rotation of the plane that is defined at the intersection of the corresponding sides of that node. The rotation was added specifically to the element to help alleviate the problem of trying to model a curved surface with flat elements [16]. The shape functions used for the 411 element for inplane displacements

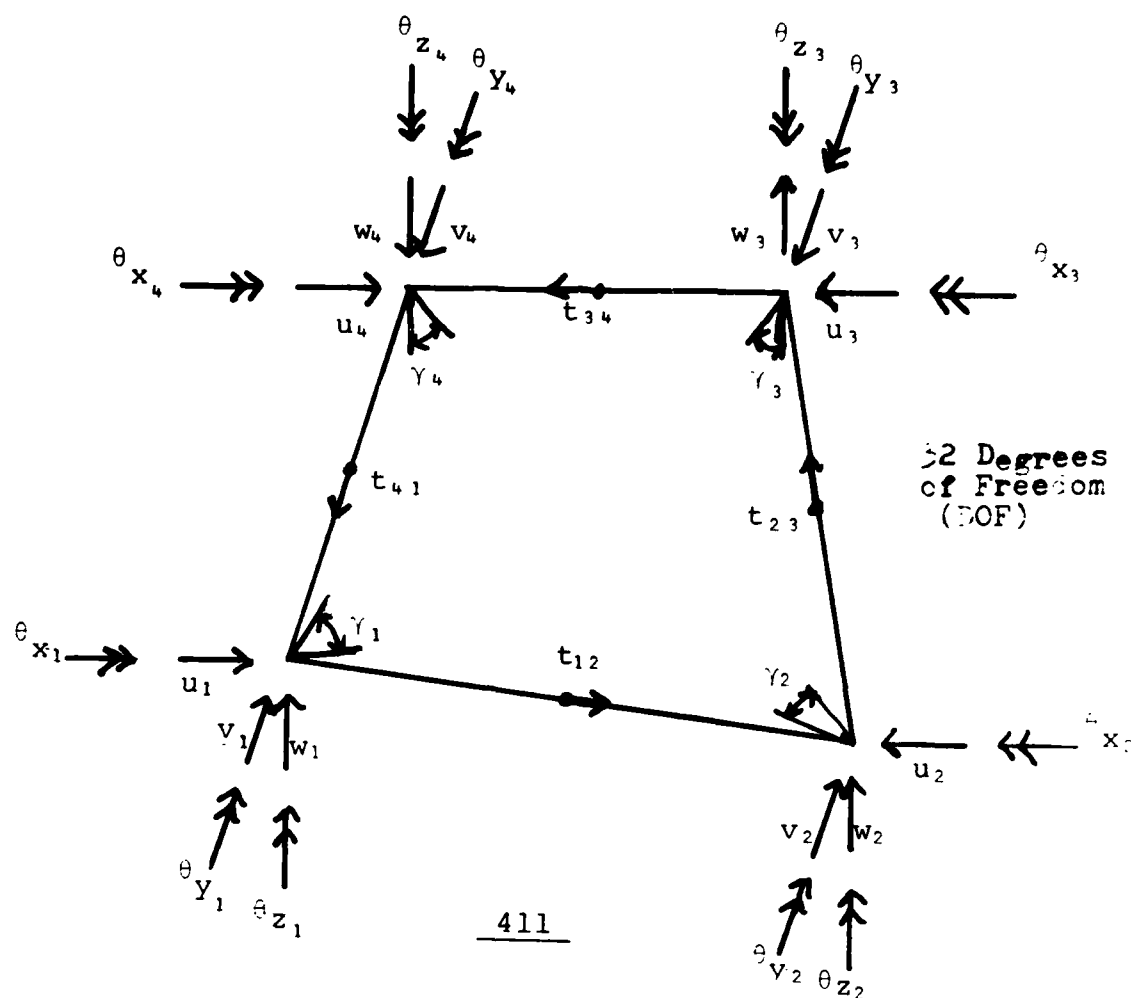


FIGURE 6: Element DOF

are cubic parallel to the edge and quadratic perpendicular to the edge and the bending shape functions are cubic in both directions [15]. Since a nonlinear collapse analysis will require large deflections and moderately large rotations, the QUAF 411 element will be the best element to use because of the extra rotational DOF at the corner node and translational DOF at the midside. However, there is one disadvantage to the 411 element. There is no suitable transition element in the library, therefore, a constant grid size is required.

Grid Selection

The first panel to be modeled has a 2 inch by 2 inch square hole located in the center of the panel. There are two grid sizes with constant spacing that will be used to model this panel. The first grid size will have 13 rows and columns with 1 square inch elements. The second grid size to be used will have 25 rows and columns with one half inch square elements (.25 square inch element). The critical load for non-linear collapse was completed for both grid sizes. The 13 by 13 grid size had a collapse load that is 12.5% higher than the finer grid (See Figure 7). The largest difference was in the computer time (CPU time) needed for completion and the number of different load steps used in solving the problem. The coarser grid completed 76 load steps to reach its collapse load in only 20% of the CPU time of the finer grid. The finer grid was stopped just prior to completion because the last load step used 1500 CPU seconds to complete. The load versus top edge displacement was plotted to see the differences in the stiffness between the two grid sizes (See Figure 8). Since both the grid signs were very close in stiffness to each other with only a 12.5% difference in the collapse load, the coarser grid size, one square inch elements, will be used thus saving on CPU time and expense for the panels with cutouts.

GRID SELECTION
DATA SHEET

2 INCH by 2 INCH CUTOUT

	13X13 Grid	25X25 Grid
NDOF	2100/1253	7840/5029
BANDWIDTH	98	192
CPU TIME	971	4852
COLLAPSE LOAD	215	191
NO. OF LOAD STEPS	76	22

IMPERFECTION GRID

.04 INCH IMPERFECTION
5HS by 5HS

	15X15 Grid	25X25 Grid
NDOF	2835/1668	7975/5018
BANDWIDTH	117	198
CPU TIME	3466	5946
COLLAPSE LOAD	273.9	243.5
NO. OF LOAD STEPS	75	23

NOTE: The 15X15 grid was 4% higher on the bifurcation load when compared to the finite difference load M. L. Beckers Paper [3].

FIGURE 7: Grid Selection Data

2 INCH by 2 INCH CUTOUT

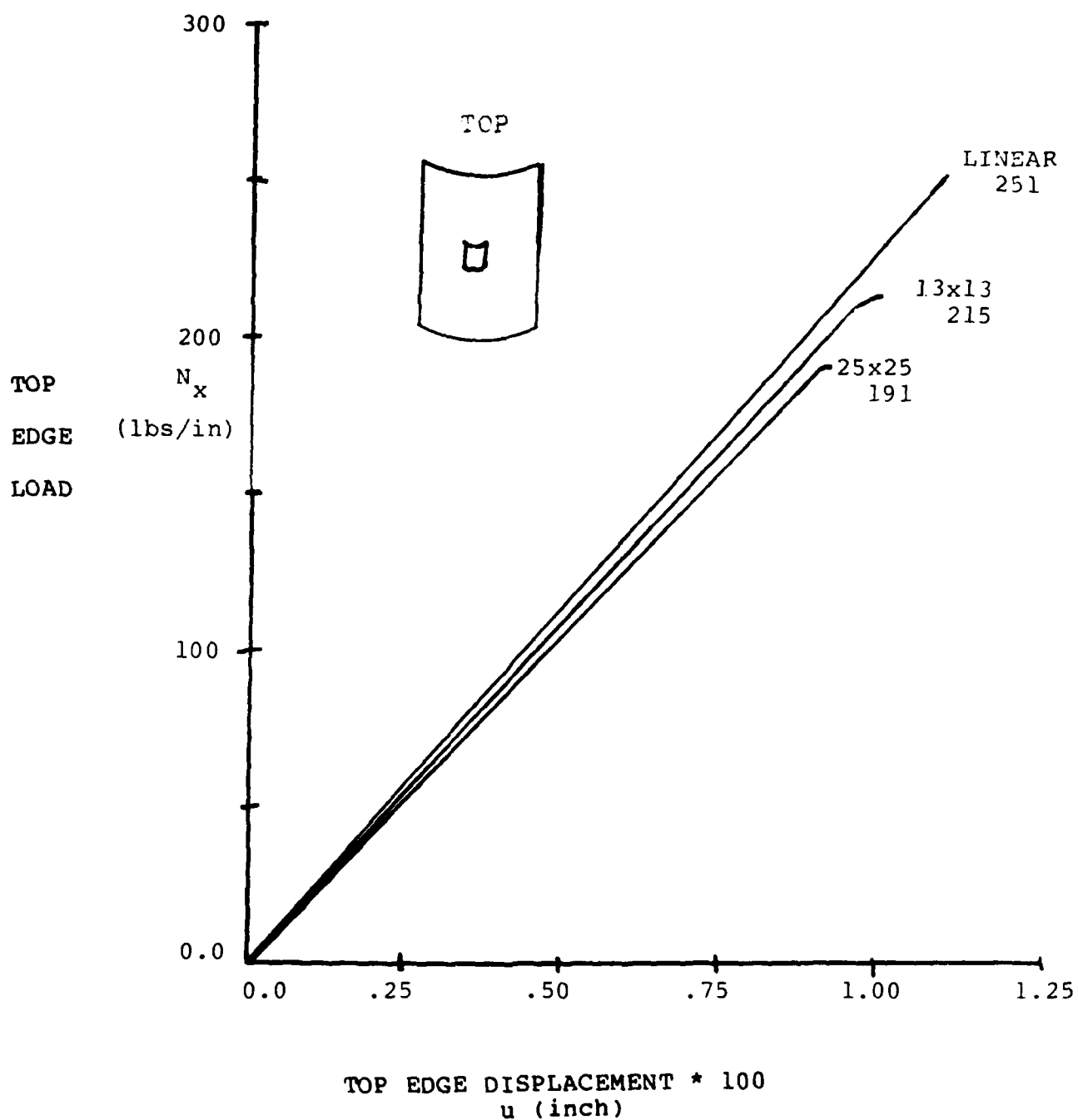


FIGURE 8: Convergence Study for Cutout Panel

For the panels with surface imperfections 2 different grid sizes will be compared along with a linear analysis of an imperfection free panel. A nonlinear collapse analysis was run on a panel that had a .04 inch maximum amplitude imperfection at the center of the panel with 5 half sine waves going in each direction. The 2 grid sizes used on this panel with the imperfection was 15 by 15 grid and a 25 by 25 grid. The coarser grid was 14.6% higher in collapse load than the finer grid (See Figure 7). This time the CPU time difference was not great. The coarse grid was run in 42.7% less time than the finer mesh. An imperfection free panel was run to find the linear bifurcation load using the 411 element and 15 by 15 mesh. The panel selected had the same size, shape, and material properties as used by M. L. Becker in his paper [3]. His article used a finite difference method to calculate the bifurcation load using a one half square inch mesh. The 15 by 15 grid with the 411 element computed a bifurcation load that was 4% higher than the load that was calculated by Becker. Therefore, a 15 by 15 grid is to be used in the imperfection study which means the elements will be .857 inches square. In addition, the convergence study was run with the minimum imperfection wavelength of 2.4 inches. Therefore, a minimum of 2.8 elements per half sine wave will have to be used to insure accuracy of the grid size and because a fewer number of elements per half sine wave have not been checked for convergence.

DISCUSSION AND RESULTS

411 Element

The first result of this study was the discovery of the 411 element. In order to make this project successful, with a reasonable amount of computer cost involved considering the nonlinear iterations, a good element was needed. A compatability problem at the junction of elements will arise when modelling a curved panel with flat elements since adjacent elements do not lie in the same plane. The 411 element in STAGS has been developed specifically so that the displacement compatability can be incorporated for flat elements meeting at a nonzero angle [14]. This is accomplished by adding the extra DOF γ at each corner (Figure 6). This angle (γ) insures that each element's common corner node has the same planar rotation as its common neighboring element. This will permit the original curved surface a relatively smooth transition without any discontinuities forming at the edge of the elements. In addition, this extra DOF allows the curved surface to be modeled by larger elements producing comparable accuracy to the same surface modeled by smaller elements without the extra DOF. Therefore, the γ DOF reduces the total computer time for accurate results since the total number of DOF in a given problem can be made less.

Analytical Model Versus Experimental Study

The first study undertaken was to evaluate the finite element model for a panel which was experimentally tested incorporating accurately measured surface imperfections. Nelson R. Bauld, Jr. [10] completed such a study for the Air Force Flight Dynamics Laboratory and the designated BCP 9824-A-31 AS panel was arbitrarily selected. In his study, Bauld made 56 surface measurement on a 16 inch by 16 inch graphite-epoxy panel with a 12 inch radius of curvature. The measurements were made in a grid covering the surface with 10 columns across the panel and 9 rows down, with a measurement made at each interior grid point. By looking at each row and column of the grid, the number of half sine waves could be computed for that row or column. The average number of half sine waves was determined for the row and column directions and the surface imperfection. For analysis purposes, the surface imperfection will be modelled by to the average number of half sine waves circumferentially (3) and longitudinally (2). The average magnitude of the 56 measured surface imperfections was .00634 inches. The center of the panel was chosen as the initial point of maximum amplitude and the imperfection pattern (3 half sine waves circumferentially and 2 half sine waves longitudinally) was generated from this point with a maximum imperfection amplitude of .00634 inches directed radially outwards. The experimental panel, when tested, collapsed at a

total load (N_x) of 290.1 lbs/in with a total displacement of the top edge of .021 inches. Using STAGS and the imperfection model referred to previously, the nonlinear collapse load (N_x) was 365.1 lbs/in with a total top edge displacement of .019 inches. Figure 9 shows both the experimental and analytical panels load versus top edge displacement curves. The STAGS solution predicted a 25.8% higher collapse load and was 9.5% lower on the top edge displacement. This demonstrated that the model, using STAGS, was stiffer than the actual tested panel and was expected. Overall though the author believes the model showed very good agreement in both the collapse load and the total top edge displacement. With this agreement, the model was said to be acceptable for use in further studies.

In evaluating the results of this nonlinear analysis, two items appear to show the greatest amount of nonlinearity. This was the radial displacement and the moment resultant about the y axis (M_x). The radial displacements were found to follow the shape of the initial imperfection. At the lower load level of 221 lbs/in (60% of the collapse load) radial outward displacements showed twice the radial inward displacements (Figure 10). These radial displacements are the displacement of the midsurface with respect to the initial imperfection. As the load is increased to 331 lbs/in (91% of the collapse load) the radial inward displacements increased at a greater rate than the outward displacements so that they equal

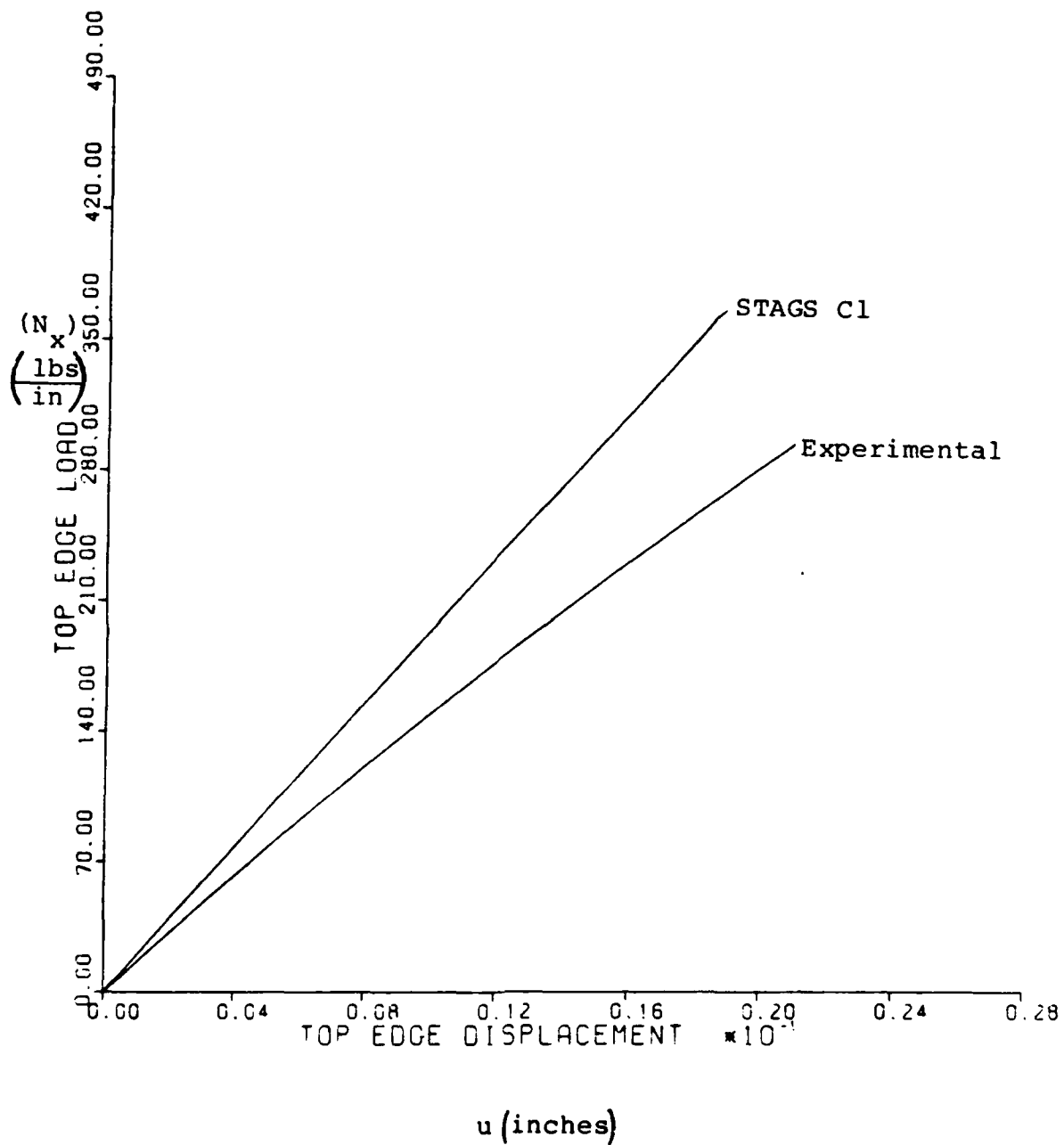


FIGURE 9: Load Versus Top Edge Displacement
On BCP 9824-A-31-AS Panel

Experimental Panel

$$N_x = 221 \text{ lbs/in}$$

Positive Contour Levels Are Radial Outward

Maximum Displacement = .0056 inch

Displacement Contours Are In 10^{ths} of Maximum Displacement

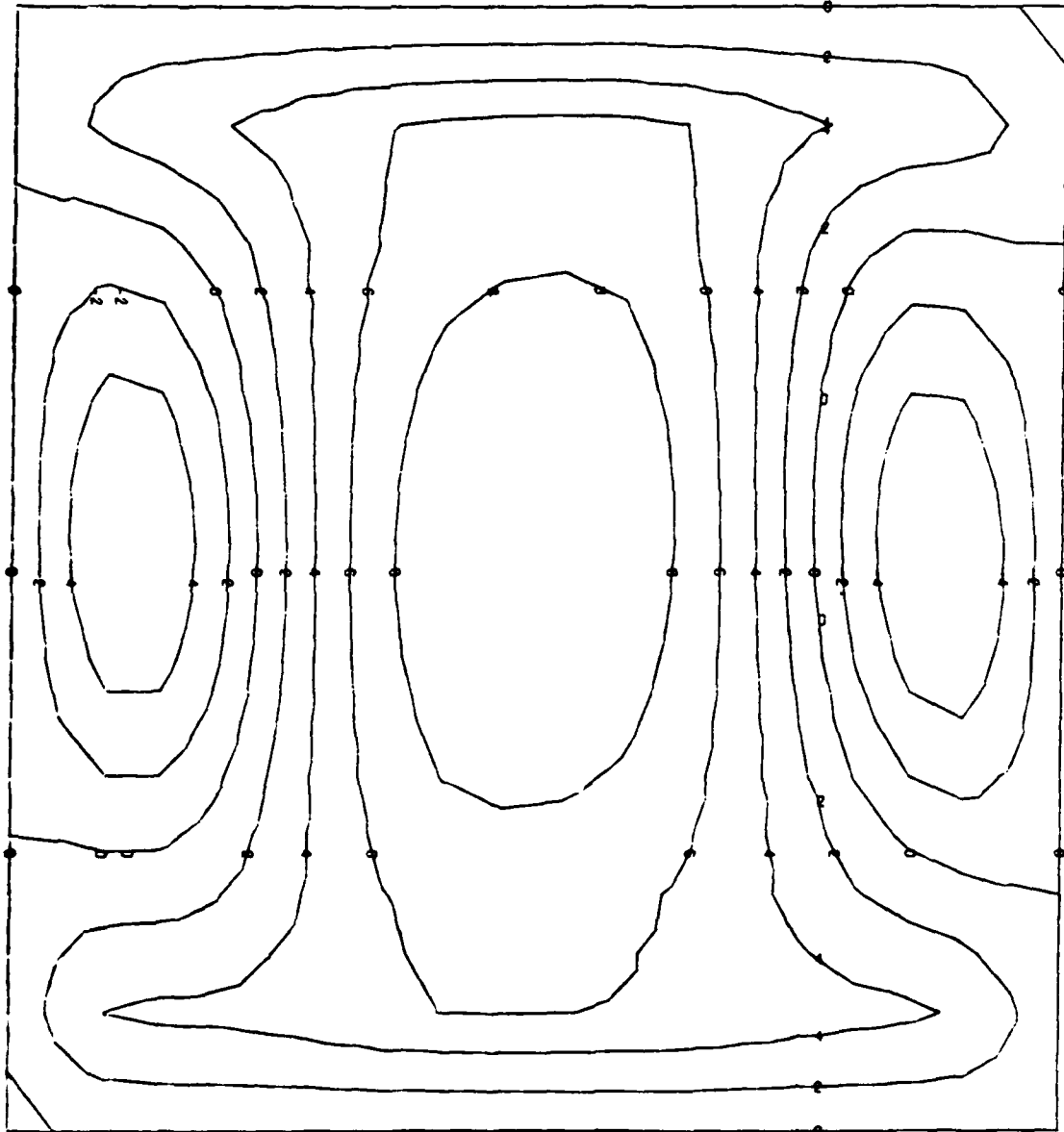


FIGURE 10: W Component Displacement Contours

each other (Figure 11). Just prior to collapse, at 363.5 lbs/in loading (99.5% of the collapse load), the panel loses the symmetry in radial displacements that it showed in earlier load steps (Figure 12). The radial inward displacements grew at a greater rate became larger than the radial outward displacements. This increase in the radial displacement is caused by the changes in the moment resultants about the y axis, M_x . As can be observed in Figure 13, as the early load levels are increased, the M_x resultant across the center of the panel is symmetric and increases symmetrically. At an 81 lbs/in load level, the M_x resultant has almost the same magnitude in the positive direction at the center of the panel as it has in the negative direction at the $\frac{1}{4}$ and $\frac{3}{4}$ chord lengths. The positive M_x corresponds to the radial outward displacements and negative M_x likewise corresponds to the inward radial displacements. As the load level is increased to 281 lbs/in, the positive M_x only doubles its magnitude while the negative M_x increases to 600% of its original value. This building of the negative M_x faster than the positive accounts for the larger magnitude of change in the negative radial displacements over the positive. As the load level is increased up to the collapse load, the M_x resultant loses its symmetry and the overall shape of the moment curve changes. The moment function near the center of the panel, where M_x was increasing positively, now decreases in magnitude and has a very slight negative value at collapse.

Experimental Panel

$N_x = 331 \text{ lbs/in}$

Positive Contour Levels Are Radial Outward

Maximum Displacement = .0056 inch

Displacement Contours Are In 10^{ths} of Maximum Displacement

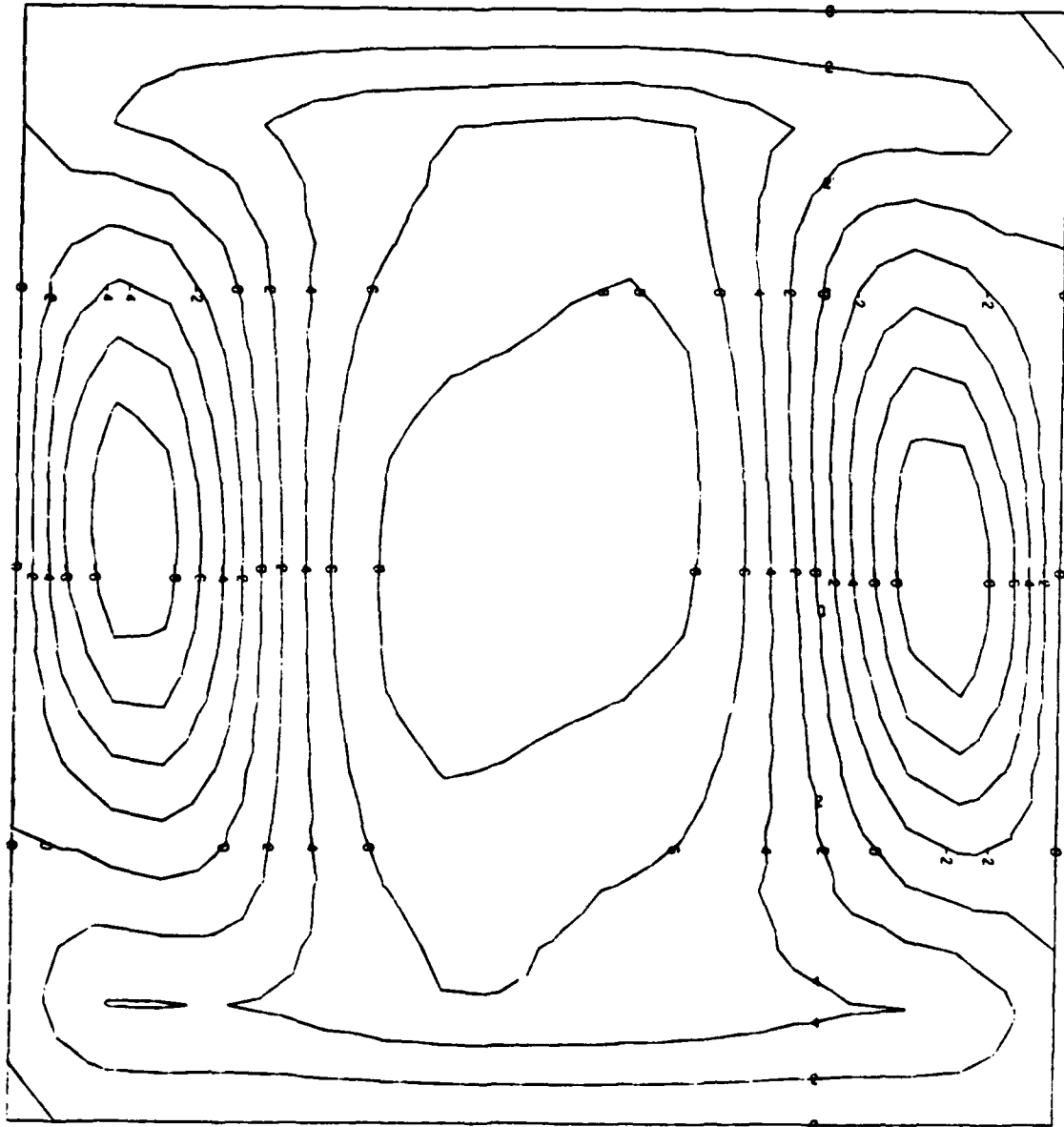


FIGURE 11: W Component Displacement Contours

Experimental Panel

$N_x = 363.5 \text{ lbs/in}$

Positive Contour Levels Are Radial Outward

Maximum Displacement = .0056 inch

Displacement Contours Are In 10^{ths} of Maximum Displacement

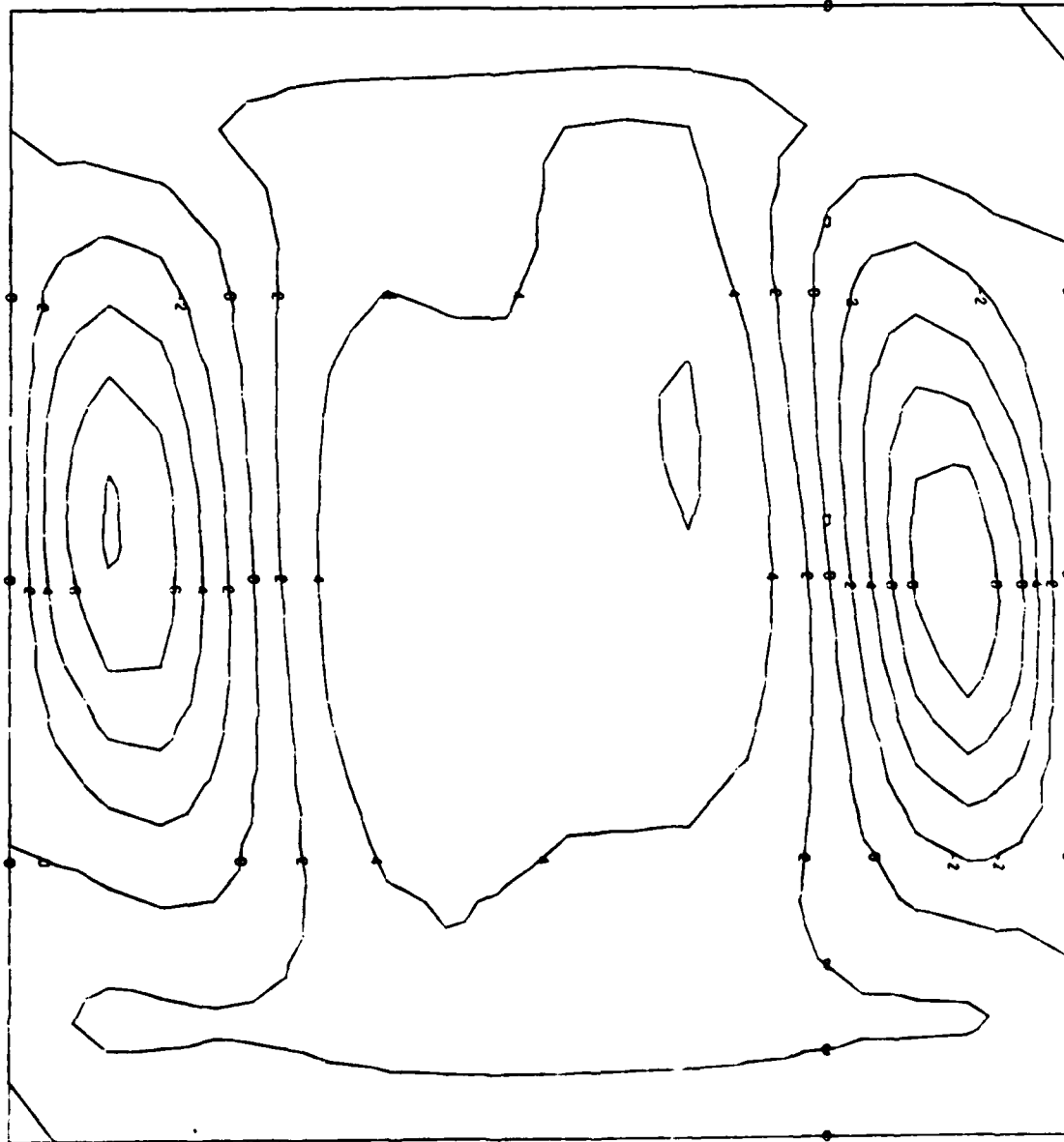


FIGURE 12: W Component Displacement Contours

Plotted Load Levels Are:

81 lbs/in
181 lbs/in
281 lbs/in
365.1 lbs/in

Load Levels Increase Away From Horizontal Axis
Radial Displacement 8 Inches From Top of Panel

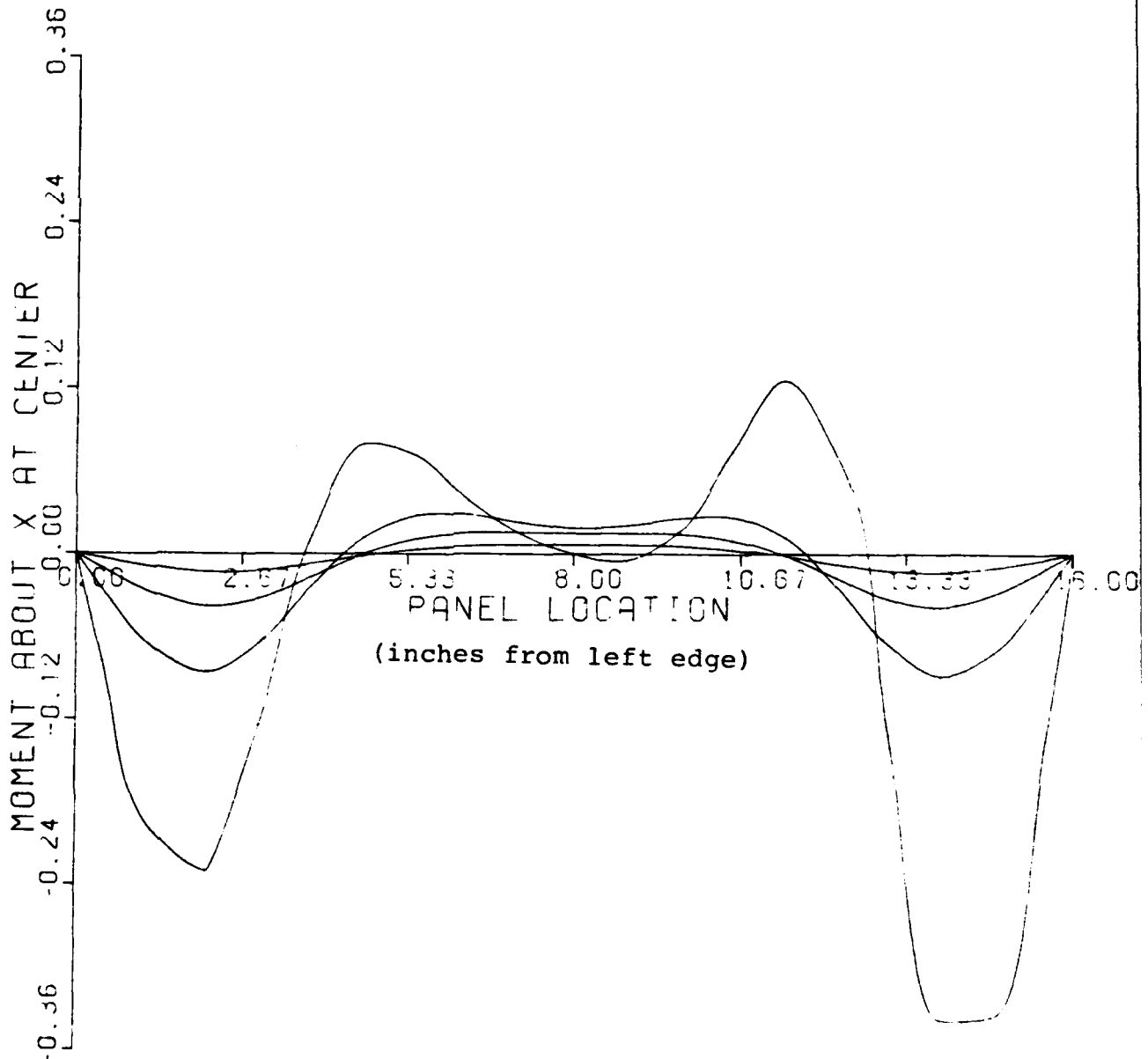


FIGURE 13: M_x at Different Load Levels

This unsymmetric shape of the M_x profile corresponds with the unsymmetric radial displacements. All of this can be tied together because of the effect the initial surface imperfection has on the various curvatures of the panel. M_x is a function of κ_x and κ_y . When the surface imperfection is added, the values of κ_x and κ_y are no longer constant as they were in the perfect panel. Since the initial surface imperfection is small and symmetric, the initial changes in curvature will be small and symmetric. Now as the load level is increased, the M_x resultant will build according to the initial imperfection shape, and this will cause the radial displacements. These radial displacements will likewise cause a change in curvature. A radially inward directed displacement has a greater effect on the change of curvature than would an equal radial outward displacement. This change in the curvatures cause the negative M_x to grow faster than the positive M_x at the higher load levels because the radial displacements now have a larger affect than the initial surface imperfection. Therefore, the initial surface imperfections will influence the function M_x as it builds according to the shape of the imperfection. This is the reason why the displacement pattern in the panel follows the initial shape of the imperfection. As the M_x nonlinearly builds, this causes the radial displacements to build which further causes a change in curvature. This change in curvature has a greater effect when the displacement is radially inwards than

outwards. Therefore, the M_x grows at an increasing rate when the displacement is radically inwards along with the radial displacement itself. This phenomena continues until the panel reaches the collapse load and is no longer able to absorb any more potential energy. Any additional load increases the potential energy in the panel and the panel is not capable of absorbing it and stay in the symmetric shape. Therefore, the panel then redistributes the potential energy and through the larger rotations the panel loses its symmetric shape.

In conclusion to the experimental versus the analytical analysis, it can be seen that the model being used does a good job in predicting the collapse load and top edge displacements of a panel with surface imperfections. As the load level is increased the radial displacements of the panel will follow the initial shape of the surface imperfection. These radial displacements show a great deal of nonlinearity as the load level is increased and corresponds to the nonlinearity of the M_x resultant and the change in curvatures. This case study also demonstrates that the model and STAGS are acceptable to continue further studies of different imperfections analytically with good accuracy.

Analytical Imperfection Study

After verifying that the surface imperfection model correlated well with an experimentally tested panel, interest turned to the effects that the number of surface imperfections with same maximum amplitude, have on a cylindrical composite panel from the point of view of the collapse load and displacement patterns. The panel size and notation are the same as shown in Figure 5. The 411 element has been used with a 15 by 15 grid (196 total elements per panel). Two ply layups have been analyzed, the $[0, +45, -45, 90]_s$ and $[90, 0]_{2s}$. The maximum amplitude of the imperfection was chosen to be equal to the thickness of the panel (.04 inch). The point of origin for the generation of the surface imperfection will be the center of the panel with the maximum amplitude being radially outward (a positive w displacement). Five different imperfection patterns were chosen for each panel to be considered and are shown in Table 1.

Table 1

Imperfection Patterns

Number of Circumferential ½ Sine Waves	Number of Longitudinal ½ Sine Waves	Ply Layup $[0, 90]_{2s}$ or $[0, +45, -45, 90]_s$ or Both
2	2	Both
3	3	Both
5	5	Both
2	3	Both
4	4	$[90, 0]_{2s}$
5	2	$[0, +45, -45, 90]_s$

The boundary conditions on all the panels are: top edge clamped with only u free, bottom edge clamped, both sides are simply supported with u , v , and the rotation about u free. A nonlinear collapse analysis was accomplished for each panel using STAGS Cl. The different results follow.

Figures 14 and 15 are graphs of the relative top edge displacement versus relative loads for the two sets of panels. The load and displacement values were normalized relative to the linear bifurcation load and top edge displacement of an imperfection free panel with the same ply layup. The numbers on the curves refer to the imperfection pattern. For example, curve 52 corresponds to the imperfection pattern of 5 half sine waves circumferentially with 2 half sine waves longitudinally. In comparing the two figures, it can be seen that the $[90, 0]_{2s}$ panel showed a greater amount of nonlinearity in the top edge displacement than the $[0, +45, -45, 90]_s$ panels. The total number of surface imperfections each panel had is the product of the number of circumferential half sine waves and longitudinal half sine waves. As the number of imperfections increased in both panels, the collapse load decreased until there was a total of 9 surface imperfections. After this, increasing the number of imperfections did not necessarily increase the stiffness in the panel, but the load bearing capability of the panel increased. One of the largest differences noticed between the panels is that the $[0, +45, -45, 90]_s$ panel is more imperfection sensitive than the

Number	Sine Waves	
	Circumference	Longitudinal
22	2	2
23	2	3
33	3	3
52	5	2
55	5	5

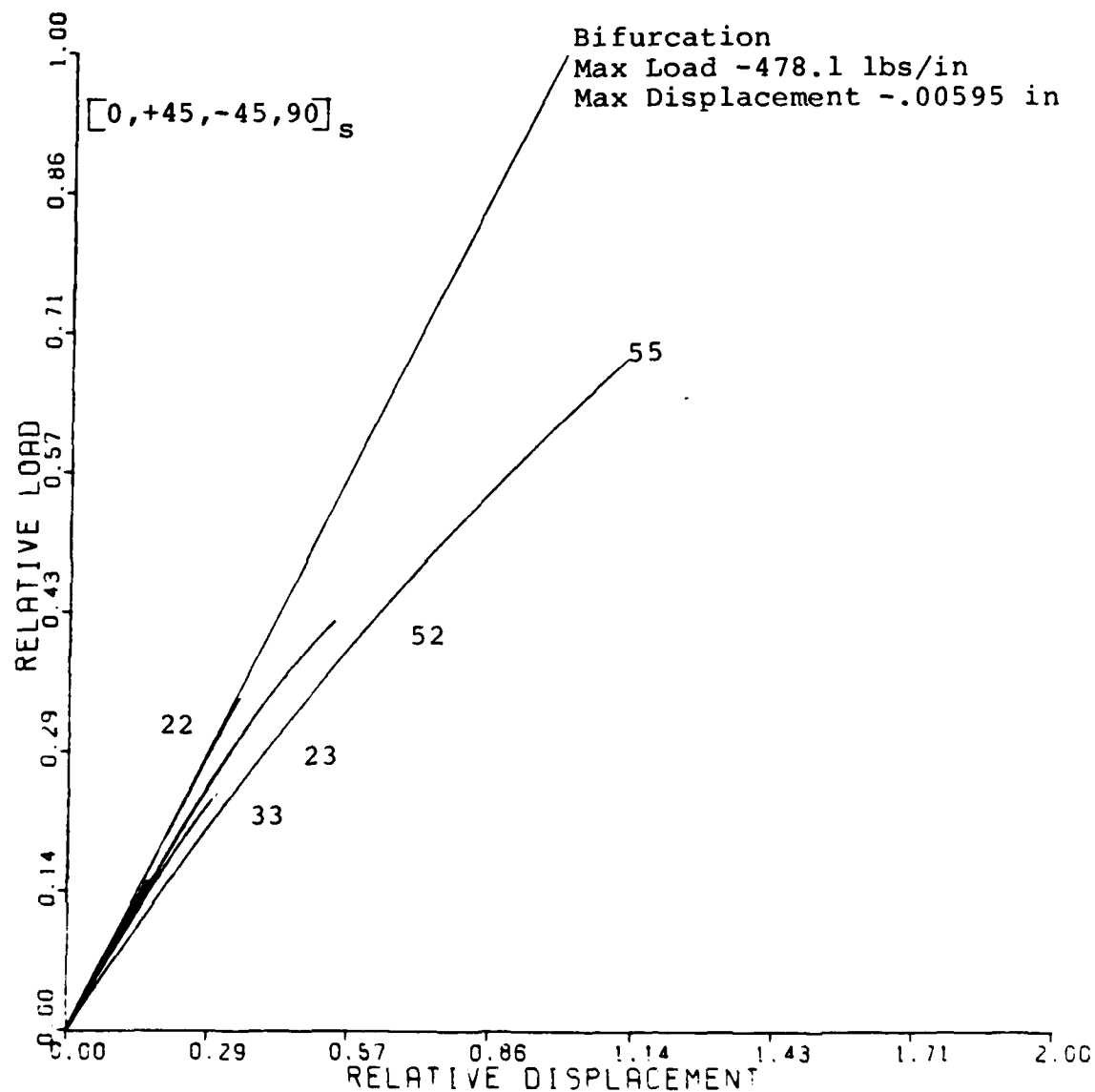


FIGURE 14: Relative Load Versus Relative Displacement

Note: The 23 curve overlays the 52 curve and terminates at .338 relative displacement

Number	Sine Waves	
	Circumference	Longitudinal
22	2	2
23	2	3
33	3	3
44	4	4
55	5	5

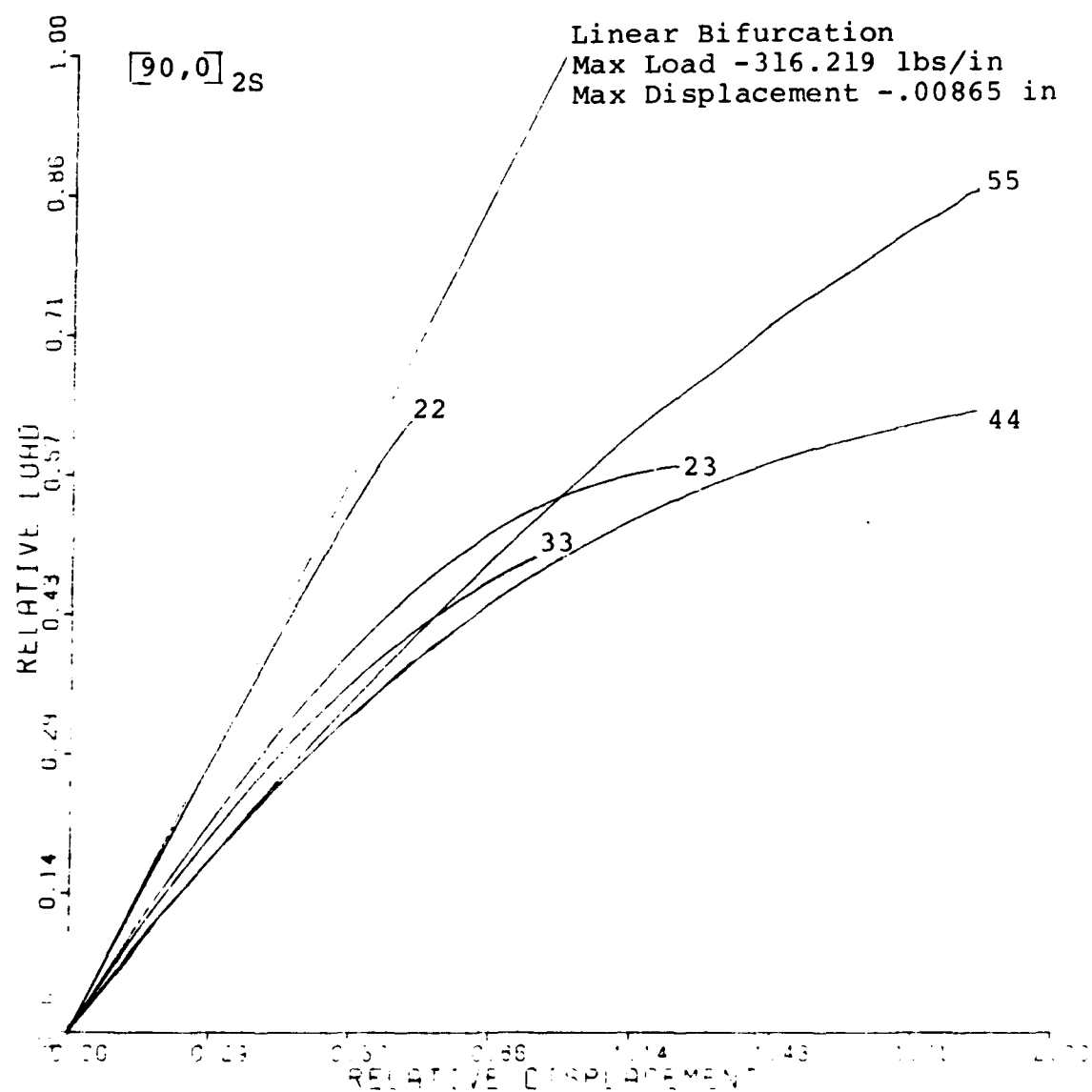


FIGURE 15: Relative Load Versus Relative Displacement

$[90, 0]_{2s}$. For example the 22 imperfection in the $[0, +45, -45, 90]_s$ panel can only handle 34% of the bifurcation load ($P_{cr} = 478$ lbs/in), however with the same imperfection the $[90, 0]_{2s}$ panel can withstand 63% of its bifurcation load ($P_{cr} = 316$ lbs/in). While the bifurcation loads of the two panels will show that the $[0, +45, -45, 90]_s$ panel can withstand the greater load, 478 lbs/in to 316 lbs/in for the $[90, 0]_{2s}$ panel, the $[90, 0]_{2s}$ panel will withstand a larger load with the same imperfection, 198 lbs/in versus 164 lbs/in for the 22 imperfection.

In both sets of panels the deformation pattern, as the load level increased, followed that of the initial surface imperfection. Figures 16-18 show the $[90, 0]_{2s}$ panel with 3X3 imperfection pattern at three different load steps and Figures 19-21 show a 5X5 imperfection pattern at 3 different load steps on a $[0, +45, -45, 90]_s$ panel. In viewing the six figures it is easy to see the initial shape of the imperfection. As the load is increased the initial magnitude of the imperfection increases with the greatest amount of increase in the radial inward direction. The effect is even more dynamic than it seems since the contour plots are plots of the w displacement relative to the initial imperfected surface. Therefore, the total displacement of the midsurface from the "perfect" panel, is the amount of displacement shown plus any initial imperfection of the panel at that point. To get the total displacement of the peaks and valleys in the

figures add .04 inch, which is the initial displacement of the imperfection at the start, to the magnitude shown in the figures. As was seen in the experimental study, the radial inwards displacements are about twice the magnitude of the outward displacements. As the load level is increased, the inward displacements increase at twice the rate as the outward displacements, thereby keeping a relative magnitude of two between them. These six plots are just examples of all the panels studied. The same displacement patterns were observed in all ten analytically observed panels, that is, the displacement pattern follows that of the initial surface imperfection and the radial inward displacement is twice the outward displacement.

$[90, 0]_{2s}$

$N_x = 86 \text{ lbs/in}$

Positive Contour Levels Are Radial Outward

Maximum Displacement = .023 inch

Displacement Contours In 10^{ths} of Maximum Displacement

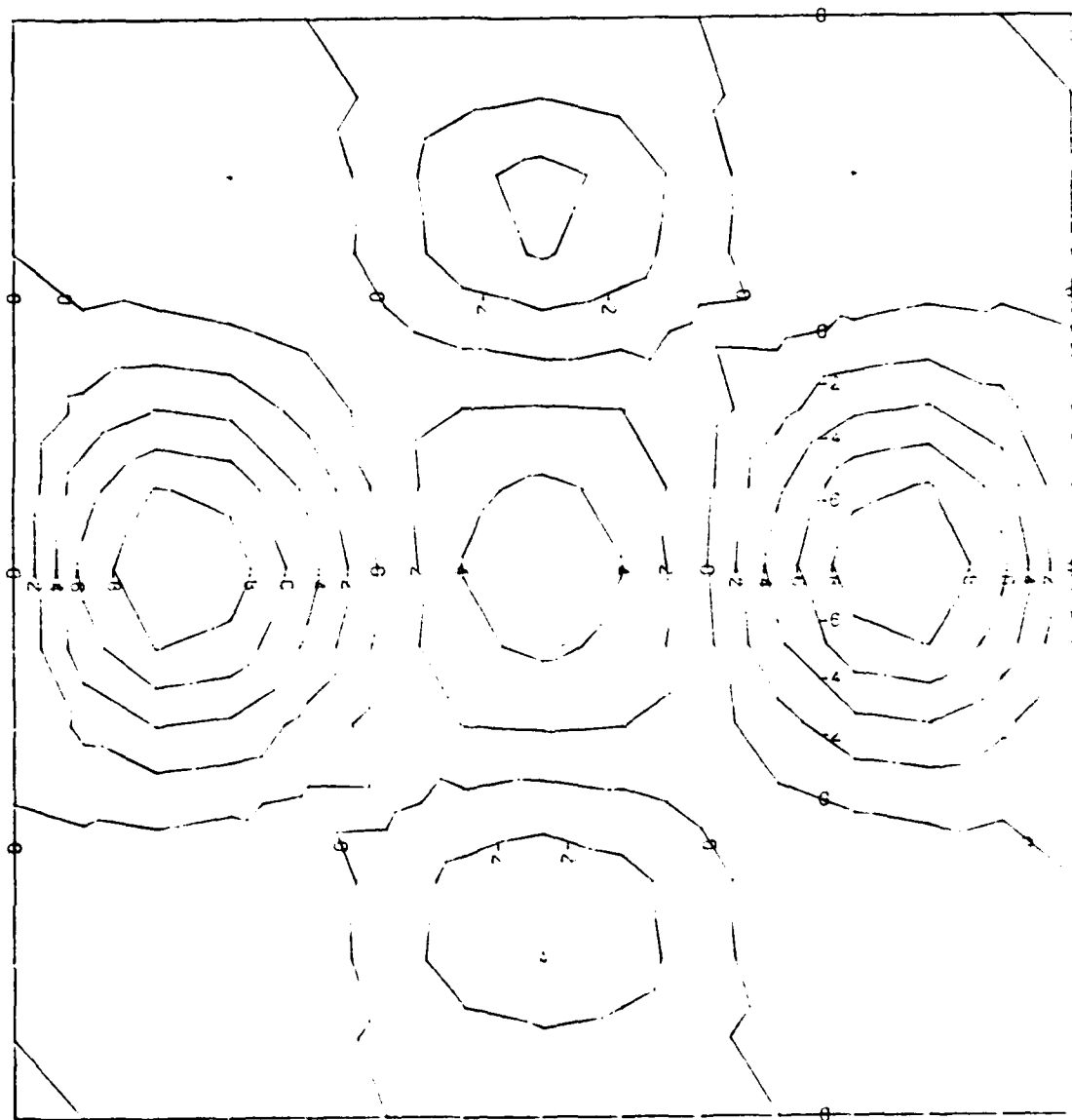


FIGURE 16: W Component Displacement Contours

$[90, 0]_{2s}$

$N_x = 128.5 \text{ lbs/in}$

Positive Contour Levels Are Radial Outward

Maximum Displacement = .049 inch

Displacement Contours In 10^{ths} of Maximum Displacement

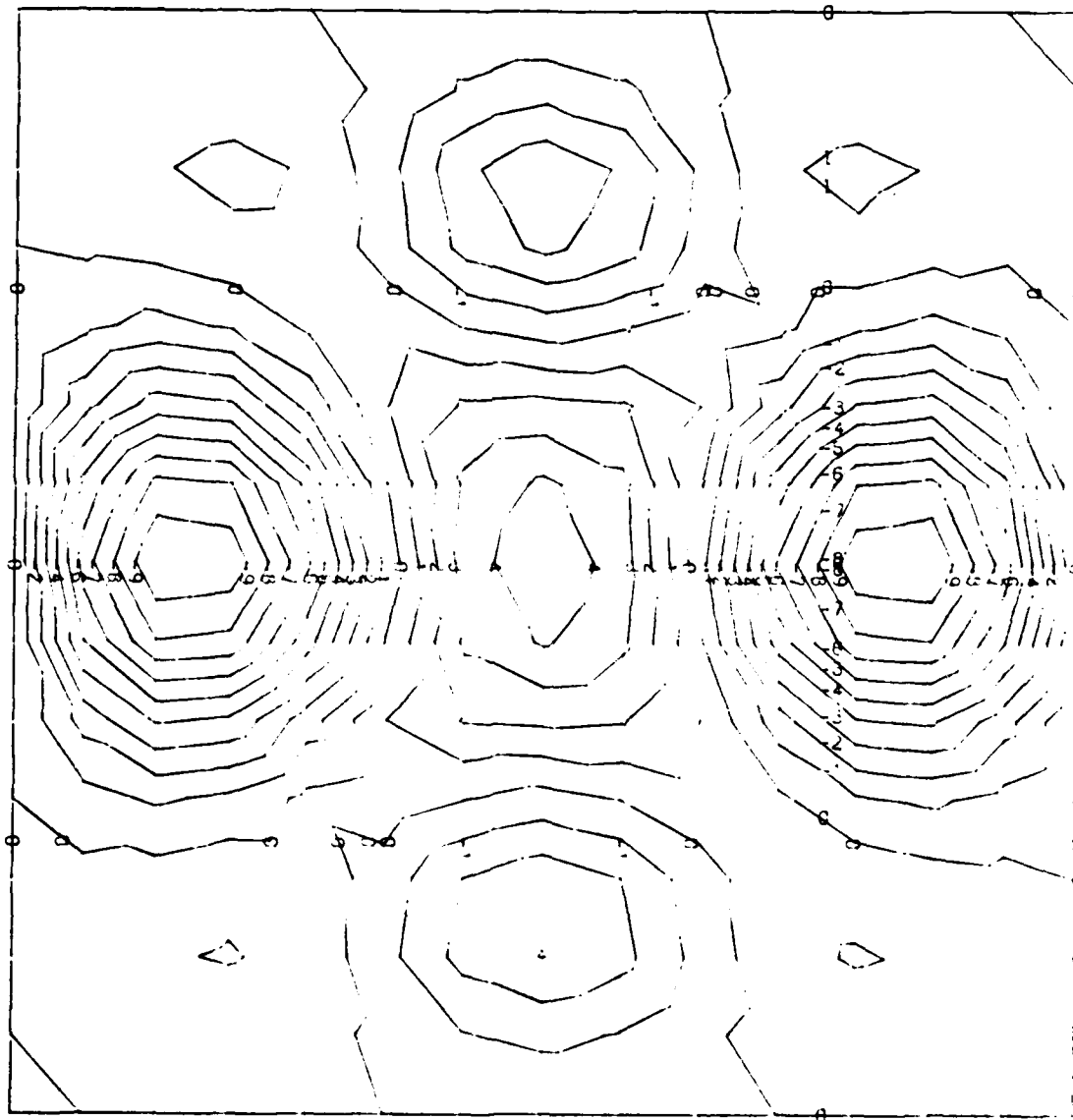


FIGURE 17: W Component Displacement Contours

$[90, 0]_{2s}$

$N_x = 154.4 \text{ lbs/in}$

Positive Contour Levels Are Radial Outward

Maximum Displacement = .076 inch

Displacement Contours In 10^{ths} of Maximum Displacement

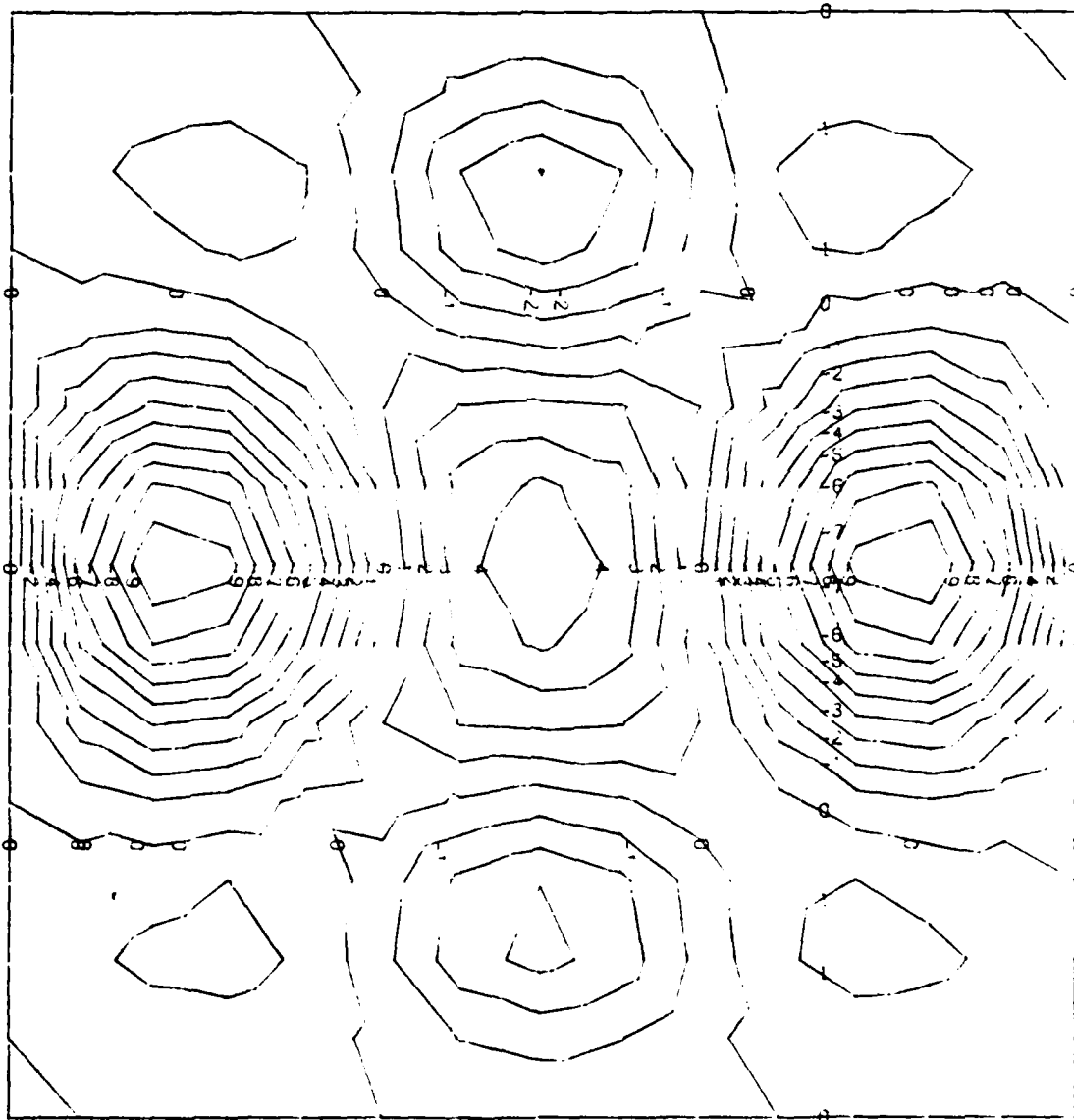


FIGURE 18: W Component Displacement Contours

$[0, +45, -45, 90]_s$

$N_x = 211 \text{ lbs/in}$

Positive Contour Levels Are Radial Outward

Maximum Displacement = .031 inch

Displacement Contours In 10^{ths} of Maximum Displacement

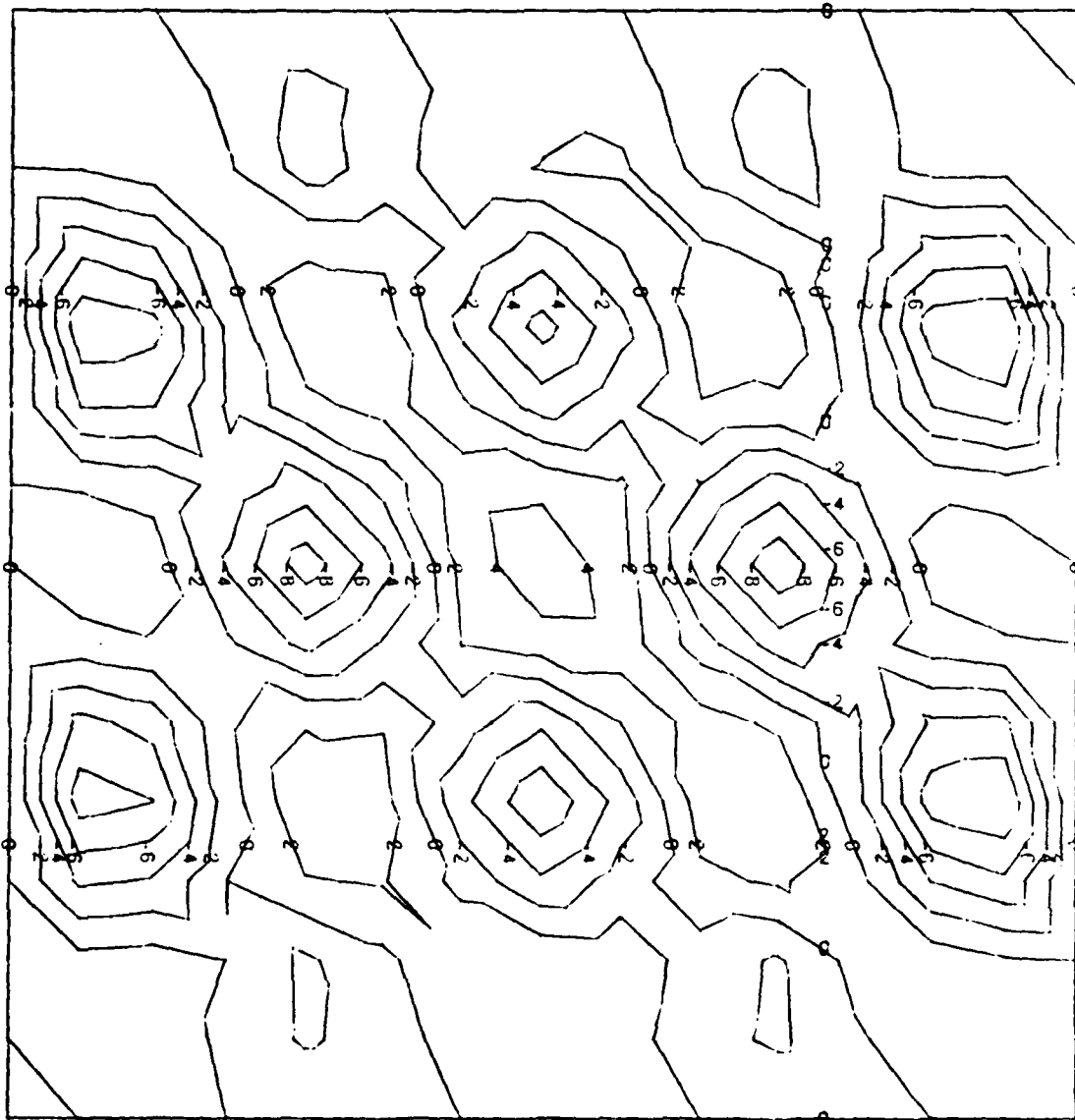


FIGURE 19: W Component Displacement Contours

$[0, +45, -45, 90]_s$

$N_x = 303.5 \text{ lbs/in}$

Positive Contour Levels Are Radial Outward

Maximum Displacement = .0525 inch

Displacement Contours In 10^{ths} of Maximum Displacement

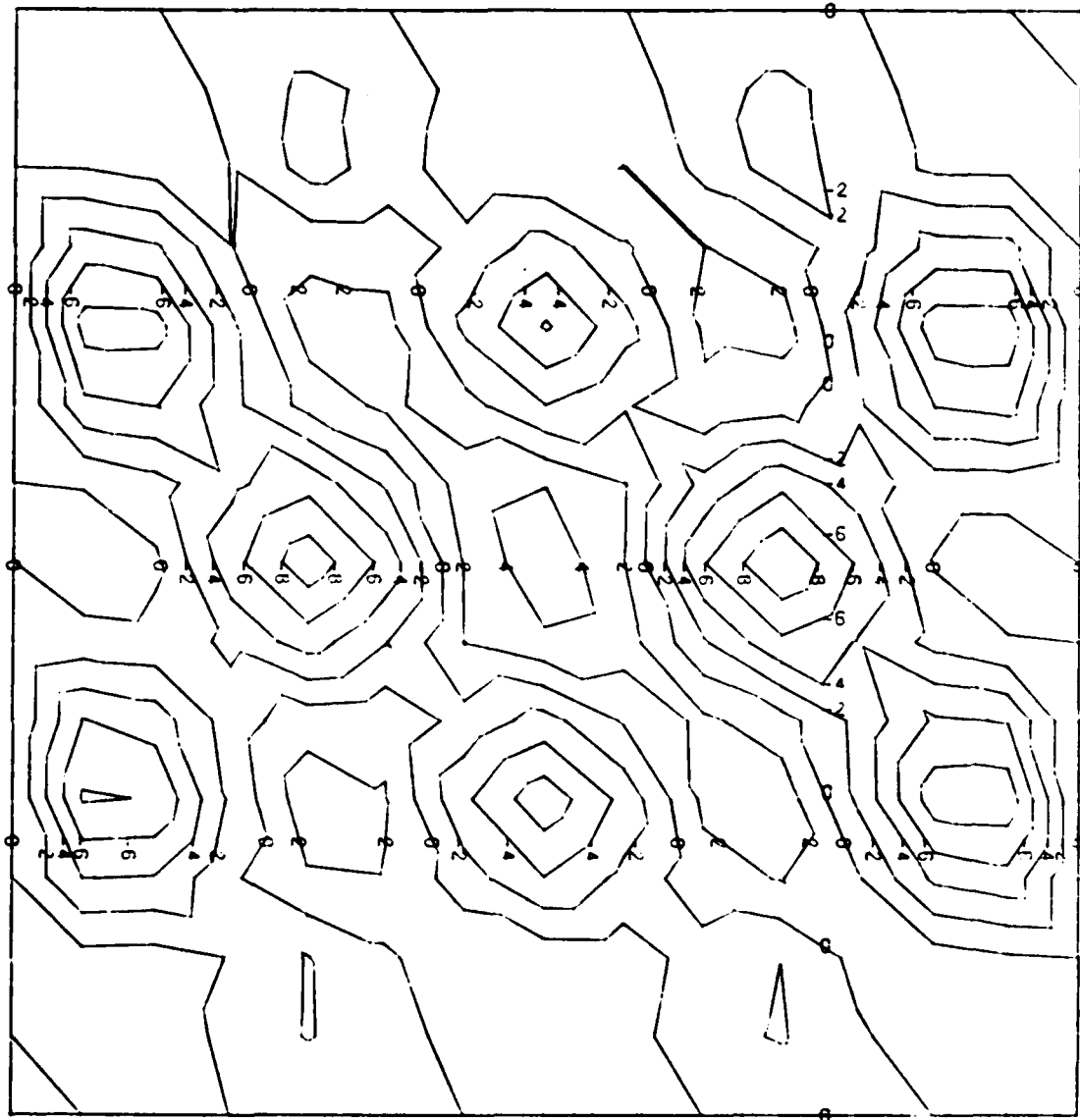


FIGURE 20: W Component Displacement Contours

$[0, +45, -45, 90]_s$

$N_x = 329.6 \text{ lbs/in}$

Positive Contour Levels Are Radial Outward

Maximum Displacement = .0599 inch

Displacement Contours In 10^{ths} of Maximum Displacement

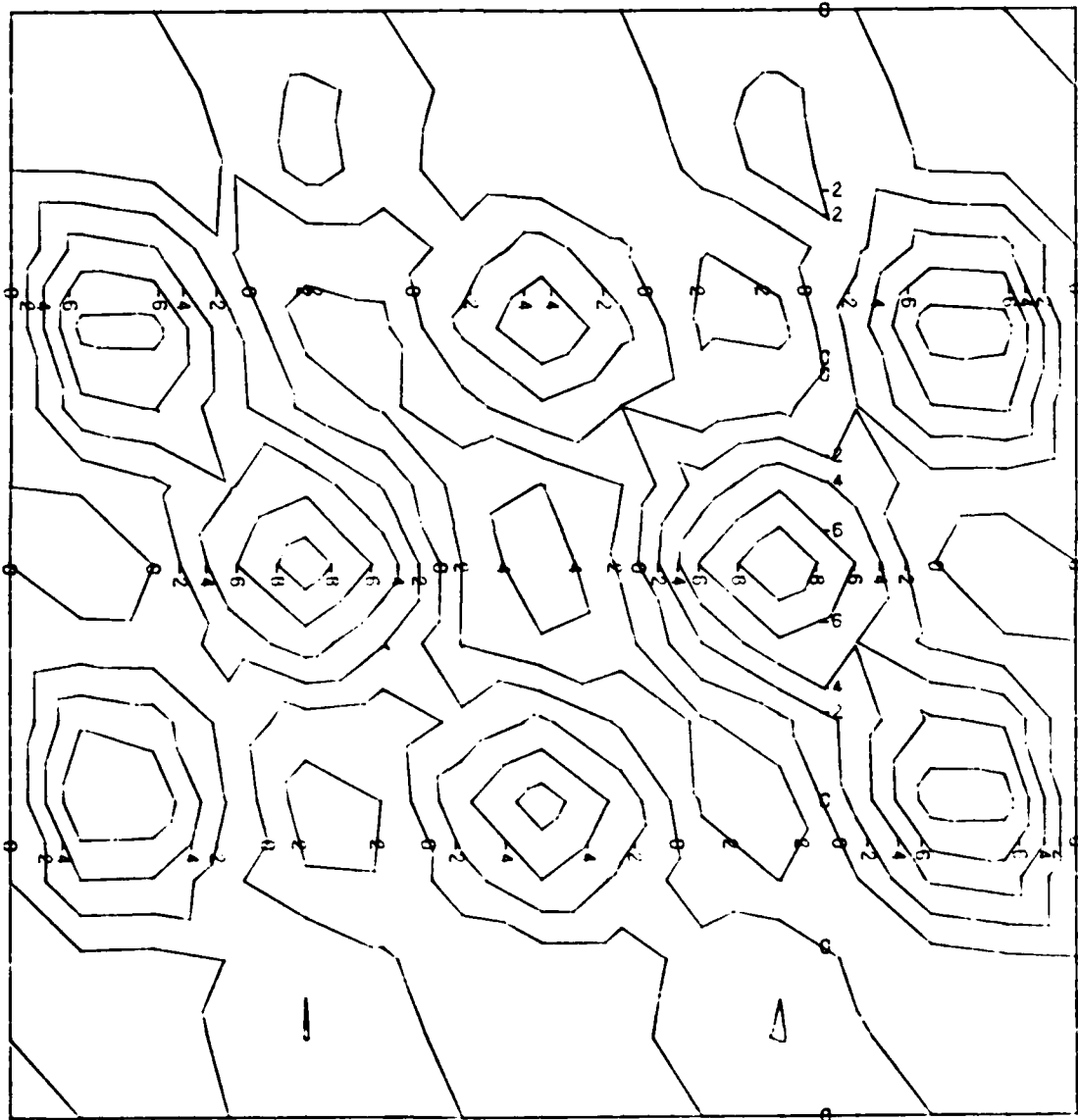


FIGURE 21: W Component Displacement Contours

In examination of the displacement contour plots, it was noted that the radial inward displacement showed a great amount of nonlinearity. The point of maximum inward radial displacement was chosen and its magnitude was plotted against the top edge load intensity (N_x) for each set of panels (Figure 22-23). In viewing these figures, one notices that there seems to be a maximum radial displacement in each set of panels occurring at the collapse load.

In Figure 22, the average maximum radial displacement for the [90, 0]_{2S} set of panels is .068 inches. The average is the sum of the maximum displacement divided by the number of curves. In the five panels considered, the 55 panel had the smallest maximum radial displacement (78% of the average) while the 44 panel had the largest maximum radial displacement (131% of the average). Figure 23 indicates a narrow band of maximum displacement difference for the [0, +45, -45, 90]_s panels. The average maximum radial displacement is .056 inch. All of the panels investigated in this series were within 8% of the average when the panel collapsed. One realizes that the M_x and M_y moment resultants are functions of the radial displacements through the change of curvature and thus they are analyzed next.

Average Radial Displacement .0684 inch

$[90, 0]_{2s}$

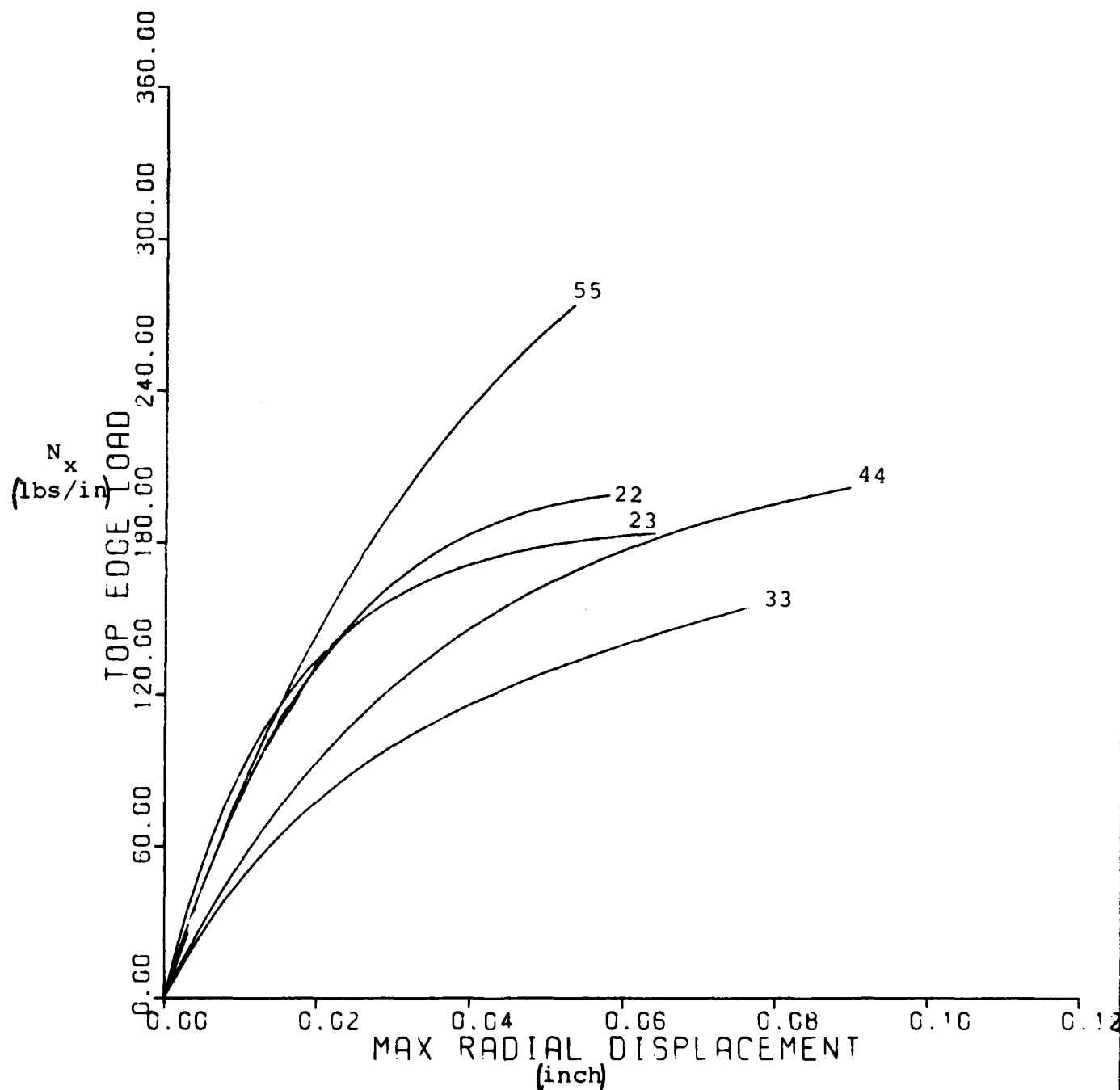


FIGURE 22: Maximum Radial Displacement Versus Top Edge Load
 $[90, 0]_{2s}$ Panel

Average Radial Displacement .056 inch

$[0, +45, -45, 90]_s$

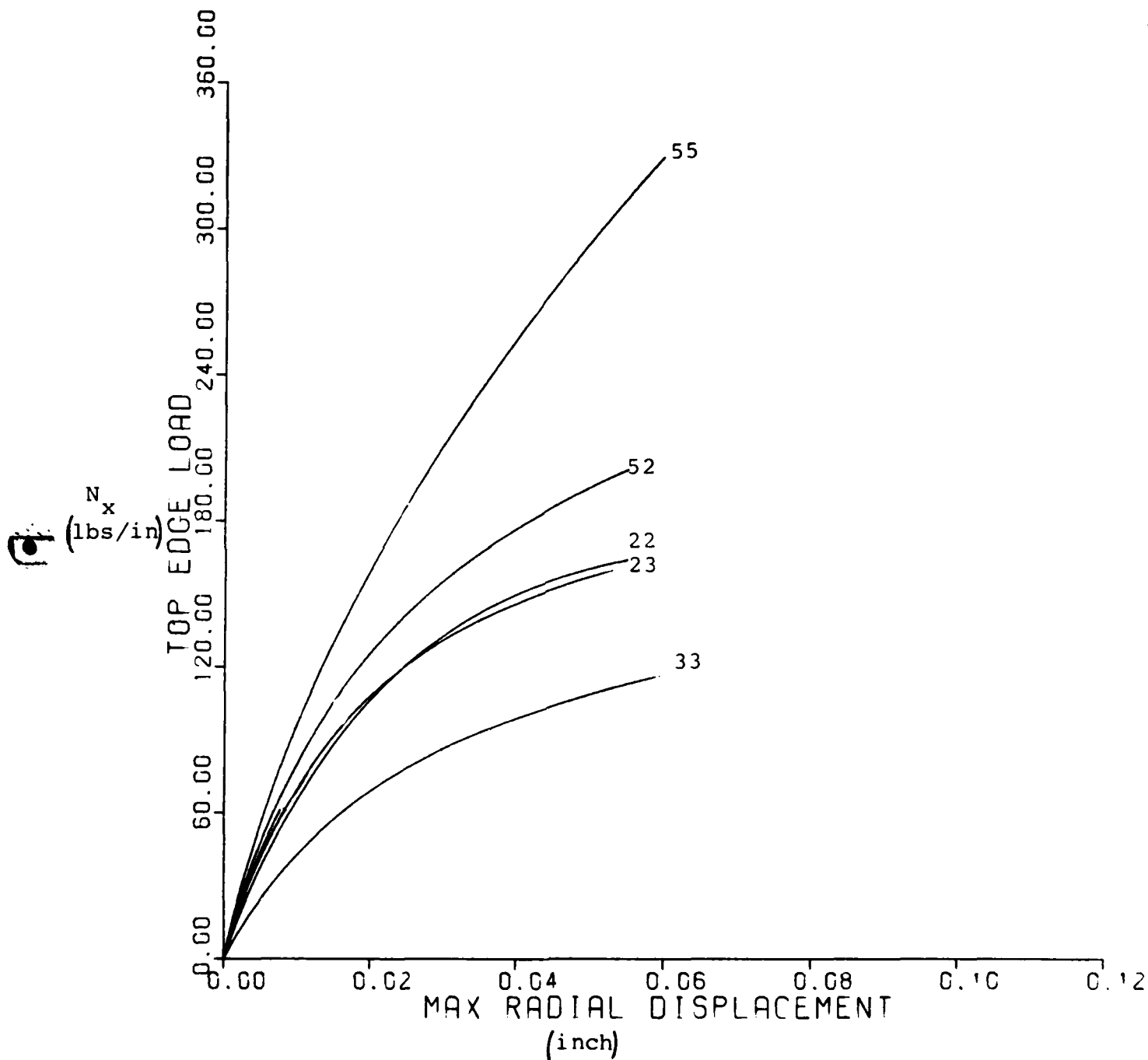


FIGURE 23: Maximum Radial Displacement Versus Top Edge Load
 $[0, +45, -45, 90]_s$ Panel

Figures 24 and 25 are plots of the maximum M_x and M_y resultant for the $[0, +45, -45, 90]_s$ panels. The points of maximum M_x and M_y were the same as the point where the maximum radial displacement occurred. Figures 26 and 27 are the companion figures for the $[90, 0]_{2s}$ set of panels. In viewing the figures, one can see a great amount of nonlinearity appearing, as was demonstrated in the radial displacement. One of the interesting things noted about these figures is that in the $[0, +45, -45, 90]_s$ set of panels (Figure 24 and 25) the M_x resultant is of a larger magnitude than the M_y resultant and the opposite is true in the $[90, 0]_{2s}$ set of panels. This can be explained by the entries in the D_{ij} bending stiffness (See Appendix B for complete array). For the $[90, 0]_{2s}$ panels D_{22} is almost twice as large as D_{11} while in the $[0, \pm 45, 90]_s$ panels D_{11} is over three times as large as D_{22} . Bearing this in mind and examining Figures 24 through 27, for the $[0, \pm 45, 90]_s$ panels, one can see that the M_x resultant is greater than the M_y resultant, because D_{11} is greater than D_{22} . While on the other hand, the $[90, 0]_{2s}$, the opposite is true. One can also see a larger difference in the magnitudes of M_x and M_y in the $[0, \pm 45, 90]_s$ panels. This directly corresponds to the differences in D_{11} and D_{22} in the different sets of panels.

$[0, +45, -45, 90]_s$

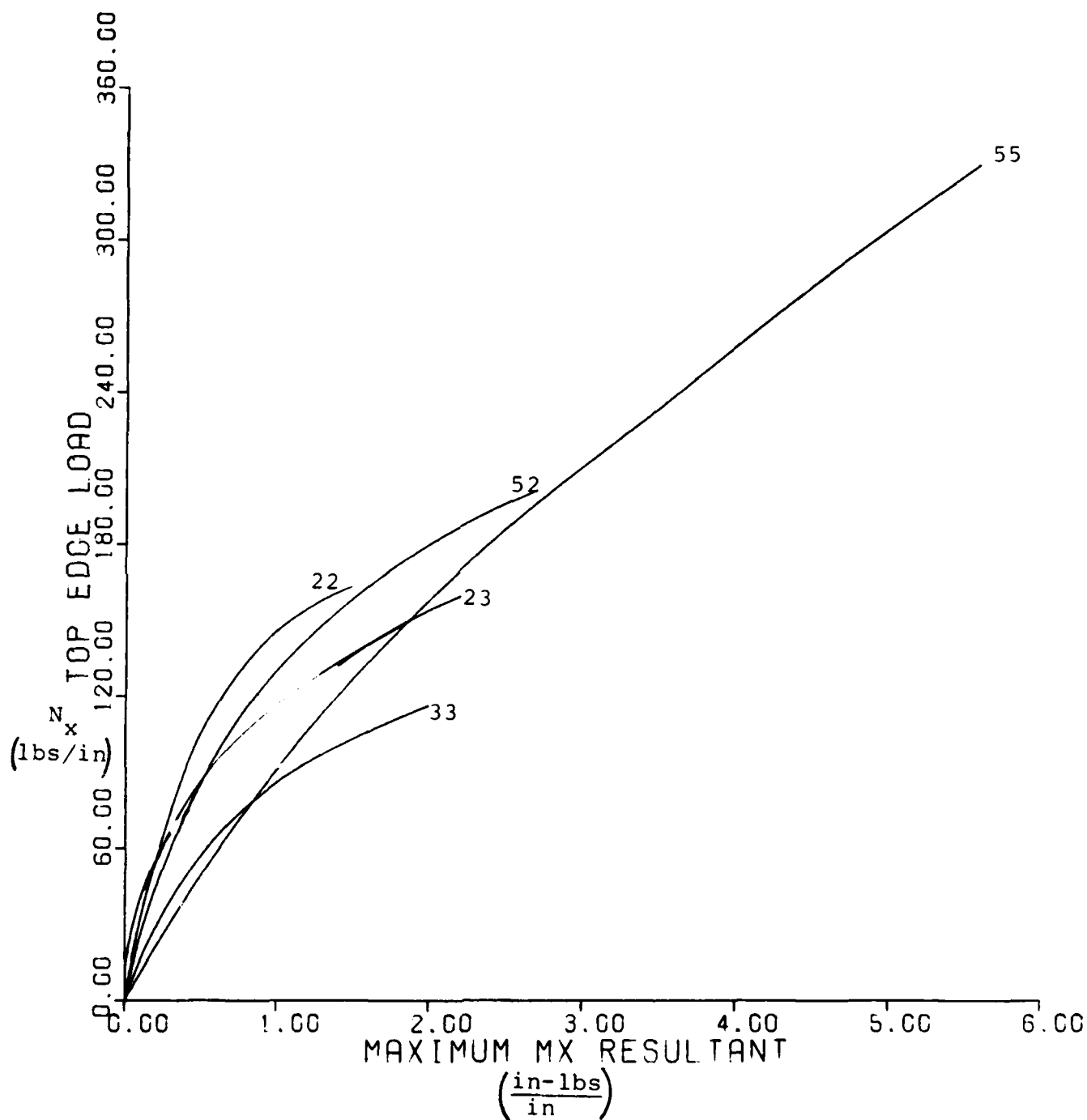


FIGURE 24: Maximum M_x Resultant Versus Top Edge Load

$[0, +45, -45, 90]_s$

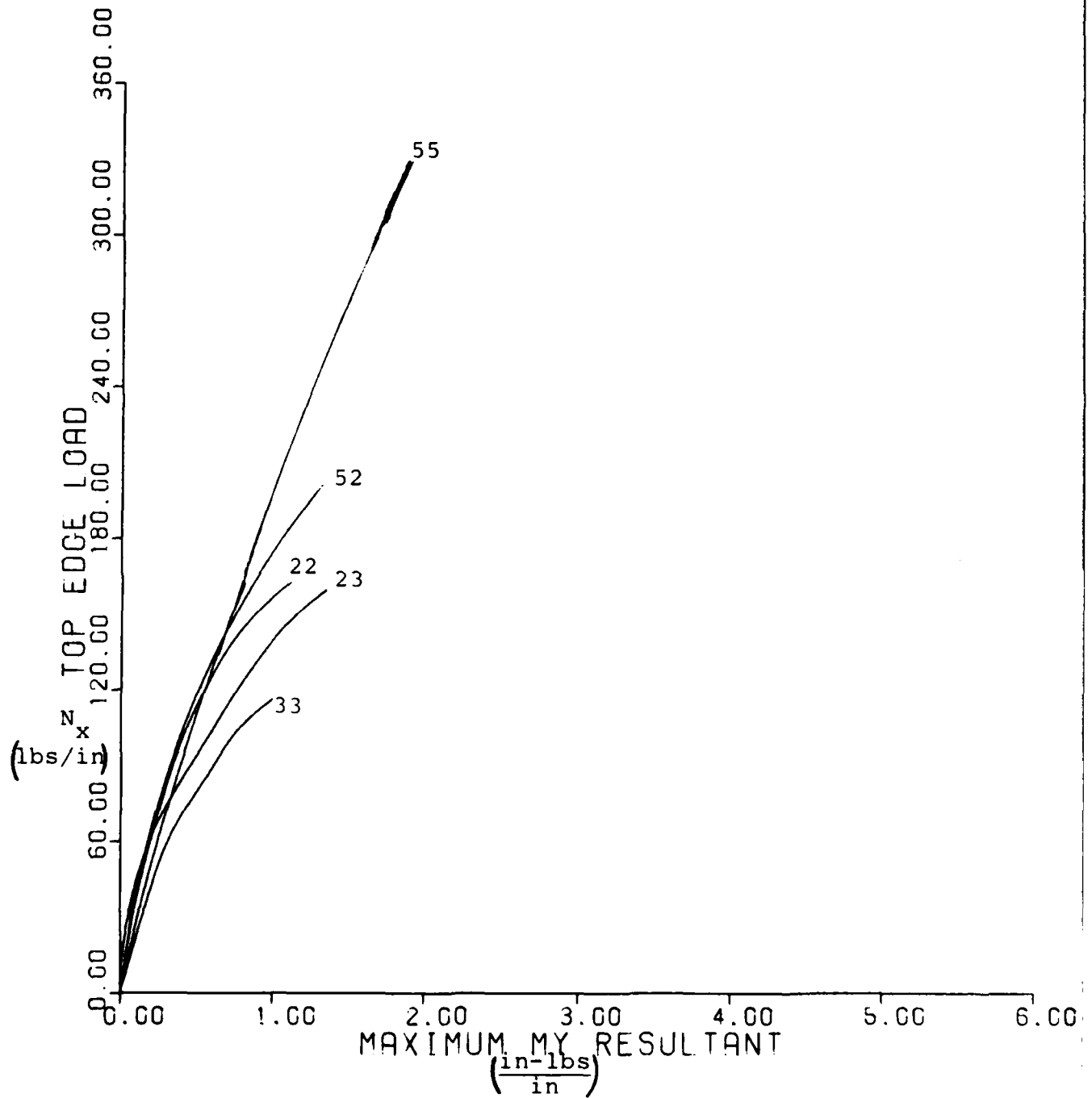


FIGURE 25: Maximum M_y Resultant Versus Top Edge Load

[90, 0]_{2s}

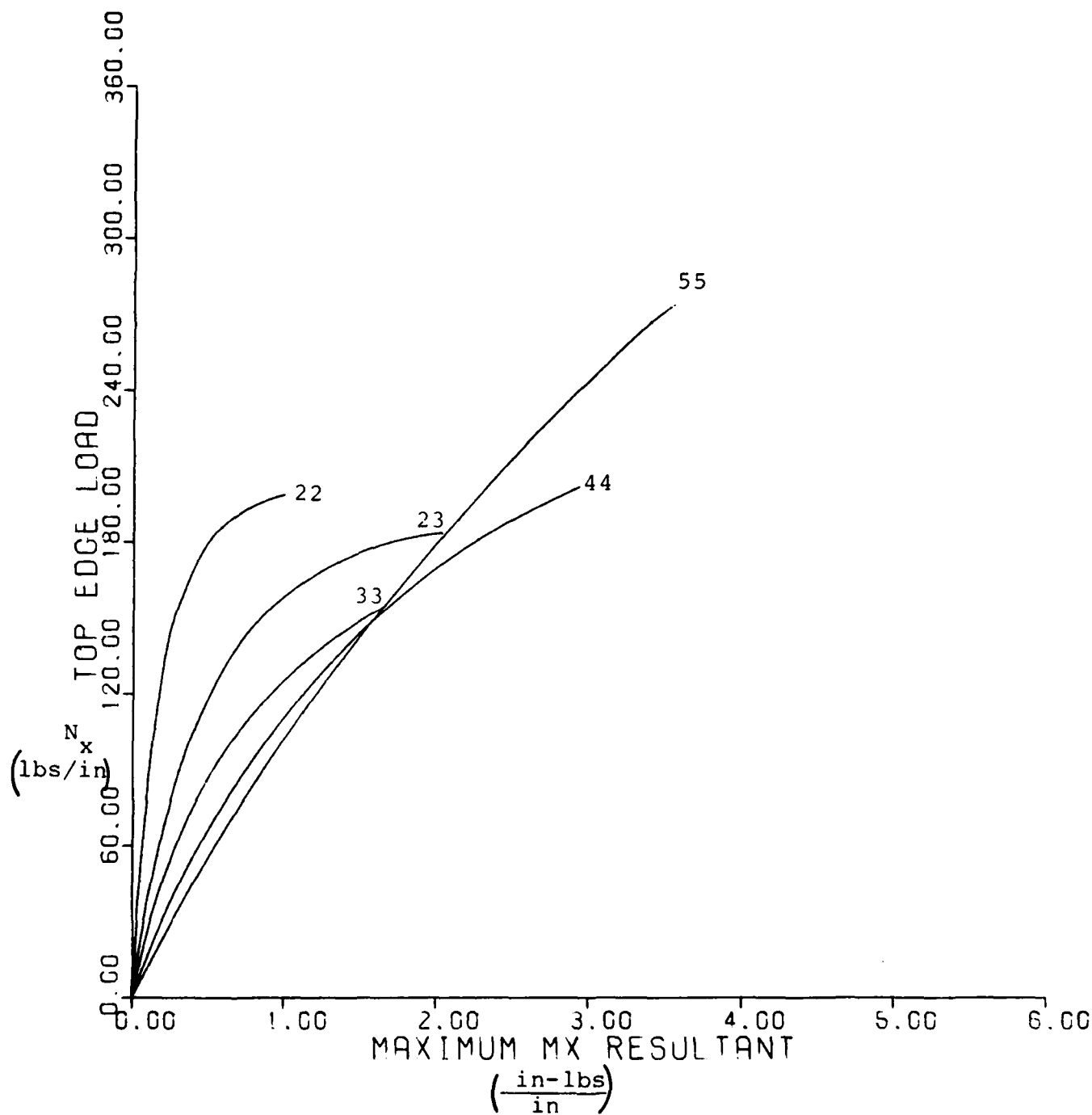


FIGURE 26: Maximum M_x Resultant Versus Top Edge Load

[90, 0]_{2s}

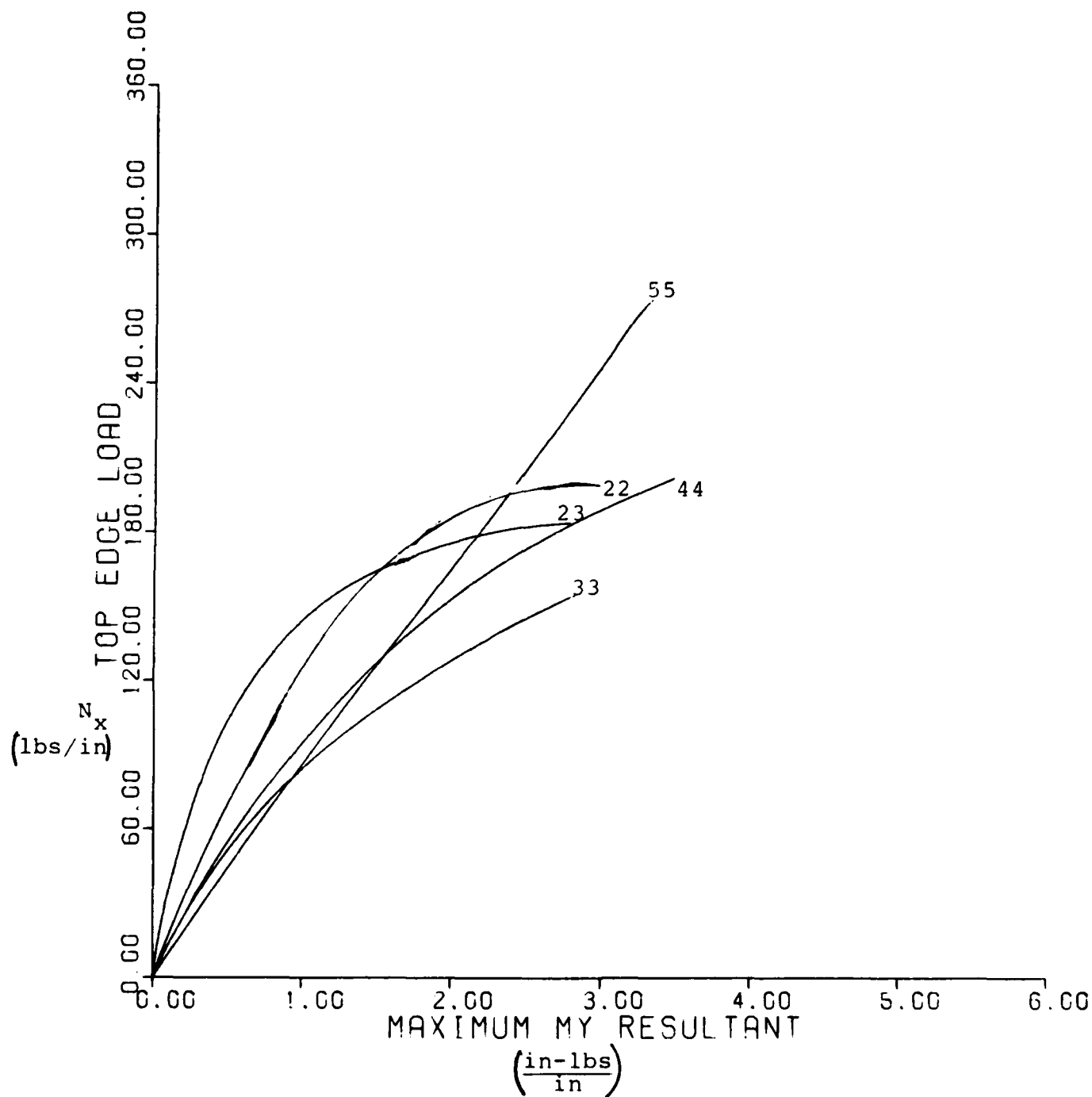


FIGURE 27: Maximum M_y Resultant Versus Top Edge Load

[0, +45, -45, 90]_s

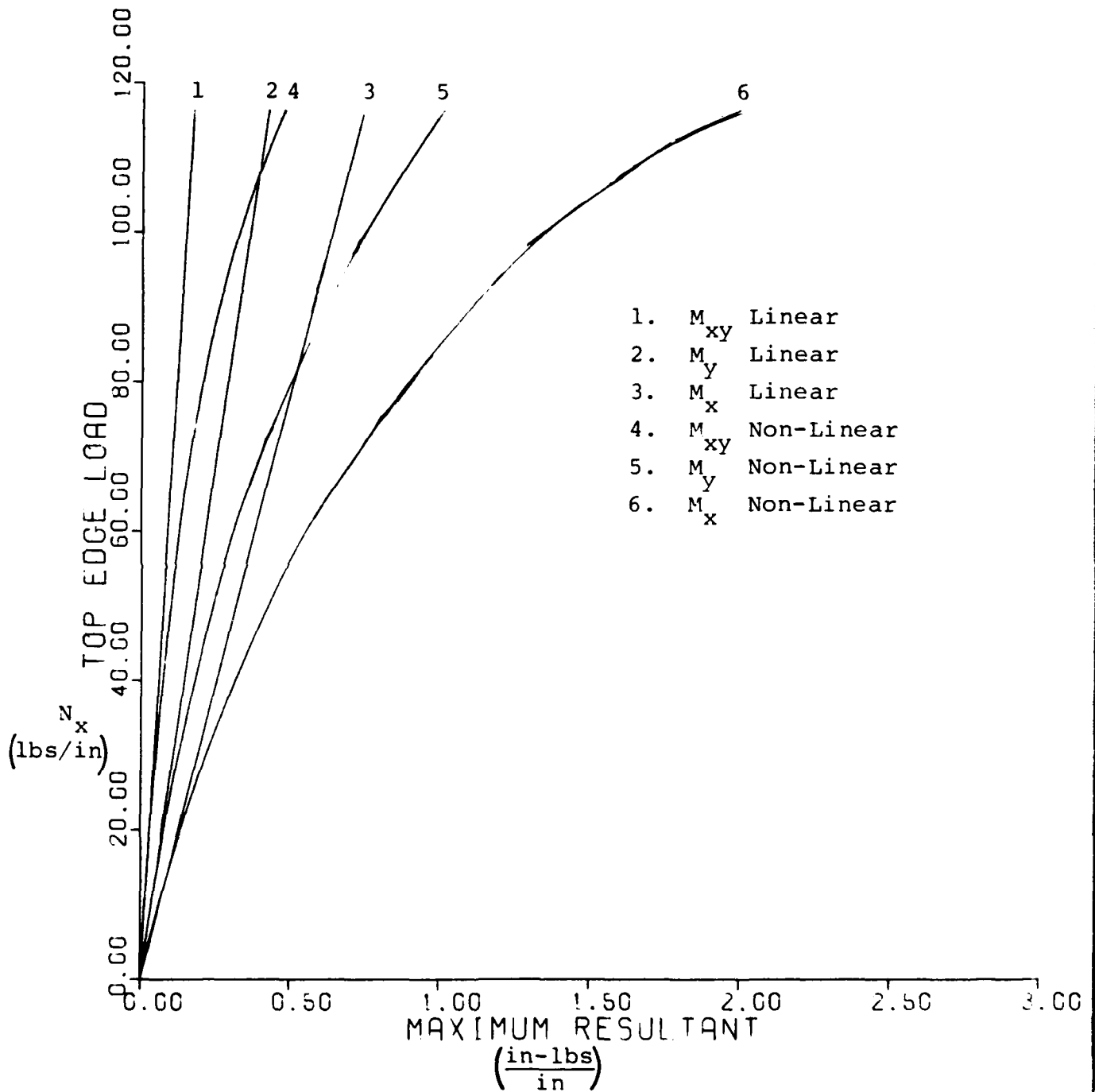


FIGURE 28: Linear and Nonlinear Moment Resultants

As a comparison of the effects of the nonlinear analysis on the moment resultants versus the linear analysis, Figure 28 was plotted. The $[0, +45, -45, 90]_s$ 33 panel was chosen and the three moment resultant M_{xy} , M_x , and M_y were plotted in both the linear and nonlinear analysis. At the collapse load of 116.3 lbs/in the differences are shown in Table 2.

Table 2

Linear Versus Nonlinear Comparison
at 116.3 lbs/in

Moment Resultant	Linear Value	Nonlinear Value	% change Nonlinear to linear
M_{xy}	.073	.481	278
M_x	.744	2.0	268
M_y	.426	1.01	237

The effects of the nonlinear analysis on the resultant moment can be readily seen in Figure 28 and Table 2. This nonlinearity within the moment functions is a by product of any change in curvature created by the radial displacements nonlinearity as discussed previously. This curvature effect is very pronounced as the collapse load is approached and thus the maximum moment resultants become larger and more nonlinear as observed in Figures 27 and 28. In order to reinforce the nonlinear characteristics of moment through the curvature, one may observe in comparing Figures 24 through 28 with Figures 14 and 15 that the nonlinear characteristics of the moments is

more apparent than the nonlinear characteristics of the top edge displacement curve.

Another item that was examined with the moment resultants was how they varied across the center of the panel with increasing load steps. The M_x moment resultant for one panel in each set is illustrated. Figure 29 is the plot of the $[0, +45, -45, 90]_S$ 55 panel and Figure 30 is $[90, 0]_{2S}$ panel. These two panels are representative examples of the two sets, since each panel in the set had the some characteristics. When comparing these two figures with the corresponding displacement contour plots (Figures 16-21) it becomes readily apparent that the maximum moments correspond with the maximum radial displacement and the negative moment resultants are much greater than the positive one. In viewing Figures 29 and 30, one can see that the shape of the moment resultant curve correspond to the shape of the initial imperfection about the midsurface. As the load is increased this symmetry is lost, and the negative moment resultants increases rapidly. Also, the greatest gradient in the moment curves correspond to the steep gradients in the displacement contours. This is due to the fact the moments are a function of the curvature and the curvature is a function of the radial displacements. Where there is a steep gradient, that is a rapidly changing displacement, there will also correspond a steep gradient in the change of the curvature. This steep gradient in the change of the curvature causes the change in the moment resultant.

[90, +45, -45, 0]_s

55 Panel

Load Levels Increase Away From Horizontal Axis

Load Levels (lbs/in) are 91, 186, 286, 329.6

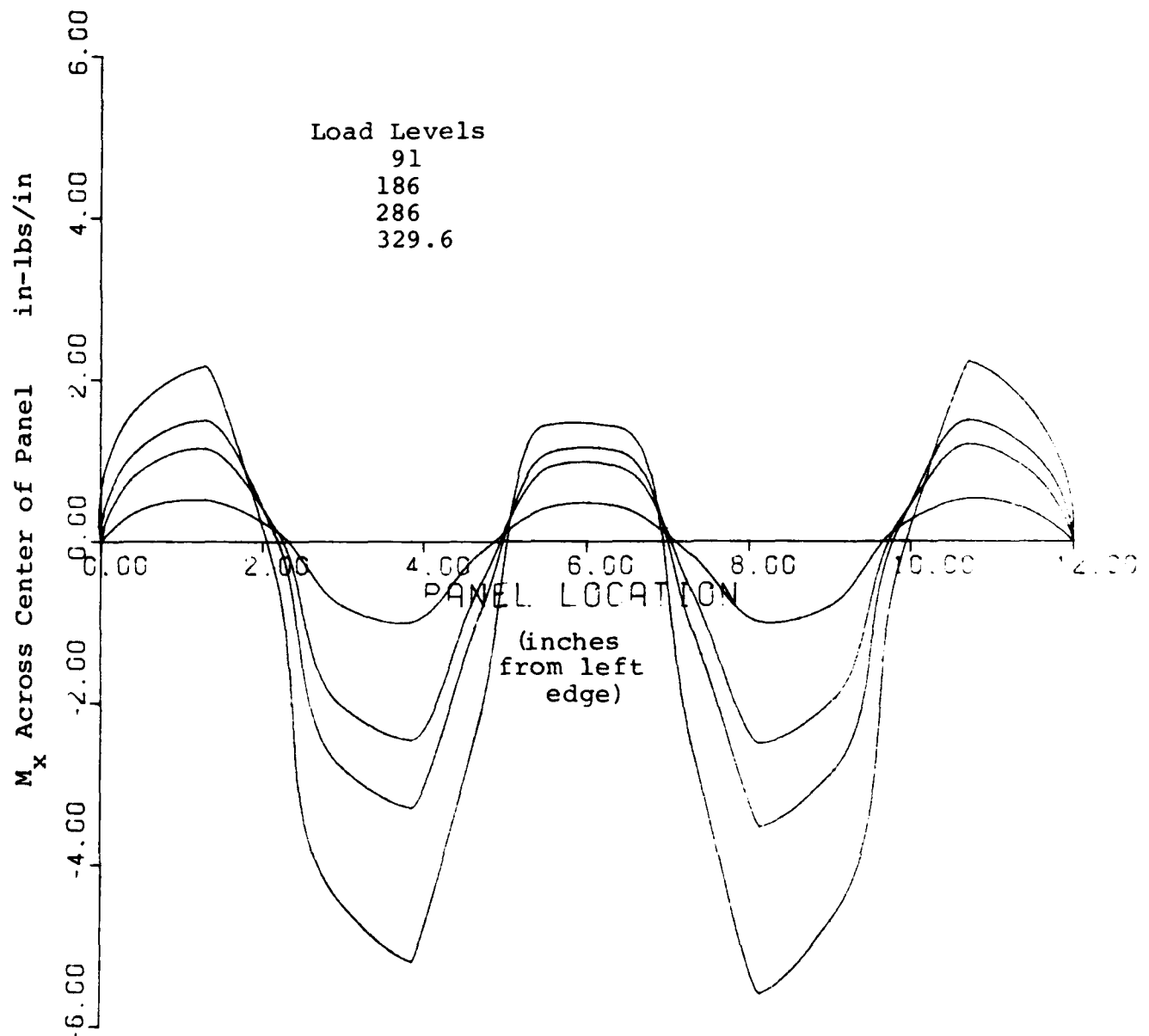


FIGURE 29: M_x Moment resultant Across Center of Panel

[90, 0]_{2s}

33 Panel

Load Levels Increase Away From Horizontal Axis

Load Levels (lbs/in) are 61, 103.5, 128.5, 154.4

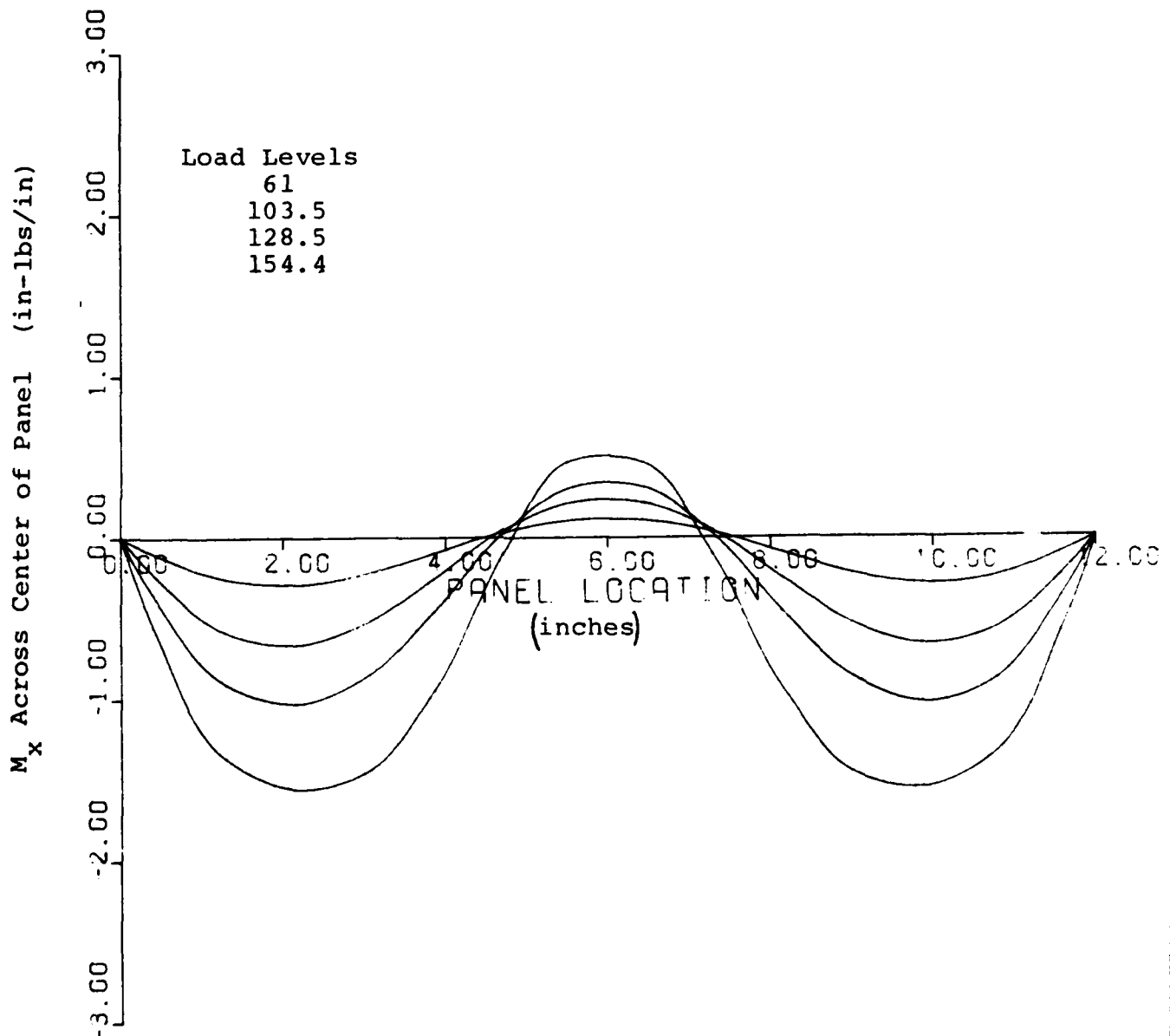


FIGURE 30: M_x Moment Resultant Across Center of Panel

One final item was considered when testing the surface imperfections on the panels. It was noted in some of the research that when a perfect panel reaches its collapse load, the panel will deform into the shape of its eigenfunction [19]. Recalling that the radial displacements followed the initial surface imperfection, it was reasonable to believe that the panel with a surface imperfection of the eigenvector would have the lowest collapse loads. A linear bifurcation was completed on both $[90, 0]_{2s}$ and $[0, +45, -45, 90]_s$ panels and the w component of the eigenvector plotted using contour levels to visualize the shape of the eigenvector (Figures 31 and 32). In viewing the two figures, one can see that the $[90, 0]_{2s}$ panel has an eigenvector in the shape of 4 half sine waves in both directions and is symmetric about the center of the panel. In Figure 32, considering the $[0, \pm 45, 90]_s$ panel the eigenvector shape is approximated by 5 half sine waves across the panel and two down. These two imperfection patterns were tested to see if this would give the lowest collapse load. As already shown in Figures 14 and 15, the collapse load for these two test cases was not the lowest of the cases tested, which came as a surprise.

All of these different observations made on these panels can be tied together by looking at the energy a panel can absorb prior to collapse. When one looks at a perfect panel, the only deformation that occurs is the end shorting. In addition, since there are no imperfections present, the

W Component Mode 1 Eigenvector

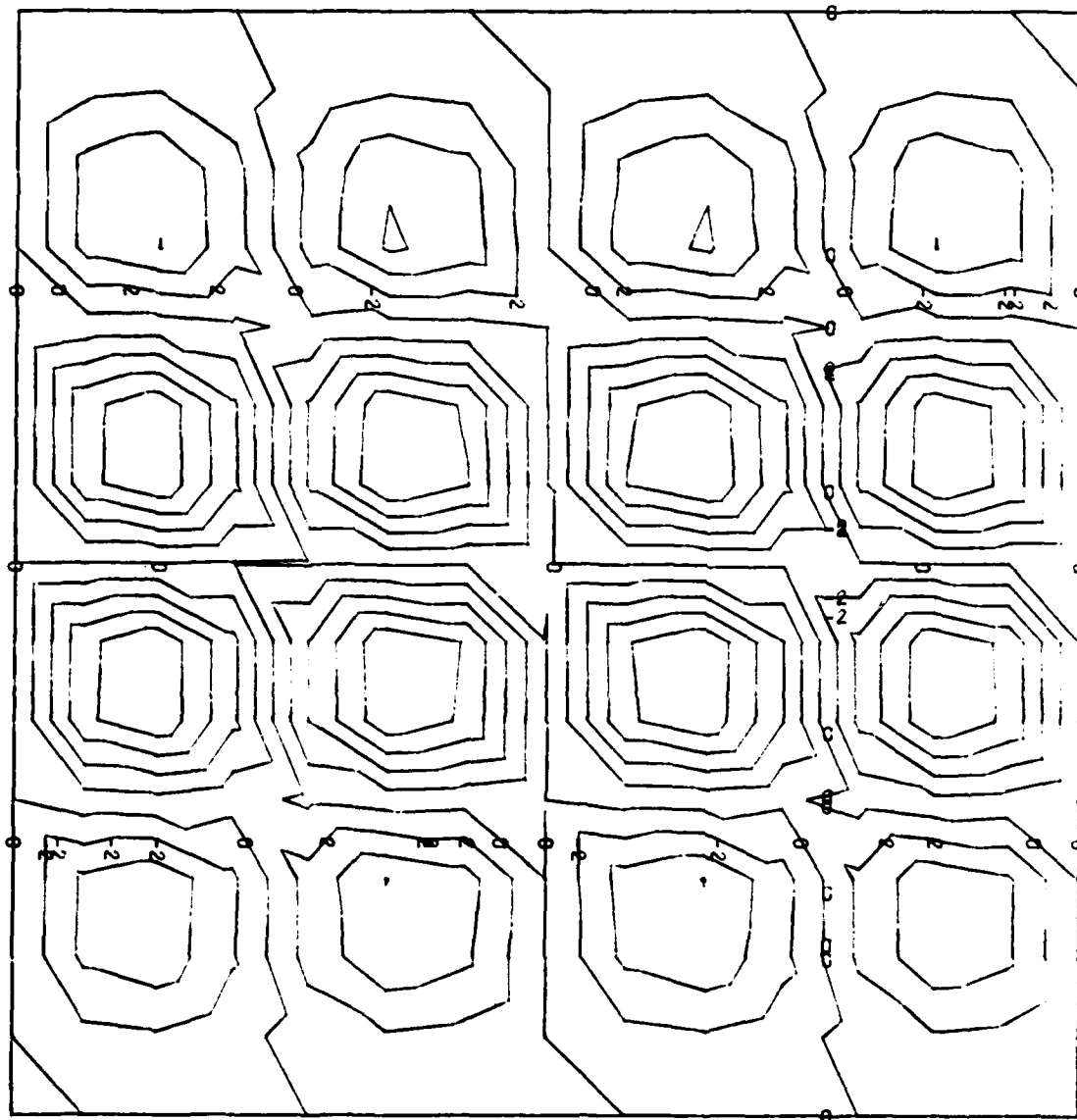


FIGURE 31: Eigenvector Contours $[90, 0]_{2s}$ Panel

W Component Mode 1 Eigenvector

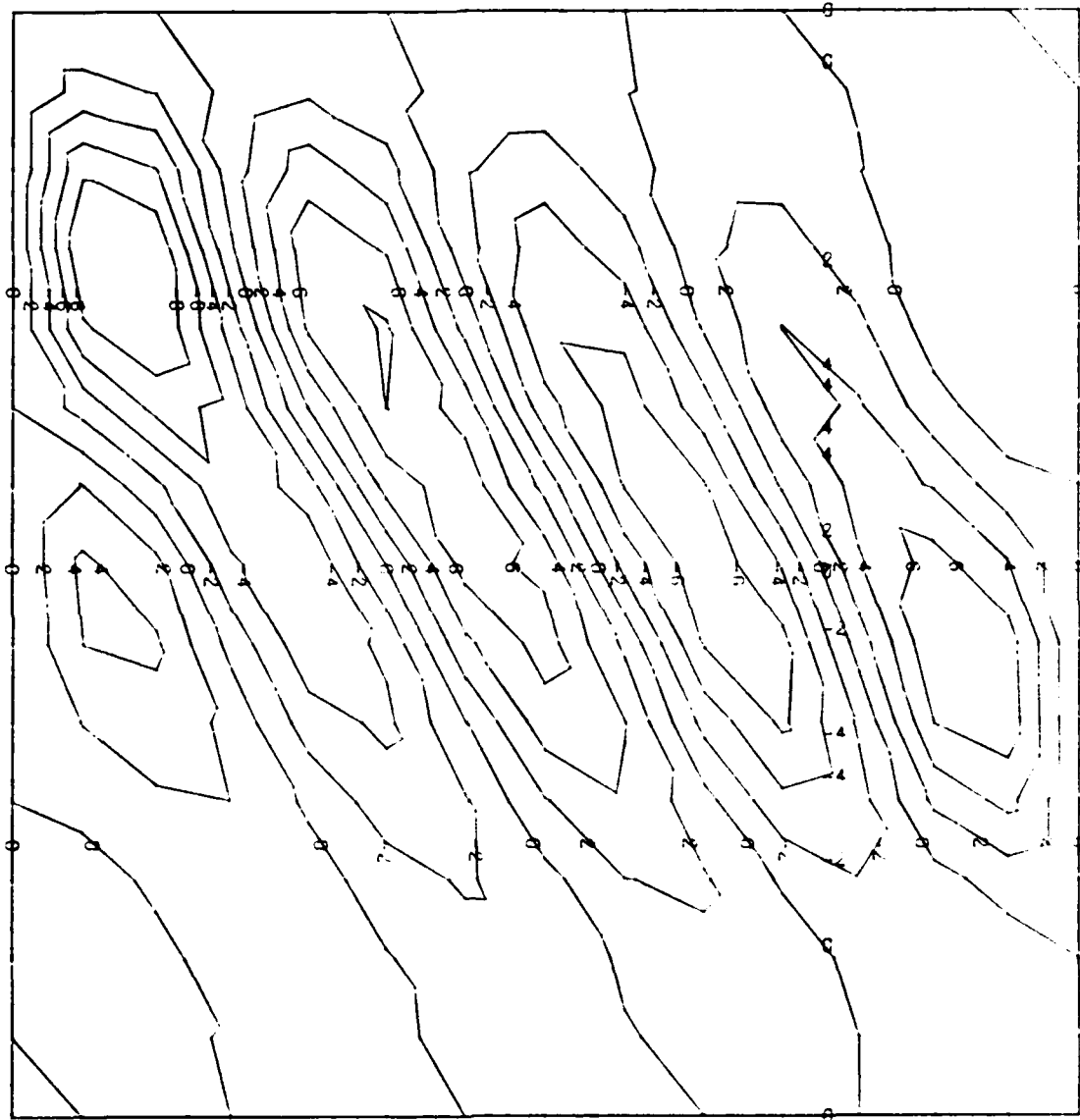


FIGURE 32: Eigenvector Contours $[0, +45, -45, 90]_s$ Panel

surface does not have significant radial displacement until the collapse load occurs. Therefore, the panel is able to absorb energy equally throughout the panel and there are no localized areas where great amounts of energy are accumulated. Thus, the panel can absorb a great amount of energy and has a high collapse load.

When surface imperfections are added to the panel, these localized areas will become "energy hot spots". That is, as the panel is loaded into compression the moment resultants will build in the areas of the imperfection faster than in the other areas due to the changing radial displacement pattern. Since the energy is a direct function of the moment and curvature as well as the membrane force and inplane displacements the imperfection sites become localized areas of higher concentrations of stored energy, that is "energy hot spots". The number of imperfections therefore will dictate the number of "energy hot spots".

With large surface imperfections, absorbed energy will be spread over a larger area than if the imperfection were smaller. This explains why the 22 panels were able to have a higher load bearing capability than the 23 and 33 panels. All these panels had relatively large surface imperfections. As the area of the surface imperfection decreased, that area was not able to absorb as much energy and the panel would collapse. Keep in mind that the magnitude of the imperfection was the same in all cases.

The question then arises, why was the 33 panels the weakest instead of the 55 panels. As the number of imperfection become greater, and the area they covered become smaller they begin to interact. Each imperfection still absorbs energy, but when the shape of the imperfection is looked at closely the answer is revealed. For example, take two surface imperfections next to each other with their amplitudes opposite one another.

As the panel is loaded, each imperfection tries to displace in the shape of the individual imperfection. Therefore, as they both try to displace in opposite directions they begin to react with one another and store the energy internal rather than being able to displace. Therefore, the absorbed energy is now being absorbed by a greater area of the whole panel, much like the perfect panel. There are still localized "hot spots of energy", but the difference in magnitude around the panel is closer to being uniform, rather than just a few areas. In recap-ping what happens, as surface imperfections are added to a panel, localized areas of absorbed energy appear and the panel will not be able to absorb as much as a perfect panel, therefore, the collapse load is smaller. As the number of imperfections increase, the "energy hot spots" begin to react and start to keep the absorbed energy pretty well constant throughout the panel, therefore, the panel starts to gain some of its strength back. A few large imperfections will weaken a panel while many small imperfections will give some of its initial strength back. The last idea is very much like the folded plate concept where the ridges stiffen the plate.

Analytical Study of Panels With Cutouts

In order to understand the effect that a true geometric imperfection has on a composite panel, a study of the effect a discontinuity has on a panel has been carried out. The geometric discontinuity will be a cutout in the center of the panel. This portion of the study, just like the surface imperfections, will be interested in the collapse load, displacement pattern in the radial direction, and moment resultants. The panel size and notation are the same as used previously and shown in Figure 5. The 411 element has been incorporated into the finite element model with a 13 by 13 grid. Three different ply layups with two different size cutouts have been analyzed and are shown in Table 3.

Table 3

Ply Layup and Cutout Size

Ply Layup	Cutout Size (inches)
$[0, +45, -45, 90]_S$	2X2 and 4X4
$[0, -45, +45, 90]_S$	2X2 and 4X4
$[90, +45, -45, 0]_S$	2X2

The 2 inch by 2 inch cutout removed 2.78% of the panels total area and the 4 inch by 4 inch cutout removed 11.1% of the total area.

The boundary conditions for all five of the panels evaluated in Table 3 are the same as used on the panels with surface imperfections. That is u free on top, bottom of the panel clamped with no free DOFs and the sides of the panel u , v , and the rotation about u are free. One other panel was examined with a different boundary condition. A $[0, +45, -45, 90]_s$ panel with a 2 inch by 2 inch cutout was analyzed with the same boundary conditions on the top and bottom of the panel and on the vertical sides only u and the rotation about u was free. A nonlinear collapse analysis was performed in all six of the different panels the following results were observed.

A graph of the top edge load versus the top edge displacement is shown in Figure 33 for the panels with cutouts. As can be seen in the graph, the cutouts affect the load bearing capability of the panel. When considering just the linear bifurcation of the panels, it can be seen that the presence of a cutout greatly reduces the load bearing capability of the panel and its stiffness. The linear bifurcation of the panels shown in Figure 33 is for a $[0, +45, -45, 90]_s$ ply layup with the indicated cutout. By changing the orientation of the 45 degree plies with each other, one did not find a change in the bifurcation load or top edge displacement. Thus, the lines are the plots of the linear bifurcation for both the $[0, +45, -45, 0]_s$ and $[0, -45, +45, 90]_s$ panels with their respective cutouts. The linear bifurcation of the

● [0, +45, -45, 90]_s Panels
 - [90, +45, -45, 0]_s Panel

Cutout Size	Ply Layup	Collapse Load	Linear Bifurcation
2X2	[0, +45, -45, 90] _s	215.9	252.14
2X2	[0, -45, +45, 90] _s	215.9	252.14
2X2	[90, +45, -45, 0] _s	223.6	205.0
4X4	[0, +45, -45, 90] _s	131.2	113.2
4X4	[0, -45, +45, 90] _s	131.2	113.2
4X4	[90, +45, -45, 0] _s		74.32

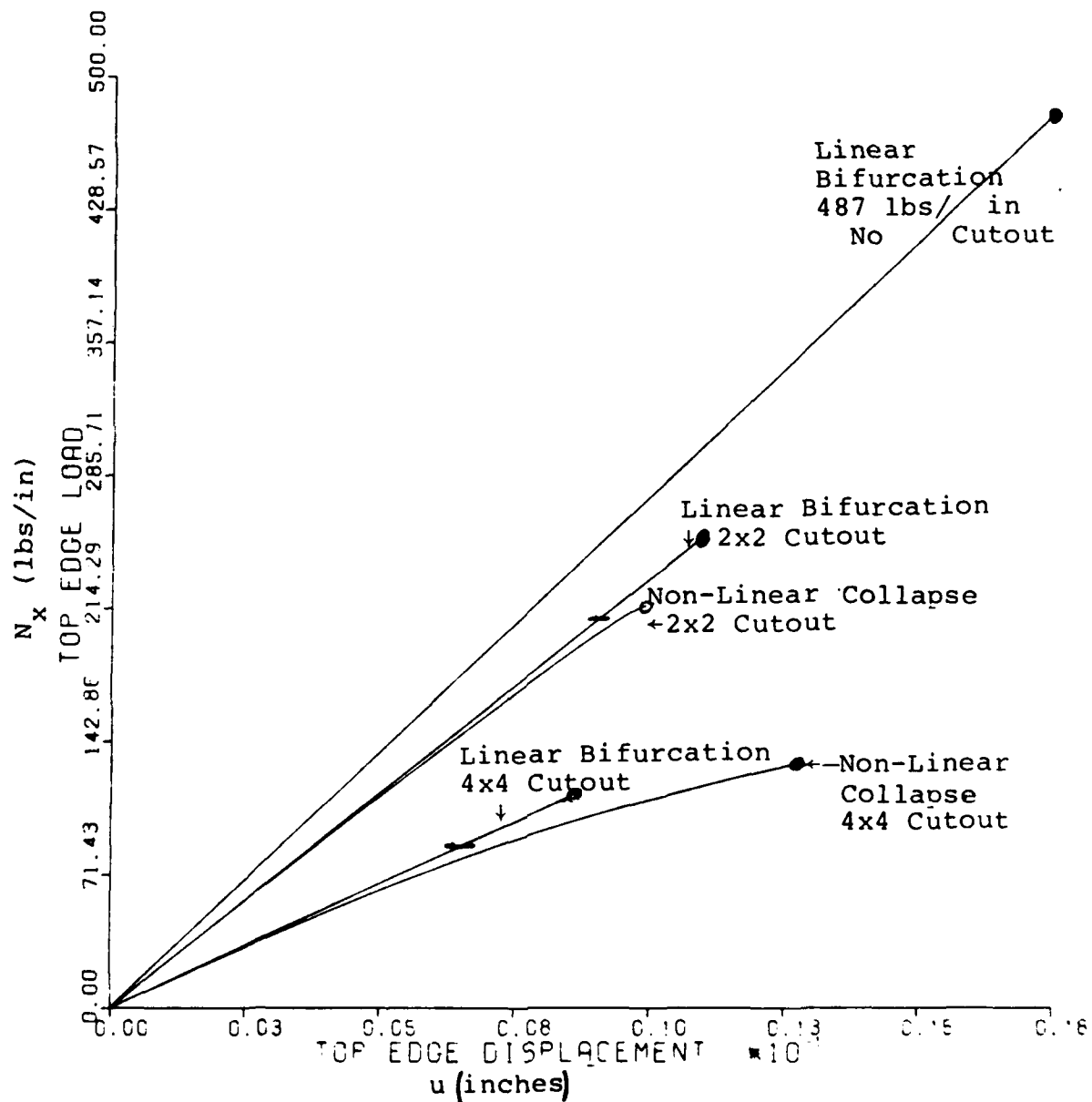


FIGURE 33: Top Edge Load Versus Top Edge Displacements

[90, +45, -45, 0]_s panels has the same axial stiffness as the [0, +45, -45, 90]_s panels. However, their load bearing capability is reduced. Because the axial stiffness is the same for the two panels, the plots of the top edge load versus the top edge displacement overlay one another. One notices that the panels with the two inch by two inch cutouts have the bifurcation load is reduced to 81% of the [0, +45, -45, 90]_s panels bifurcation load (252 lbs/in to 205 lbs/in. See hash mark on a linear bifurcation 2X2 cutout plot in Figure 33). The 4 inch by 4 inch cutout panel had its bifurcation load reduced to 65% of the [0, +45, -45, 90]_s panels bifurcation load (113.2 lbs/in to 74.3 lbs/in). In other words, it can be seen from the linear bifurcation that the different ply layup did not affect the axial stiffness of the panel. However, the load bearing capability of the panel with the zero degree outside ply has the largest bifurcation load. This is because of the change in the bending stiffness array (See Appendix B).

When the nonlinear collapse analysis was performed, a couple of interesting things were noticed about the load bearing capability of the panels and their top edge displacements. The panels with the three different ply layups and 4 square inch cutouts all had the same top edge displacement, at their respective collapse loads, of .0103 inch. The collapse load for the [0, +45, -45, 90]_s panel was exactly the same as the [0, -45, +45, 90]_s panel at a load of 215.9 lbs/in. The collapse load for the [90, +45, -45, 0]_s panel was a little

higher (3.4%) at 223.6 lbs/in. Since they are so close to one another they are represented in Figure 33 as the same curve for the nonlinear analysis. Referring to Figure 33, one can see that the zero degree outside ply panels had a collapse lower than the linear bifurcation load. However, the panel with the 90° outside ply had a collapse load higher than its respective linear bifurcation. The collapse load for the 2 inch by 2 inch cutout panel in the nonlinear analysis falls in between the two different bifurcation loads and top edge displacements (See Figure 33).

This item can be explained by considering the stiffness matrix for the panels and the effects the small cutout has on a nonlinear collapse analysis. In the straight linear bifurcation the panels had the same axial stiffness and because of the bending stiffness the panels with the zero degree outside plies were able to withstand the greater load. When the nonlinear collapse analysis was done, the radial displacements and the nonlinearity of the cutout comes into play. Since the load is applied in the zero degree direction (axial compression) the cutting of this ply orientation by the cutout produces a reduced bending stiffness. Therefore, the panel with the zero degree outside plies will allow the panel to displace radially more than the panels with the 90° outside plies. Taking this into account, the panels with the 90° outside plies will have a higher collapse load (be able to absorb more energy) than to zero degree outside ply panels.

Therefore, when compared to the linear bifurcation analysis, the load bearing capability for the 90° outside ply panels will increase in the nonlinear collapse analysis, and likewise, the 0° outside panels will have the opposite effect. This is the reason why the nonlinear collapse analysis of the 2 inch by 2 inch cutout is very close to the same for both ply orientations and why it falls in between the two linear bifurcations.

In looking at the effect a 4 inch by 4 inch cutout had on the panels, one will notice a different effect than the 2 inch by 2 inch cutout had (Figure 33). The nonlinear collapse load of the 4 inch by 4 inch cutout was higher than both of the different bifurcation loads. This is because in the nonlinear collapse analysis the radial displacements along the cutout edges will play a greater part in absorbing energy than the 2 inch by 2 inch cutout and the linear bifurcation of the 4 inch by 4 inch cutout panel. By having the larger cutout, radial displacements along the cutout edges are less constrained in the radial direction and will allow greater amount of bending. Therefore, the panel will be able to absorb more energy (higher collapse load) than the linear bifurcation value and will have a larger top edge displacements.

Briefly in reviewing, the 2 inch by 2 inch cutout nonlinear analysis does not effect the panels load bearing capability that greatly compared to the linear cutout analysis because of the small amount of area removed, and the length of the cutouts edges. This is due to the fact that the radial

displacements along the cutouts edges are not as large as those of a panel with a larger cutout. Therefore, there is less bending in the panel for the smaller cutout and its nonlinear collapse load will be close to the bifurcation load. As the cutout gets larger in size, the radial displacements along the edge of the cutout will play a greater effect in the nonlinear analysis and thus will have a larger moment effect. One will notice when an area is removed from panel the overall bending stiffness is reduced in the area of the cutout. Since the general resistance in a panel is axial, a reduction in the bending stiffness makes the overall axial resistance less. Therefore, the larger cutout will have a greater top edge displacement when compared to the linear bifurcation and the collapse load will be higher because of the greater moment due to the larger radial displacements. However, the presence of a cutout will greatly reduce the strength of a panel when compared to the uncut panel (See Figure 33).

After seeing the effect that the radial displacements had in the nonlinear collapse of the cutout panels, they were studied further. Figures 34 through 38 are the w component displacement contours of the panels with a 2 inch by 2 inch cutout (small cutout). In examining these figures, one can see a difference in the displacement pattern then that experienced by isotropic panels. That is, at collapse the symmetry is lost.

Load Level 81 lbs/in

Maximum Displacement = .0086 inch

Ply Layup $[0, +45, -45, 90]_s$

Contour Levels Are In 10^{ths} of Maximum Displacement

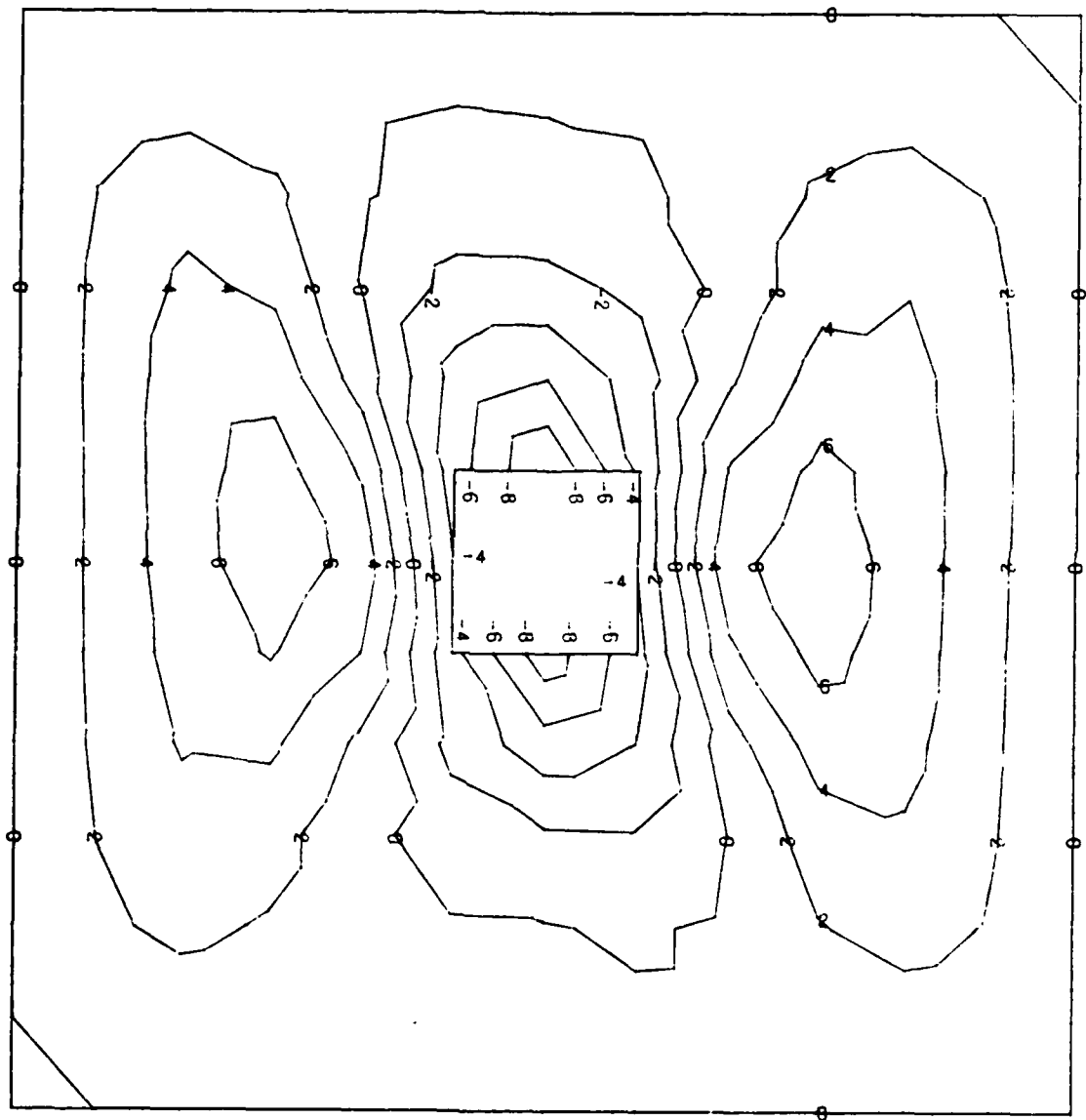


FIGURE 34: W Component Displacement Contours

Load Level 215.9 lbs/in

Maximum Displacement = .037 inch

Ply Layup $[0, +45, -45, 90]_s$

Contour Levels Are In 10^{ths} of Maximum Displacement

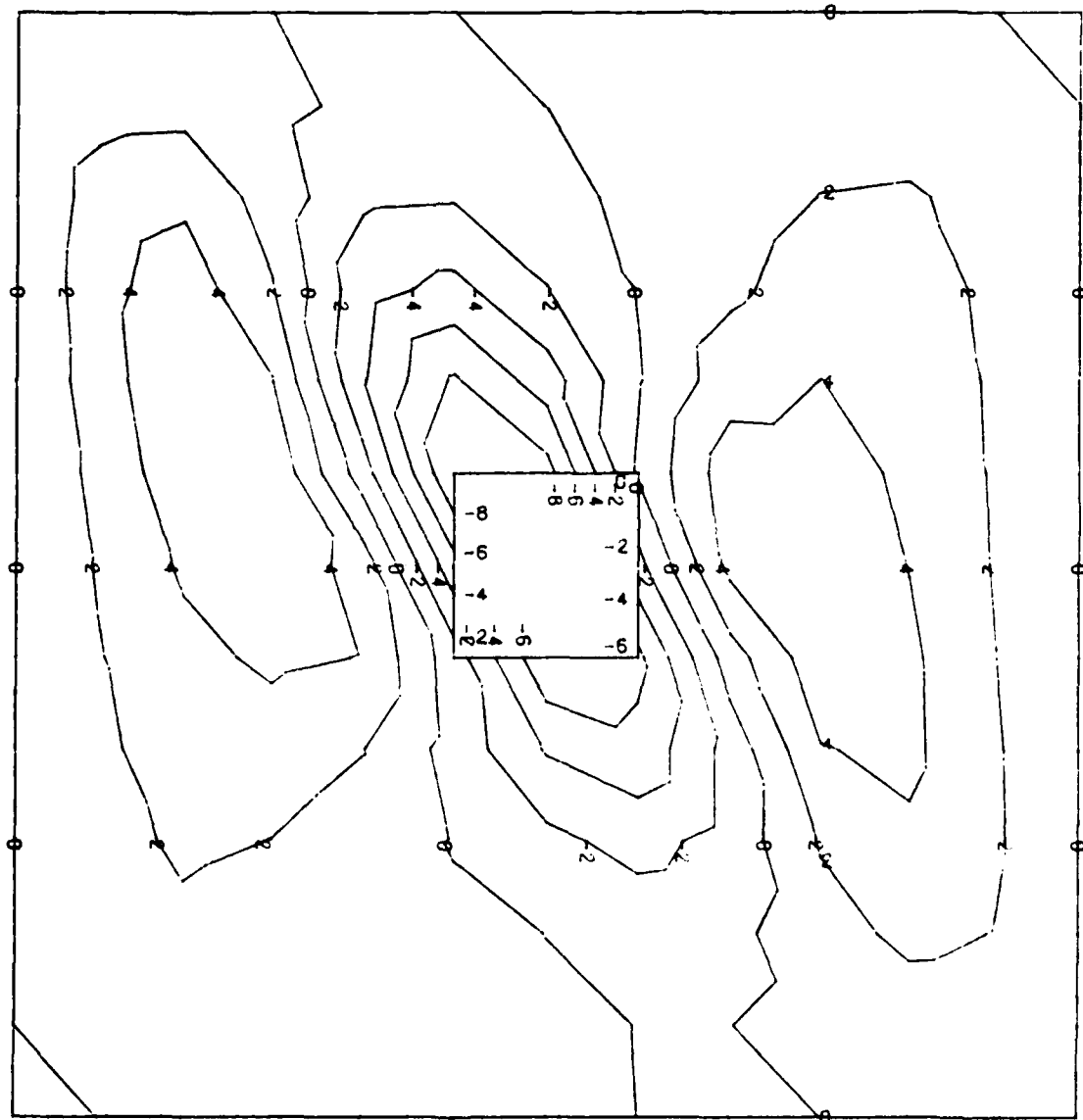


FIGURE 35: W Component Displacement Contours

Load Level 215.9 lbs/in

Maximum Displacement = .037 inch

Ply Layup $[0, -45, +45, 90]_s$

Contour Levels Are In 10^{ths} of Maximum Displacement

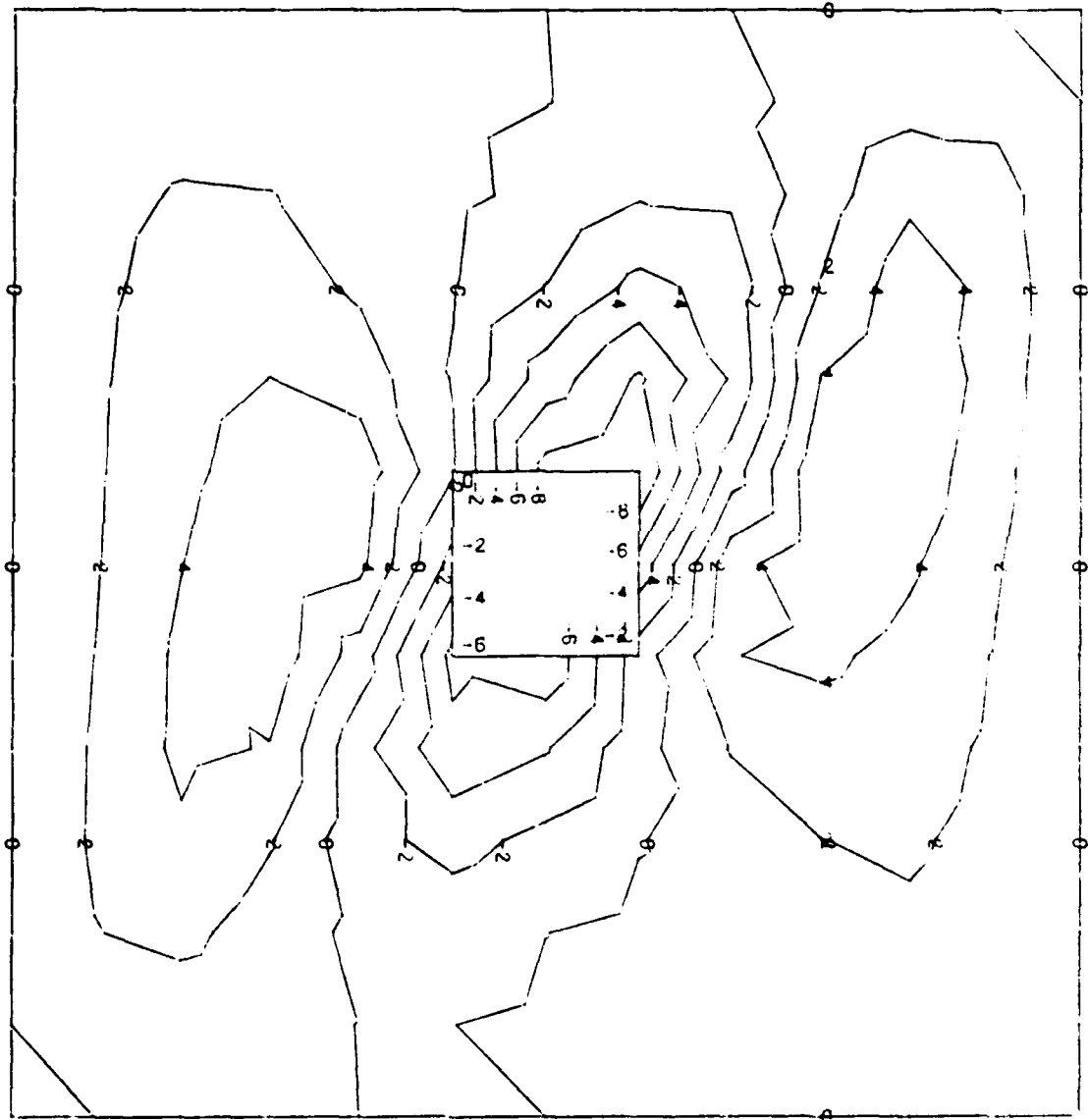


FIGURE 36: W Component Displacement Contours

Load Level 71 lbs/in

Maximum Displacement = .0040 inch

Ply Layup $[90, +45, -45, 0]_s$

Contour Levels Are In 10^{ths} of Maximum Displacement

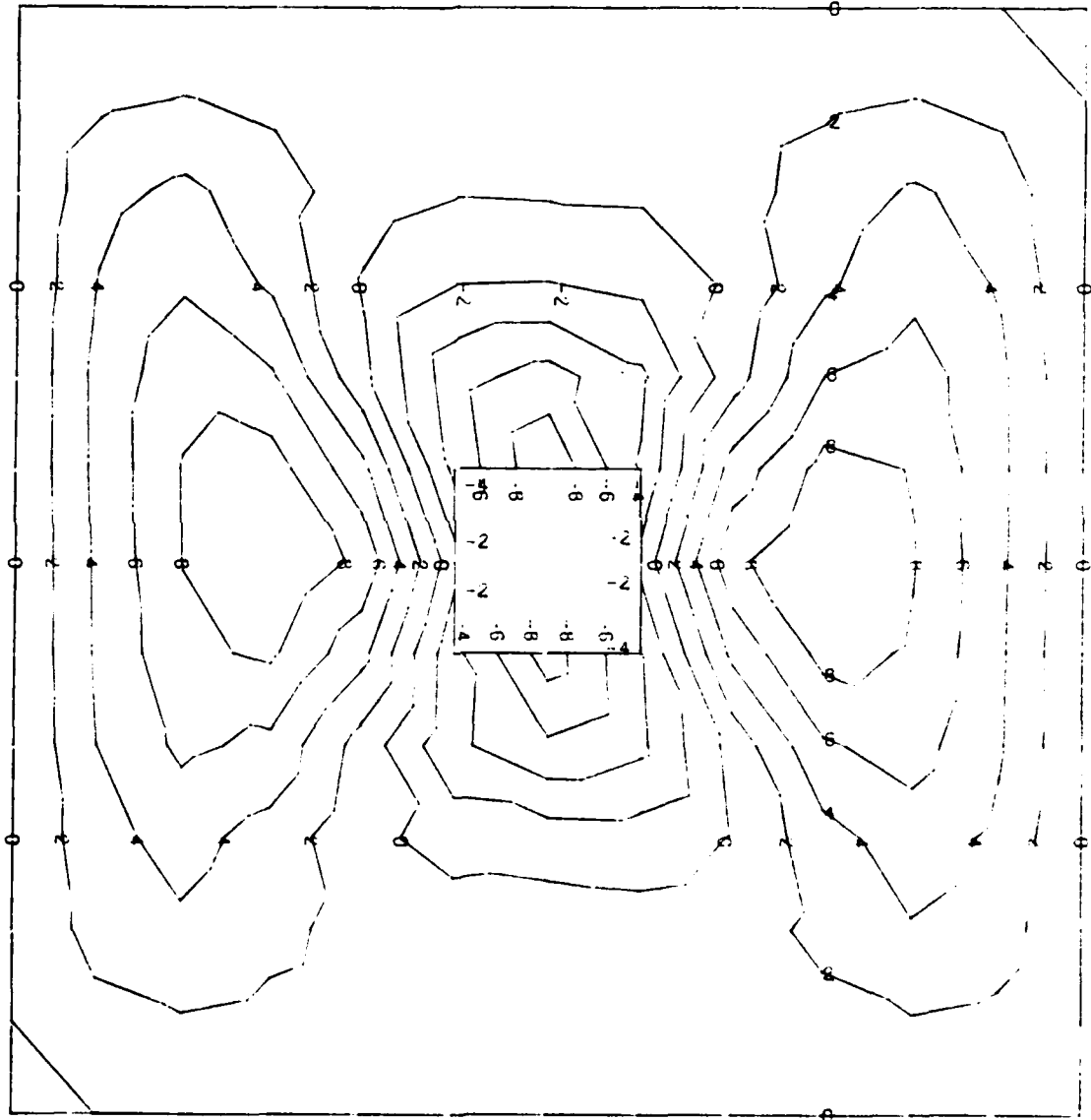


FIGURE 37: W Component Displacement Contours

Load Level 223.6 lbs/in

Maximum Displacement = .0157 inch

Ply Layup $[90, +45, -45, 0]_s$

Contour Levels Are In 10^{ths} of Maximum Displacement

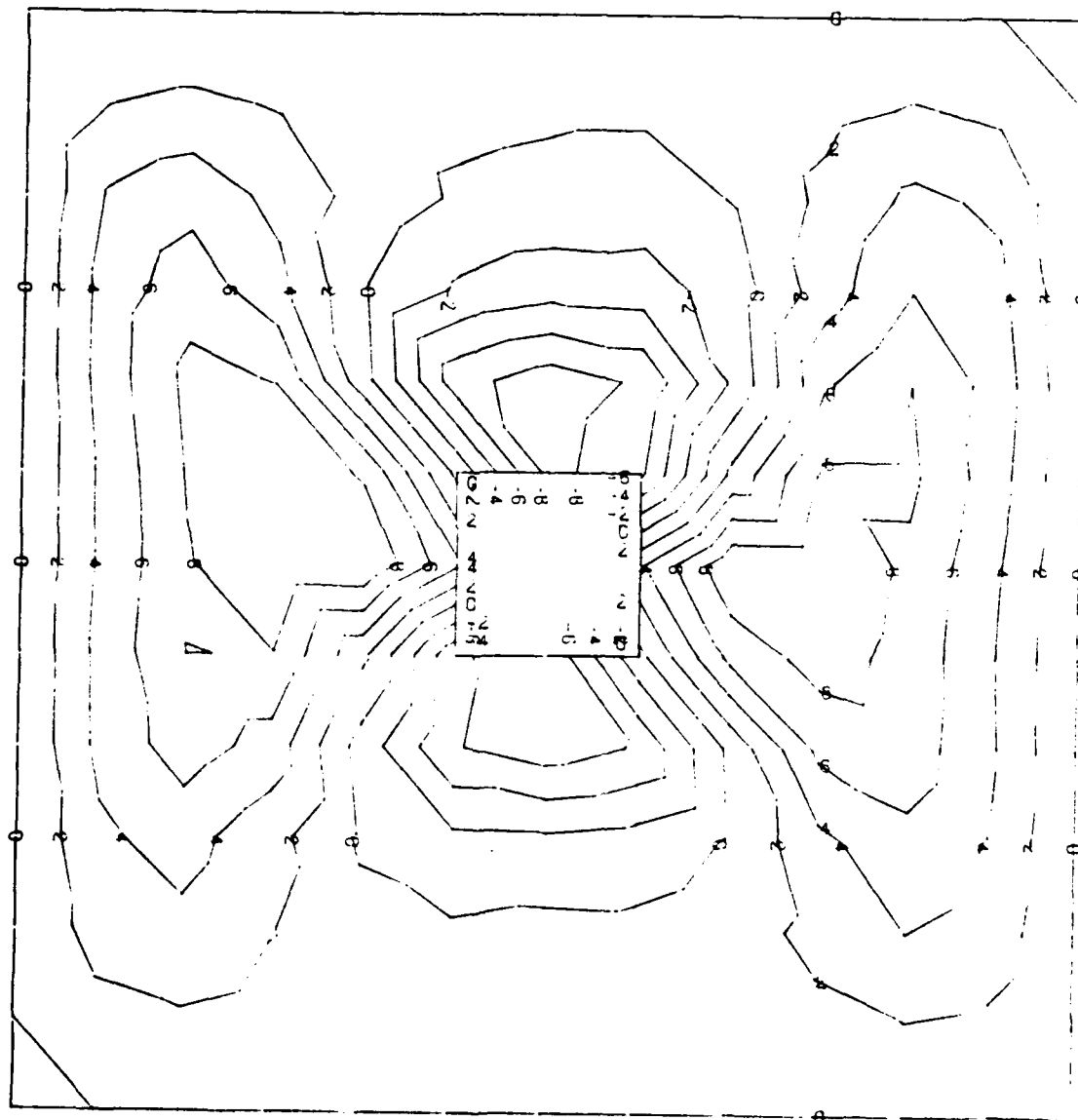


FIGURE 38: W Component Displacement Contours

Figure 34 shows that for the lower load step of 81 lbs/in for the $[0, +45, -45, 90]_s$ ply layup the displacement pattern is relatively symmetric about the center of the cutouts. This symmetry is due to the energy absorption by the axial stiffness of the panel and very little bending. The extensional (axial) stiffness matrix is symmetric in the A_{11} and A_{22} terms (See Appendix B). This pattern of symmetry is again shown in Figure 37 at 71 lbs/in for the $[90, +45, -45, 0]_s$ ply layup. This is the displacement pattern that was expected and is the same type of symmetry shown in displacement patterns of isotropic panels and shells [5, 12]. However, as the load is increased this symmetric displacement field about the center of the cutouts edges is lost when the collapse load is reached. This loss of symmetry is due to the larger radial displacements, hence the larger moments. With the greater radial displacements, the bending stiffness matrix has a greater effect. Therefore, the D_{11} and D_{22} will have an effect on the displacement pattern. Since there is a large difference between them, the symmetry in the displacement field is lost.

Figure 35 shows the radial displacement contour of the $[0, +45, -45, 90]_s$ panel at the collapse load of 215.3 lbs/in. One will notice that there is a trough of large radial inward displacements from the upper left corner of the cutout to the lower right. Figure 36 represents the displacement contours for the $[0, -45, +45, 90]_s$ panel and

is almost the mirror image of Figure 35. Both of these panels have the same collapse load and maximum radial displacements. Figure 38 (considering a $[90, +45, -45, 0]_s$ panel) on the other hand does not show as great a change from the symmetric displacement pattern as the two previous panels did. This stands to reason since the D_{22} term in the $[90, +45, -45, 0]_s$ panel is larger than the corresponding value in the $[0, +45, -45, 90]_s$ panel. The larger D_{22} term will absorb the same energy with less bending involved. With the smaller bending, the displacement pattern will be more symmetric. One will notice however, that also in Figure 38 there is still a trough or radial inward displacements that run from just right of center of the top edge of the cutout to slightly left of center of the bottom edge of the cutout. These displacement troughs and loss of symmetry are better shown on radial displacement profiles for different load levels across the panel at several distances from the top of the panel.

The $[0, -45, +45, 90]_s$ panel with a 2 inch by 2 inch cutout was selected to show this. Figures 39 through 44 are the plots of the radial displacement versus load level for a specific circumferential arc across the panel at different locations from the top of the panel. Figure 39 is the plot for 2 inches from the top of the panel at load levels 56 lbs/in, 106 lbs/in, 156 lbs/in, and 215.9 lbs/in. Likewise, Figures 40 through 44 are for the same load levels at the distance from the top of the panel is indicated on each figure.

[0, -45, +45, 90]

Radial Displacement 2 inches from Top of Panel

Load Levels Increase Away From Horizontal Axis

Load Levels (lbs/in) are 56, 106, 156, 215.9

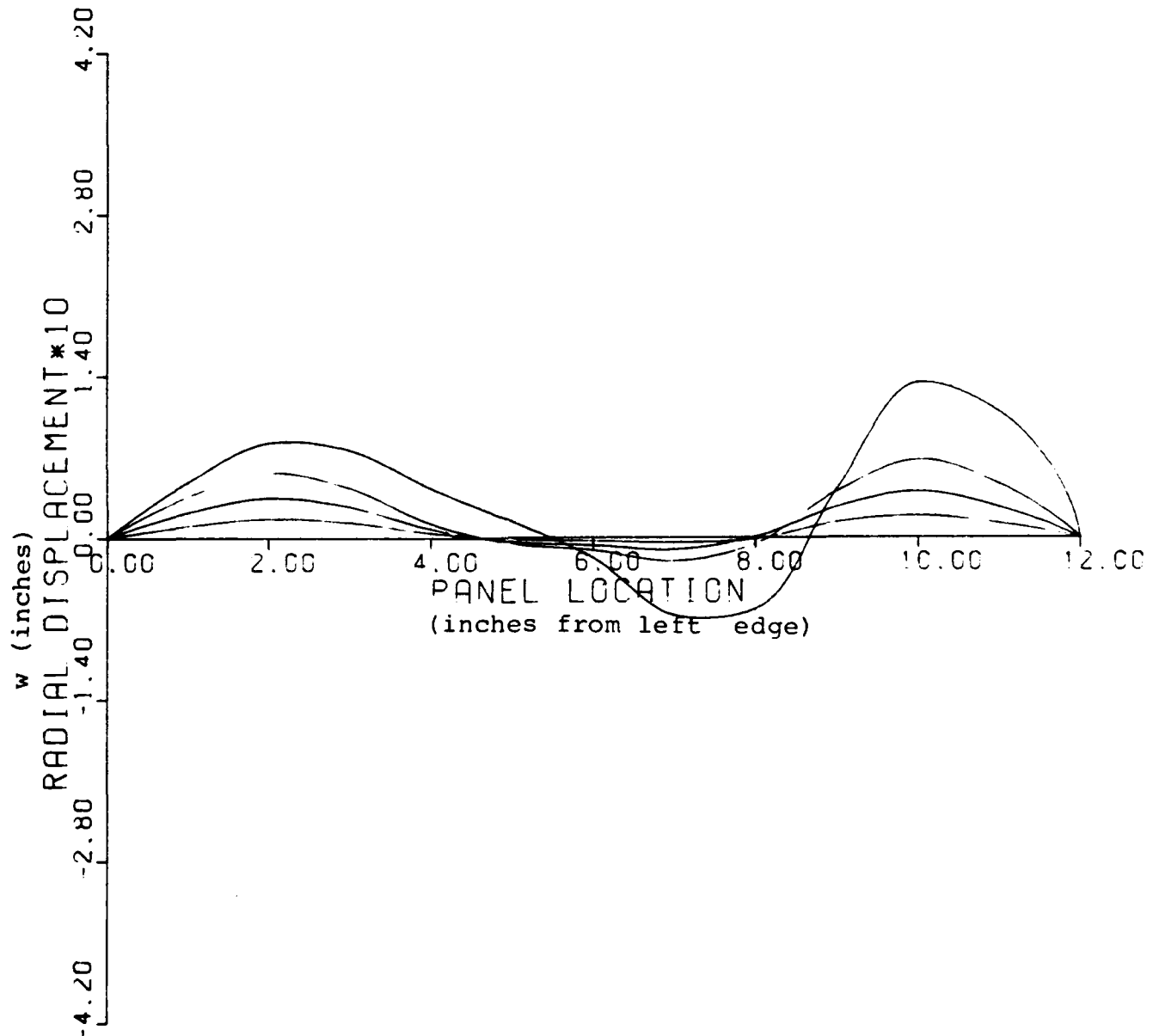


FIGURE 39: Radial Displacement Profiles

$[0, -45, +45, 90]_S$

Radial Displacement 3 inches from Top of Panel

Load Levels Increase Away From Horizontal Axis

Load Levels (lbs/in) are 56, 106, 156, 215.9

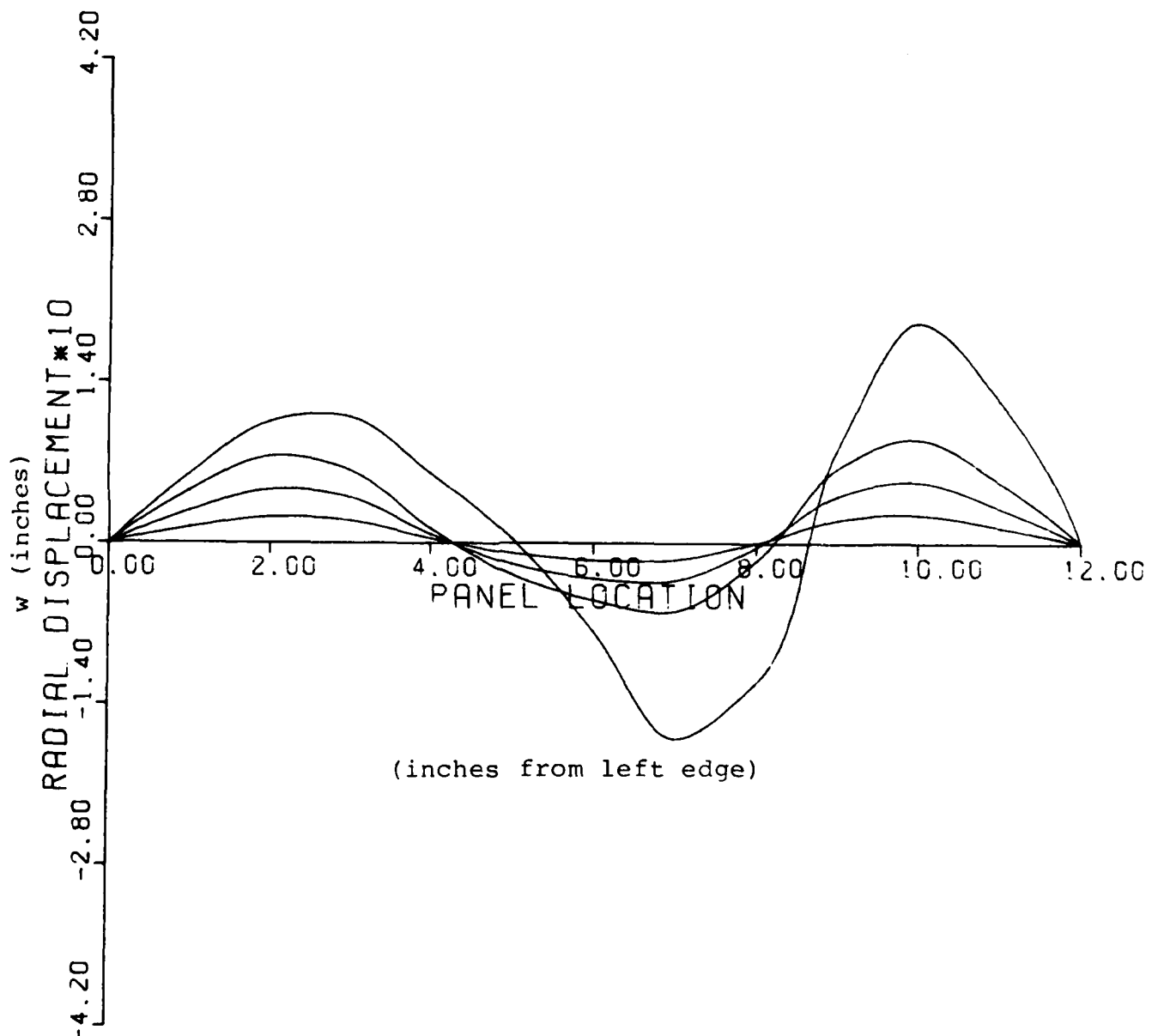


FIGURE 40: Radial Displacement Profiles

$[0, -45, +45, 90]_s$

Radial Displacement 5 inches from Top of Panel (Top of Cutout)

Load Levels Increase Away From Horizontal Axis

Load Levels (lbs/in) are 56, 106, 156, 215.9

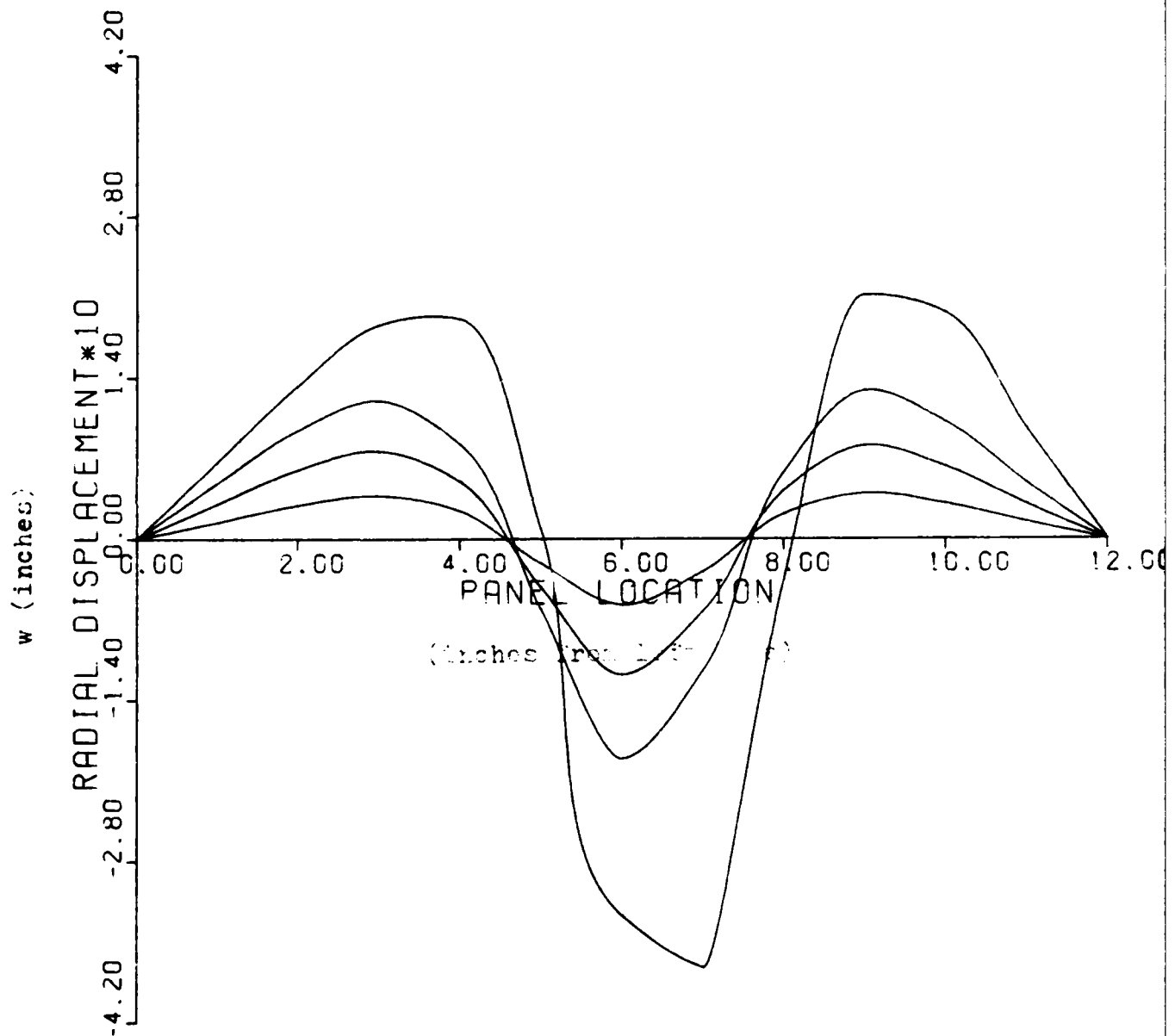


FIGURE 41: Radial Displacement Profiles

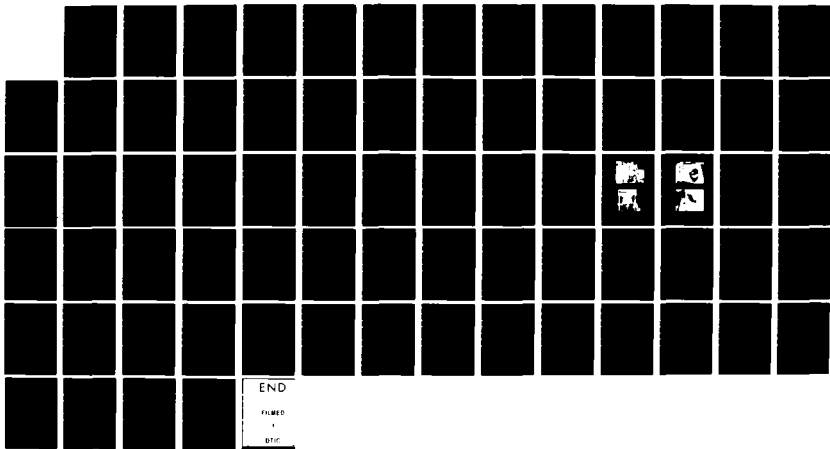
AD-A124 739

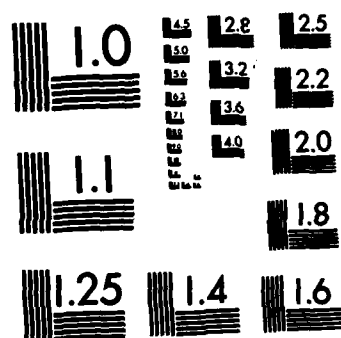
A PARAMETRIC STUDY OF SURFACE IMPERFECTIONS AND SMALL
CUTOUTS IN A COMPOSITE PANEL(U) AIR FORCE INST OF TECH
WRIGHT-PATTERSON AFB OH SCHOOL OF ENGI... T C JANISSE
DEC 82 AFIT/GRE/AA/82D-15 . F/G 12/1

2/2

UNCLASSIFIED

NL





MICROCOPY RESOLUTION TEST CHART
NATIONAL BUREAU OF STANDARDS-1963-A

$[0, -45, +45, 90]_s$

Radial Displacement 6 inches from Top of Panel
(Across Center of Cutout)

Load Levels Increase Away From Horizontal Axis

Load Levels (lbs/in) are 56, 106, 156, 215.9

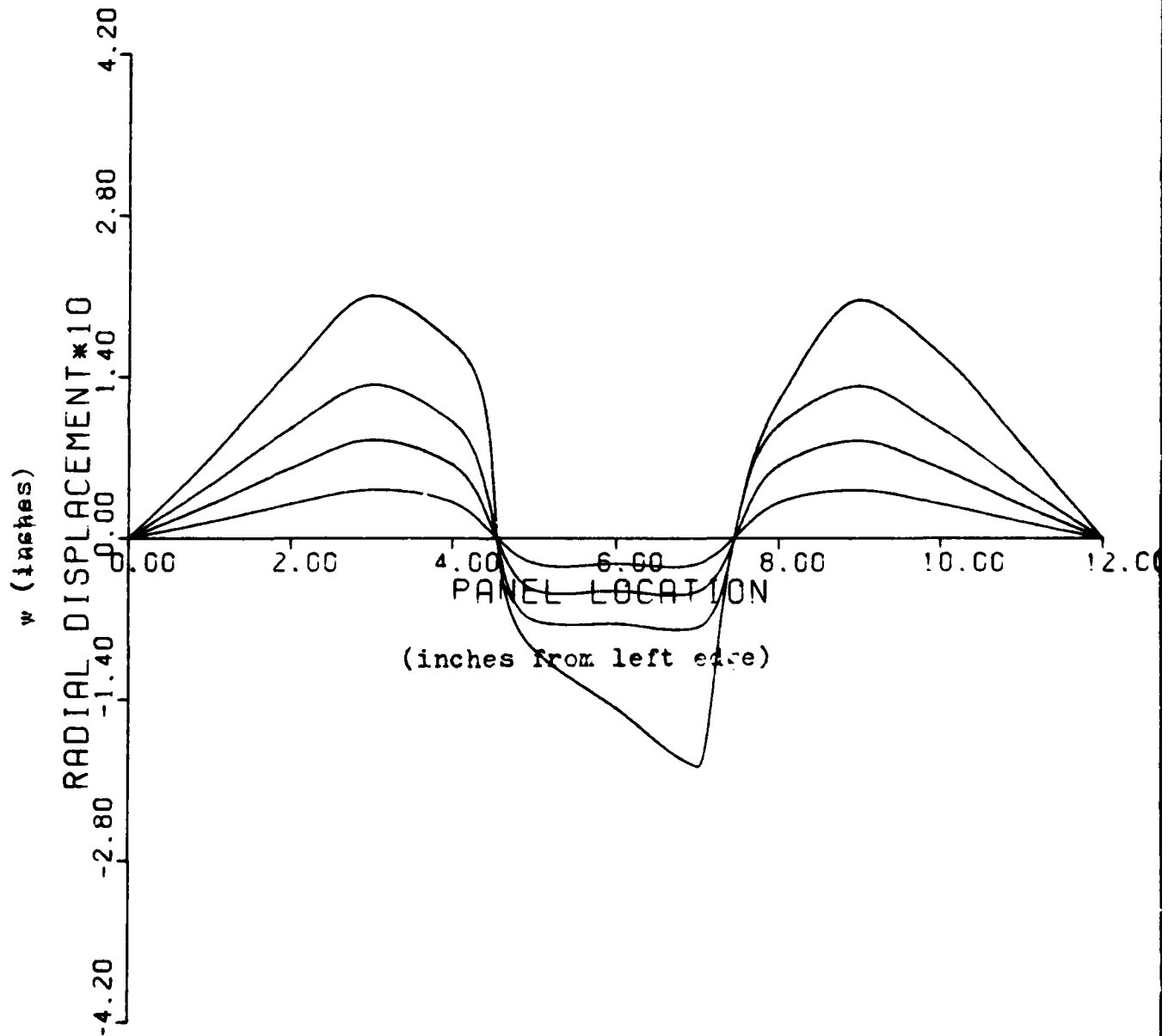


FIGURE 42: Radial Displacement Profiles

$[0, -45, +45, 90]_s$

Radial Displacement 7 inches from Top of Panel
(Bottom of Cutout)

Load Levels Increase Away From Horizontal Axis

Load Levels (lbs/in) are 56, 106, 156, 215.9

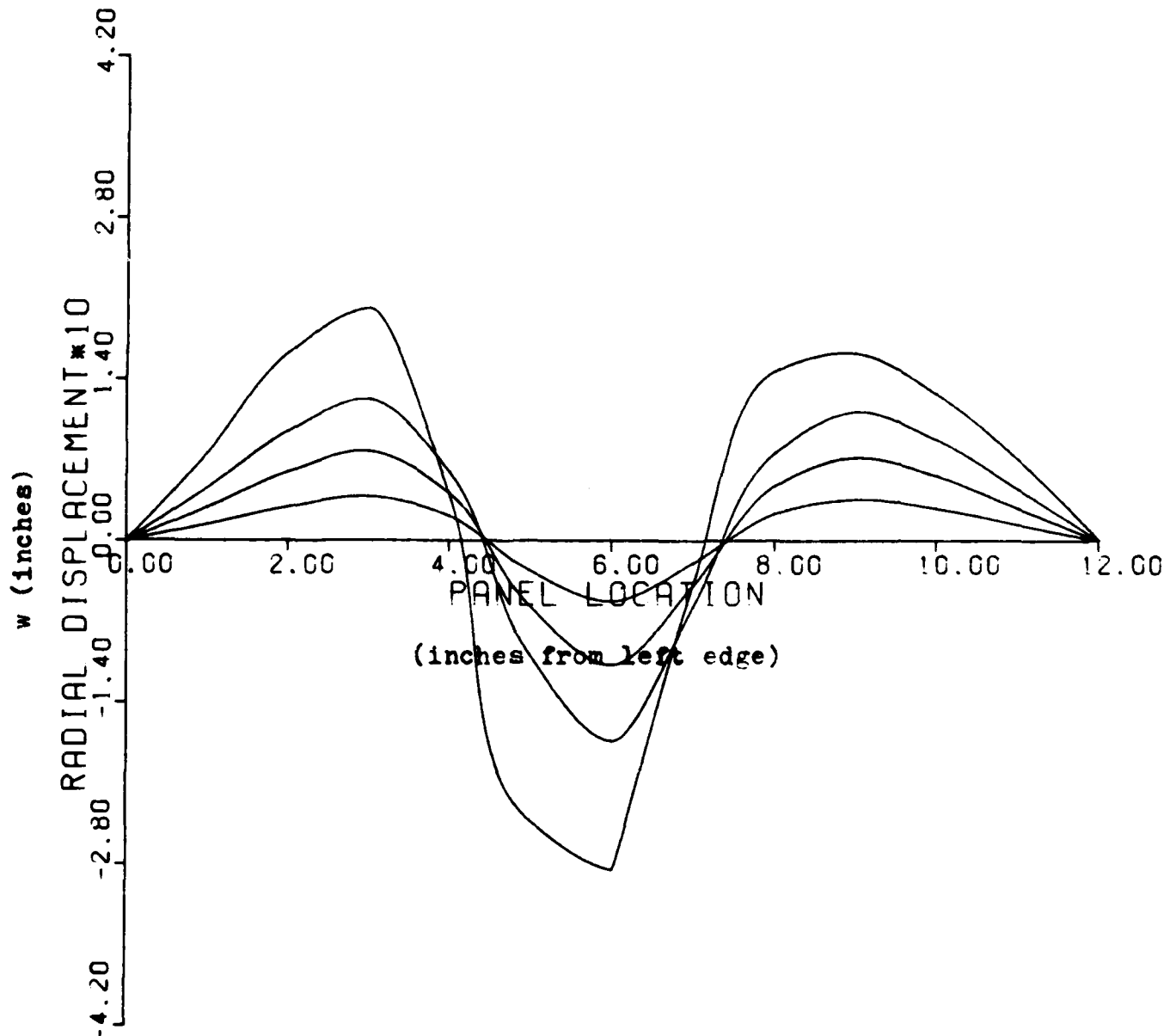


FIGURE 43: Radial Displacement Profiles

$[0, -45, +45, 90]_s$

Radial Displacement 10 inches from Top of Panel

Load Levels Increase Away From Horizontal Axis

Load Levels (lbs/in) are 56, 106, 156, 215.9

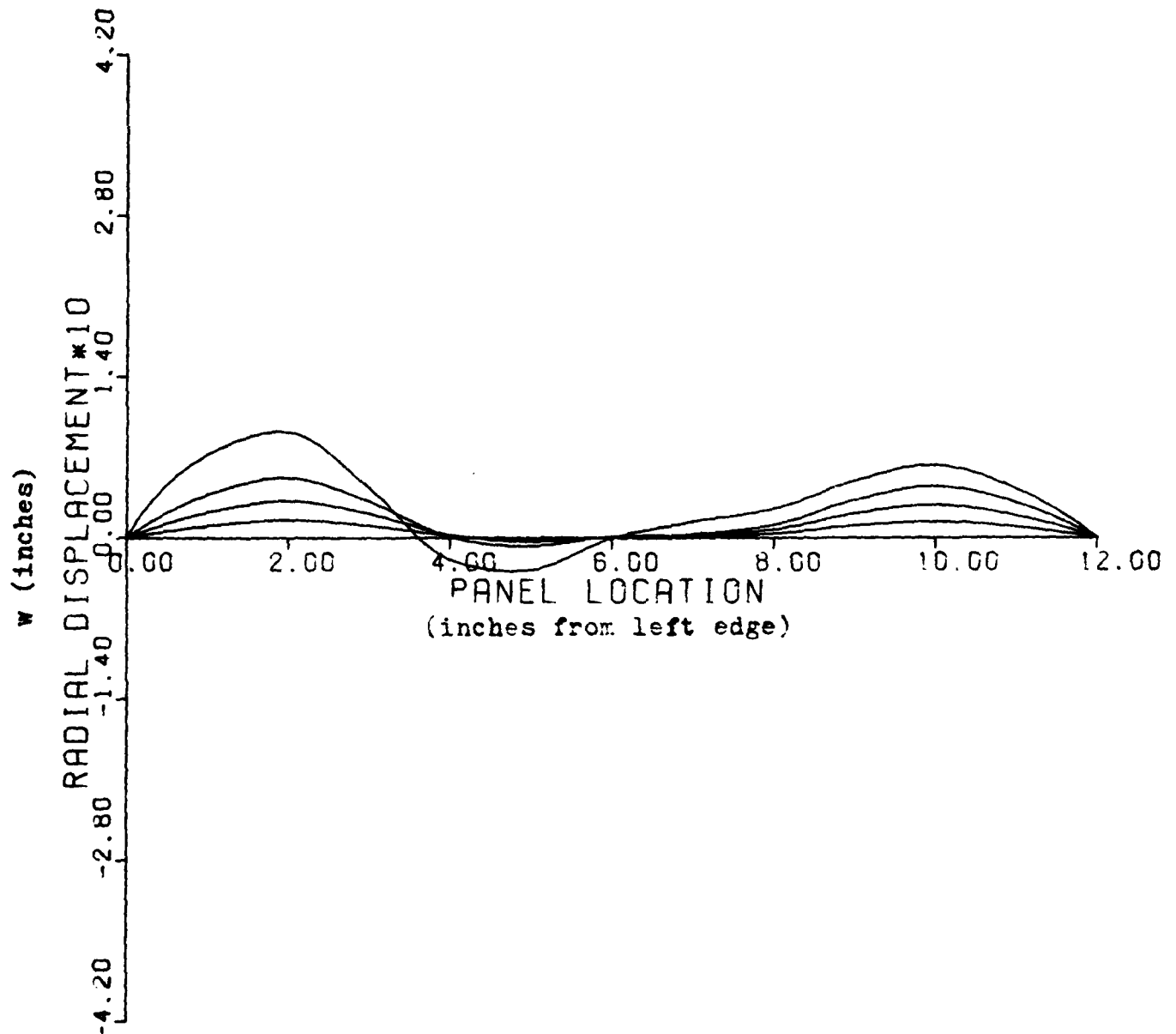


FIGURE 44: Radial Displacement Profiles

One can see in viewing the figures that the panel's radial displacements are relatively symmetric as the load increases about the center of the panel for the first 3 load levels. At the final load level (collapse load level) one can see the loss of symmetry and the trough of layer displacements that run from the upper right of the panel to the lower left is easily seen. The other panels that were analyzed displayed the same type of displacement profiles as the panel's load increased as the small cutout panel had. In the comparison of the radial displacements for the nonlinear analysis of the cutouts it was noticed, and mentioned earlier, that the $[0, +45, -45, 90]_s$ panel had a trough of displacements that were about twice as deep as the $[90, +45, -45, 0]_s$ panel did even though they had the same top edge displacement and almost the same collapse load. This is because of the difference in the D_{22} term in the bending stiffness. In light of this, the moment resultant profiles for these two panels were studied.

Like the displacement profiles, the same four load levels were selected to show the resultant moment profiles across the panel and down the panel. Figure 45 through 52 are the resultant moment profiles for the $[0, +45, -45, 90]_s$ panel with the small cutout and figures 53 through 60 are the moment resultant profiles for the $[90, +45, -45, 0]_s$ panel with a small cutout. In viewing Figures 45 through 60, one can see that the moment resultants are relatively symmetric about the center of the panel for the first 3 load levels.

$[0, +45, -45, 90]_s$

M_x 2.5 Inches From Top of Panel

Load Levels Increase Away From Horizontal Axis

Load Levels (lbs/in) are 56, 106, 156, 215.9

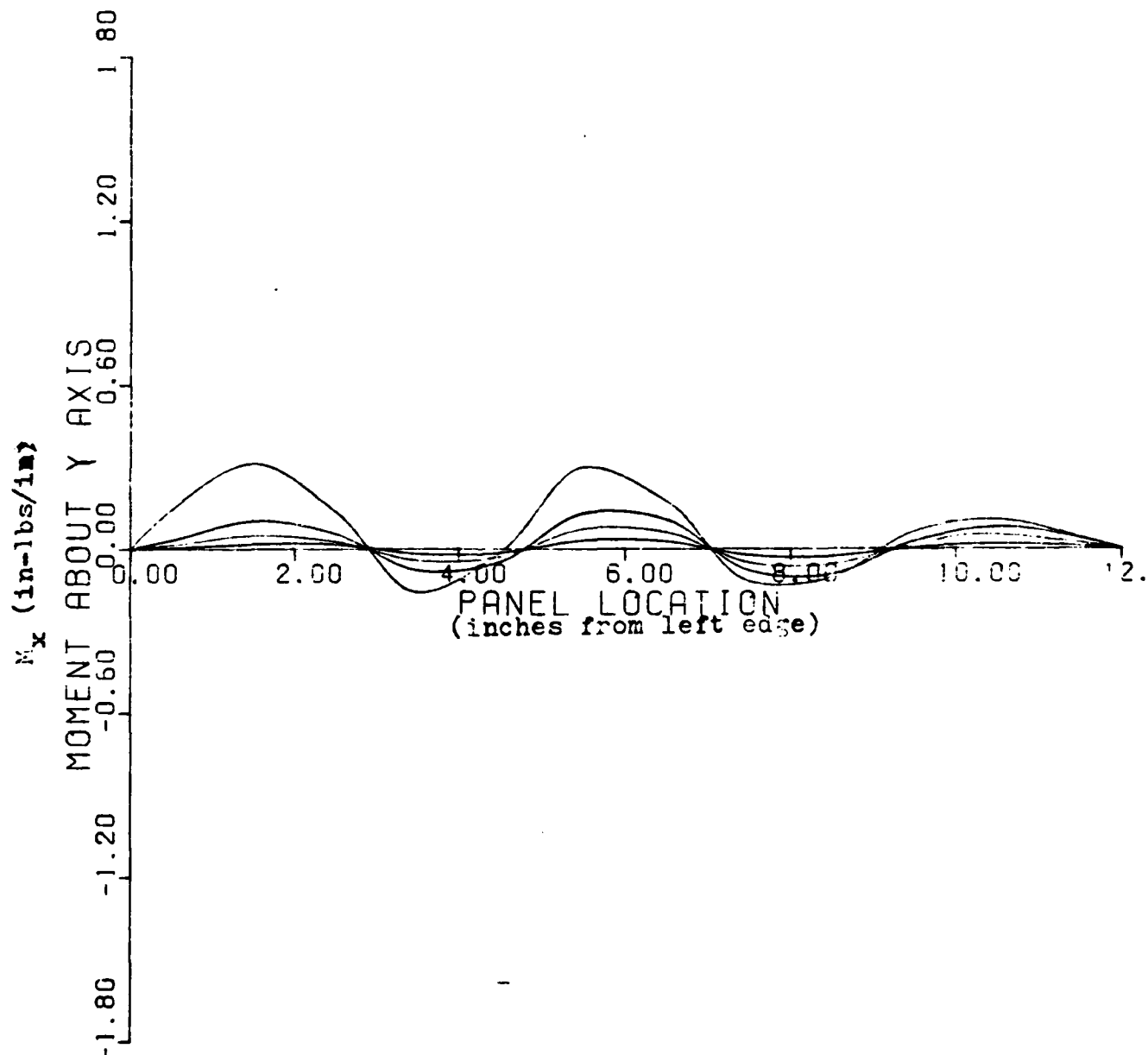


FIGURE 45: Moment Resultant Profiles

$[0, +45, -45, 90]_s$

M_x 4.5 Inches From Top of Panel

Load Levels Increase Away From Horizontal Axis

Load Levels (lbs/in) are 56, 106, 156, 215.9

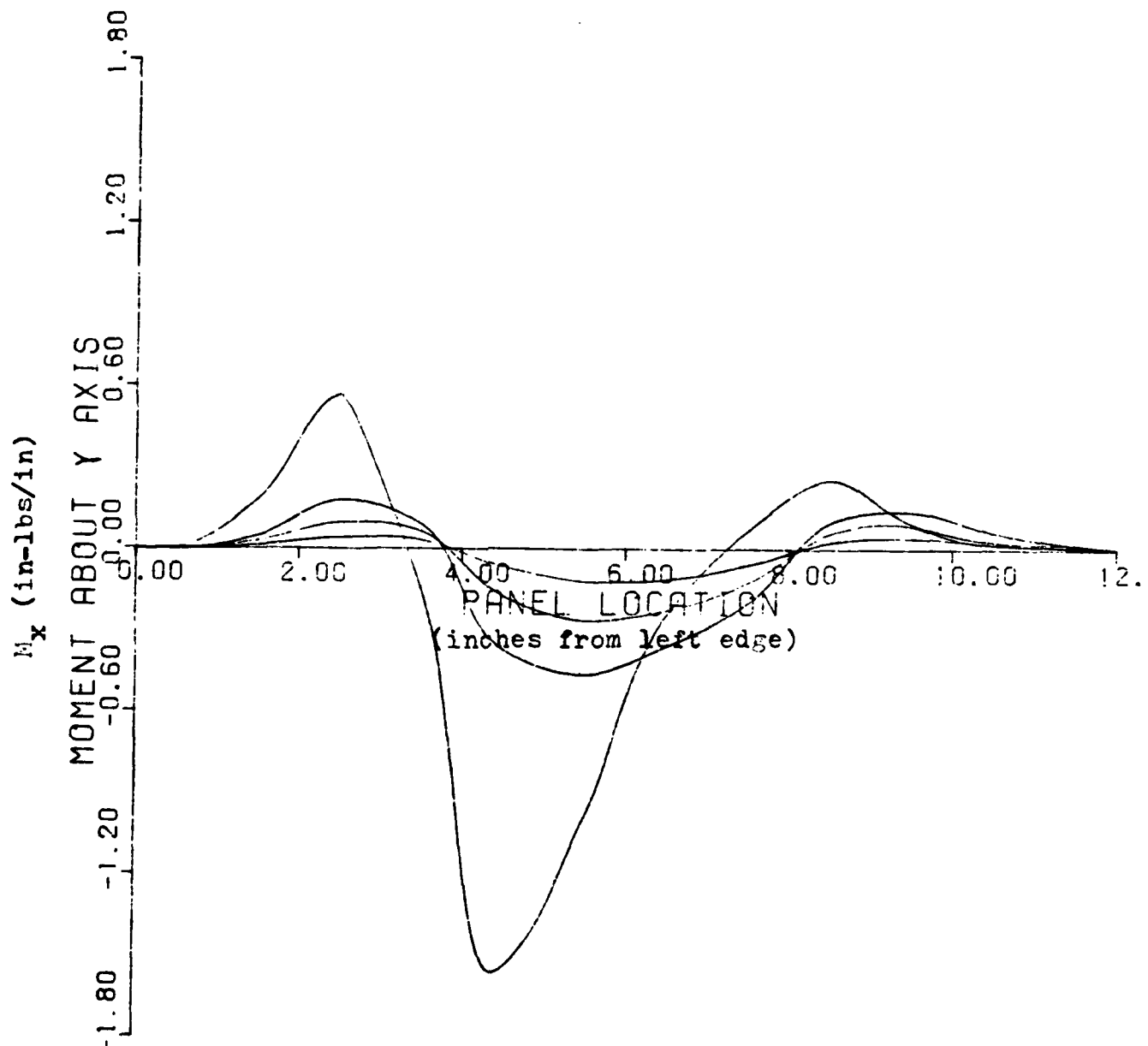


FIGURE 46: Moment Resultant Profiles

$[0, +45, -45, 90]_s$

M_x 7.5 Inches From Top of Panel

Load Levels Increase Away From Horizontal Axis

Load Levels (lbs/in) are 56, 106, 156, 215.9

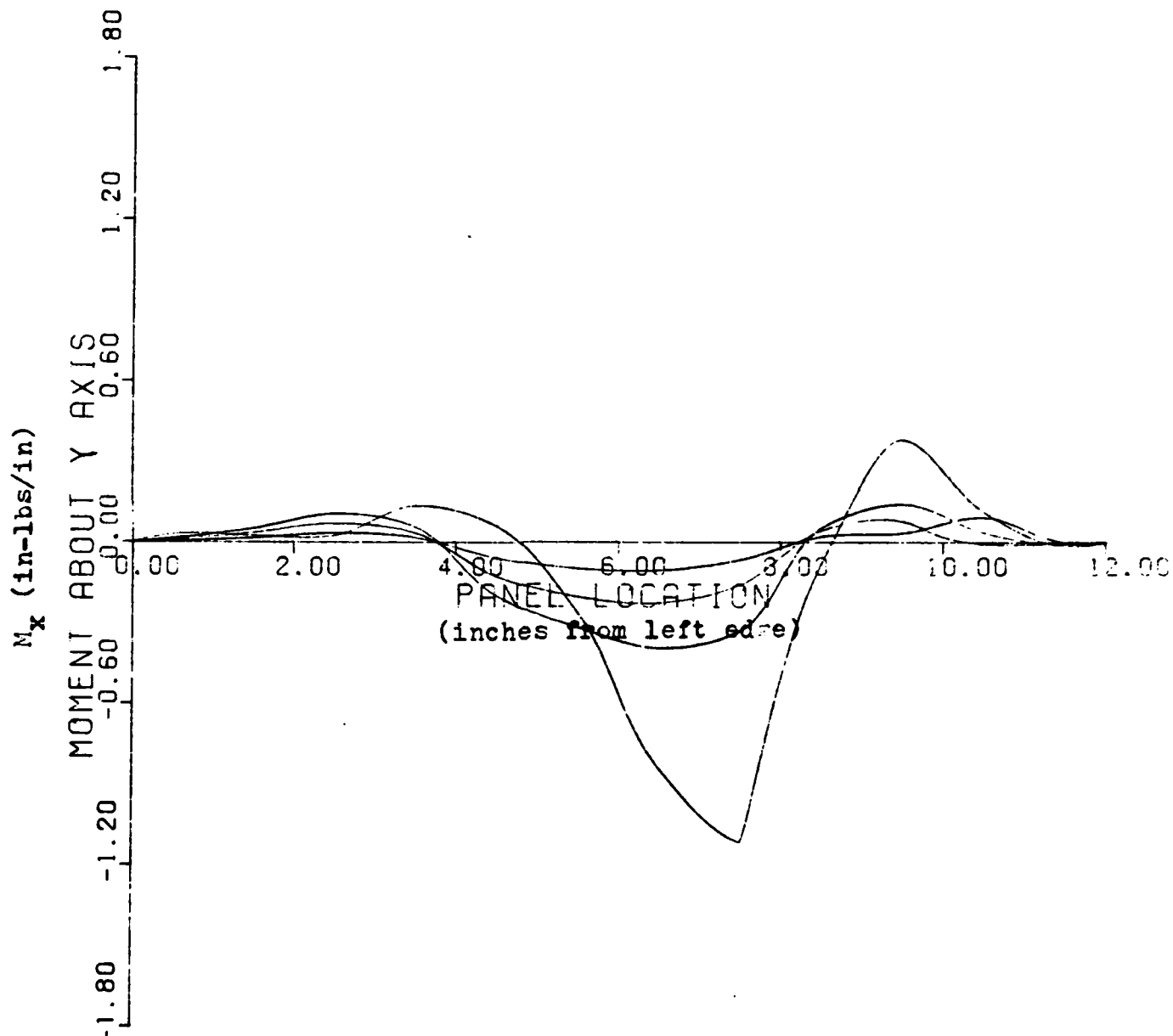


FIGURE 47: Moment Resultant Profiles

$[0, +45, -45, 90]_s$

M_x 9.5 Inches From Top of Panel

Load Levels Increase Away From Horizontal Axis

Load Levels (lbs/in) are 56, 106, 156, 215.9

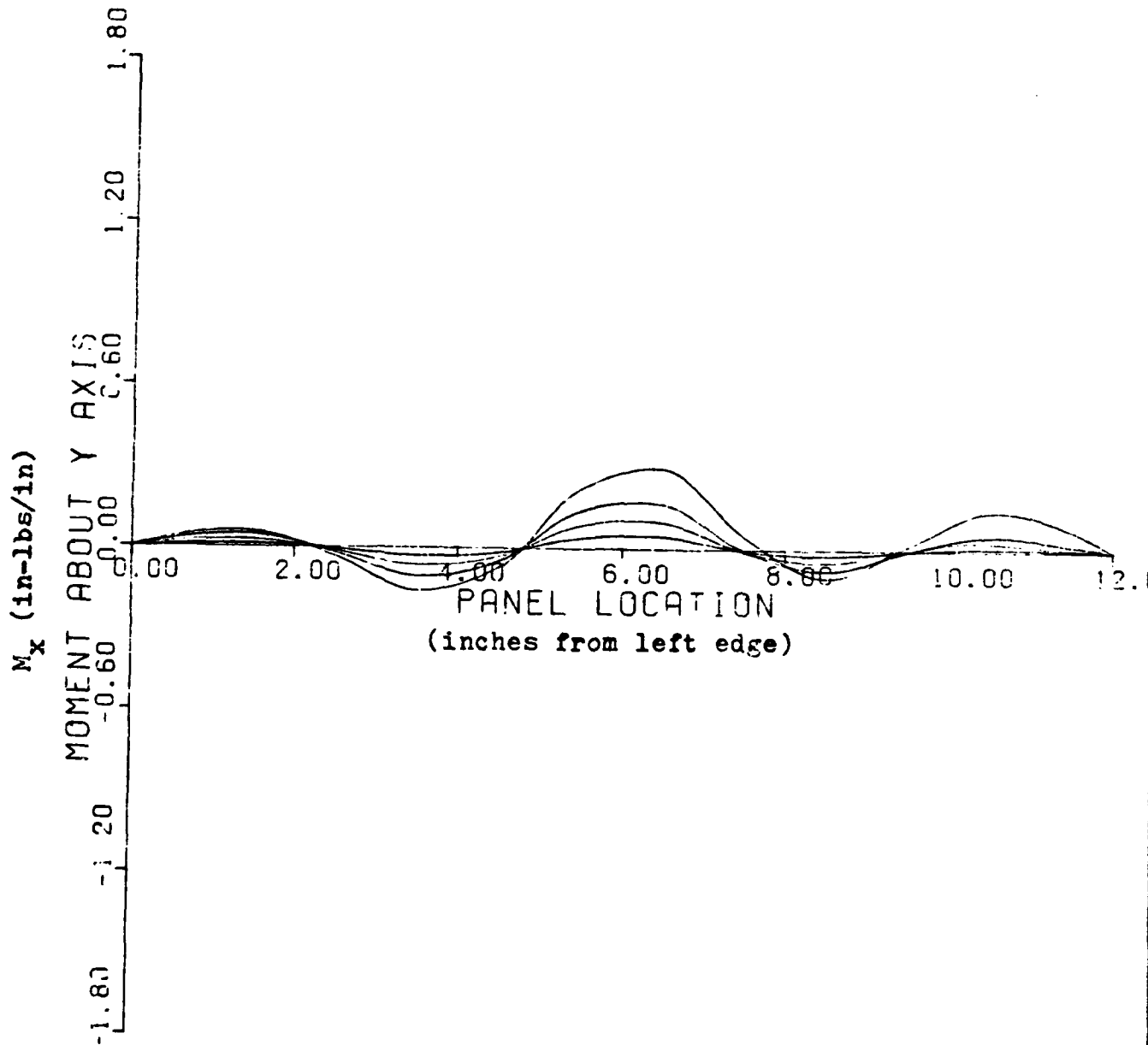


FIGURE 48: Moment Resultant Profiles

$[0, +45, -45, 90]_s$

M_y 2.5 Inches From Left Edge of Panel

Load Levels Increase Away From Horizontal Axis

Load Levels (lbs/in) are 56, 106, 156, 215.9

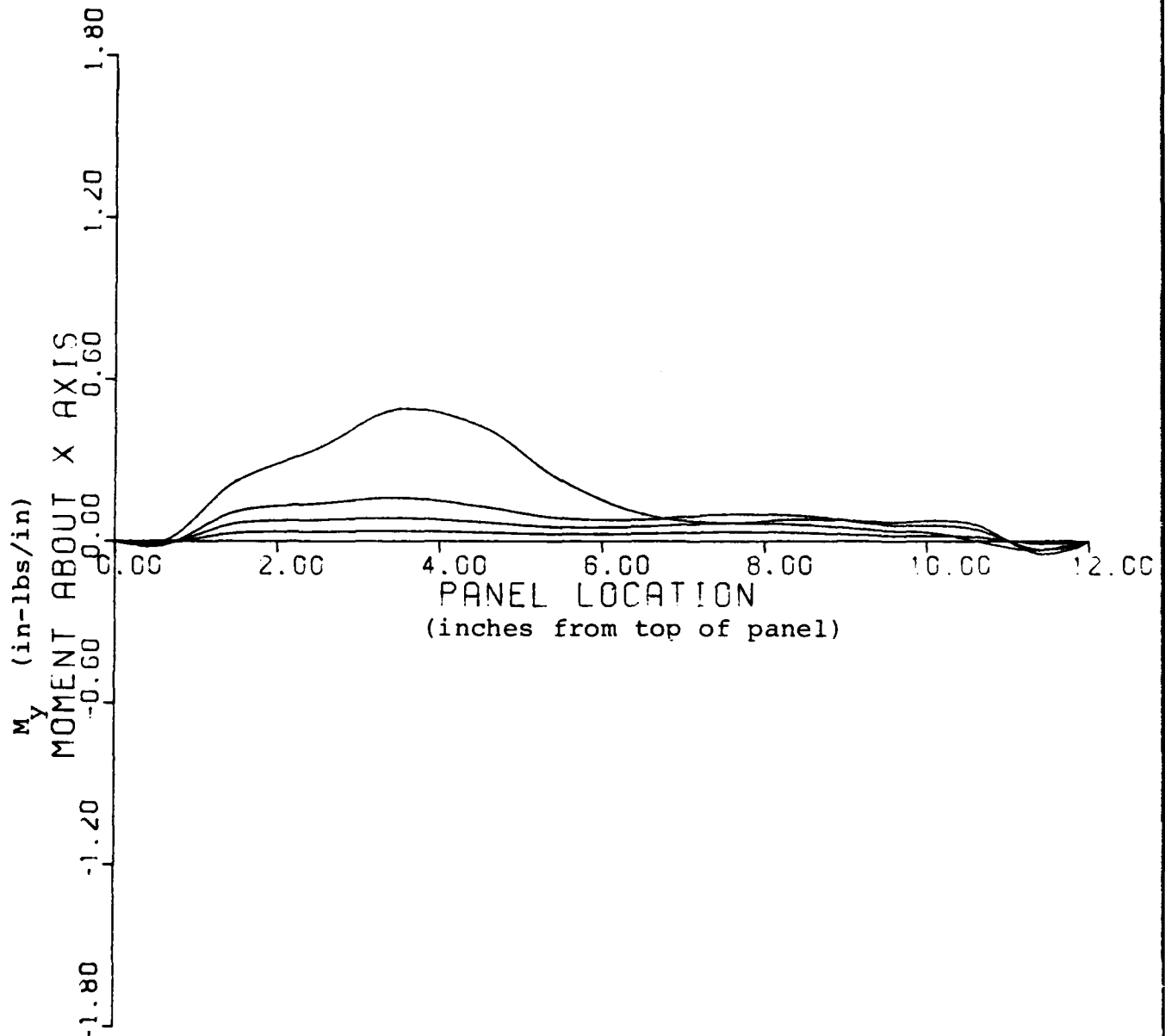


FIGURE 49: Moment Resultant Profiles

$[0, +45, -45, 90]_s$

M_y 4.5 Inches From Left Edge of Panel

Load Levels Increase Away From Horizontal Axis

Load Levels (lbs/in) are 56, 106, 156, 215.9

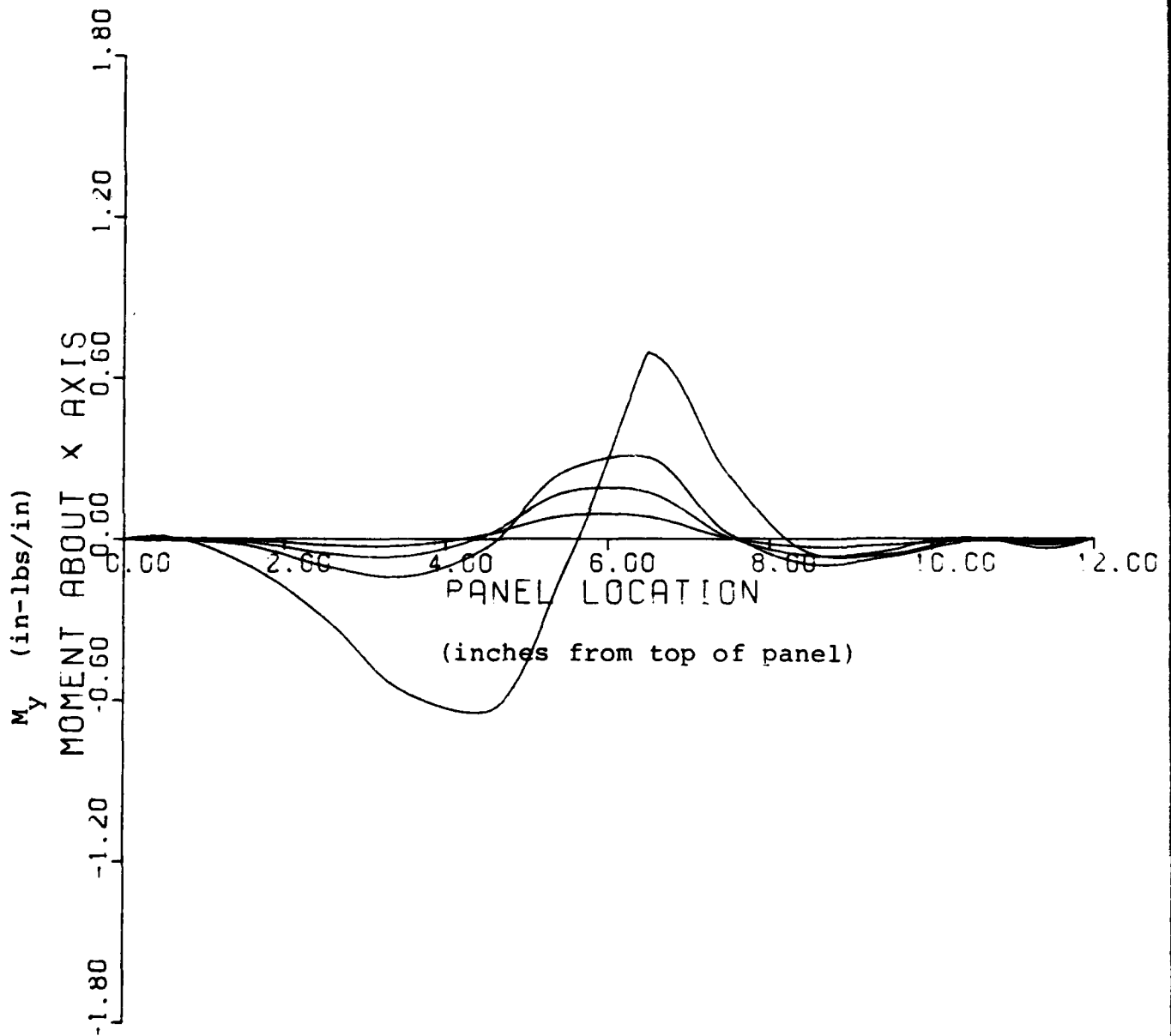


FIGURE 50: Moment Resultant Profiles

$[0, +45, -45, 90]_s$

M_y 7.5 Inches From Left Edge of Panel

Load Levels Increase Away From Horizontal Axis

Load Levels (lbs/in) are 56, 106, 156, 215.9

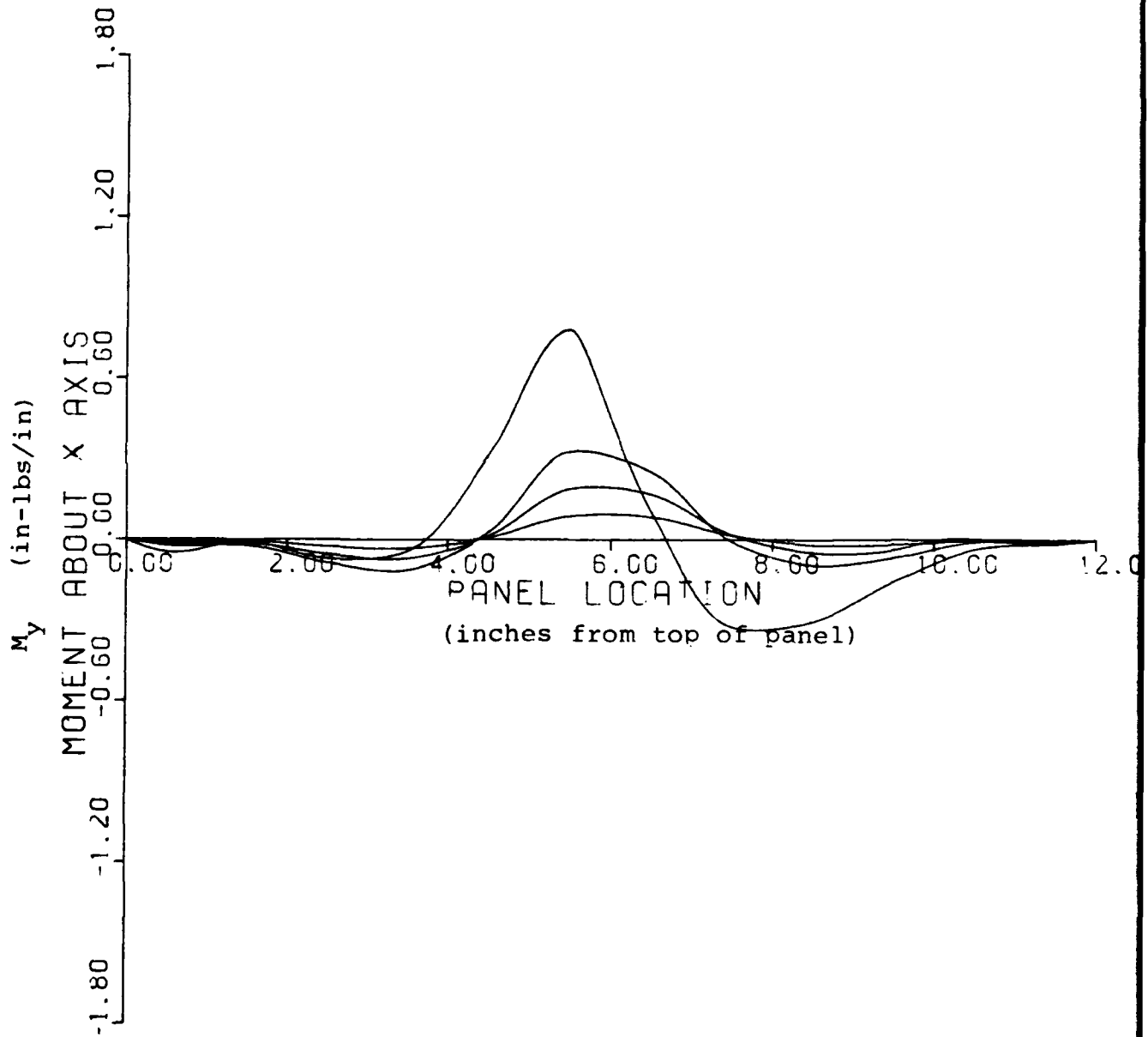


FIGURE 51: Moment Resultant Profiles

$[0, +45, -45, 90]_s$

M_y 9.5 Inches From Left Edge of Panel

Load Levels Increase Away From Horizontal Axis

Load Levels (lbs/in) are 56, 106, 156, 215.9

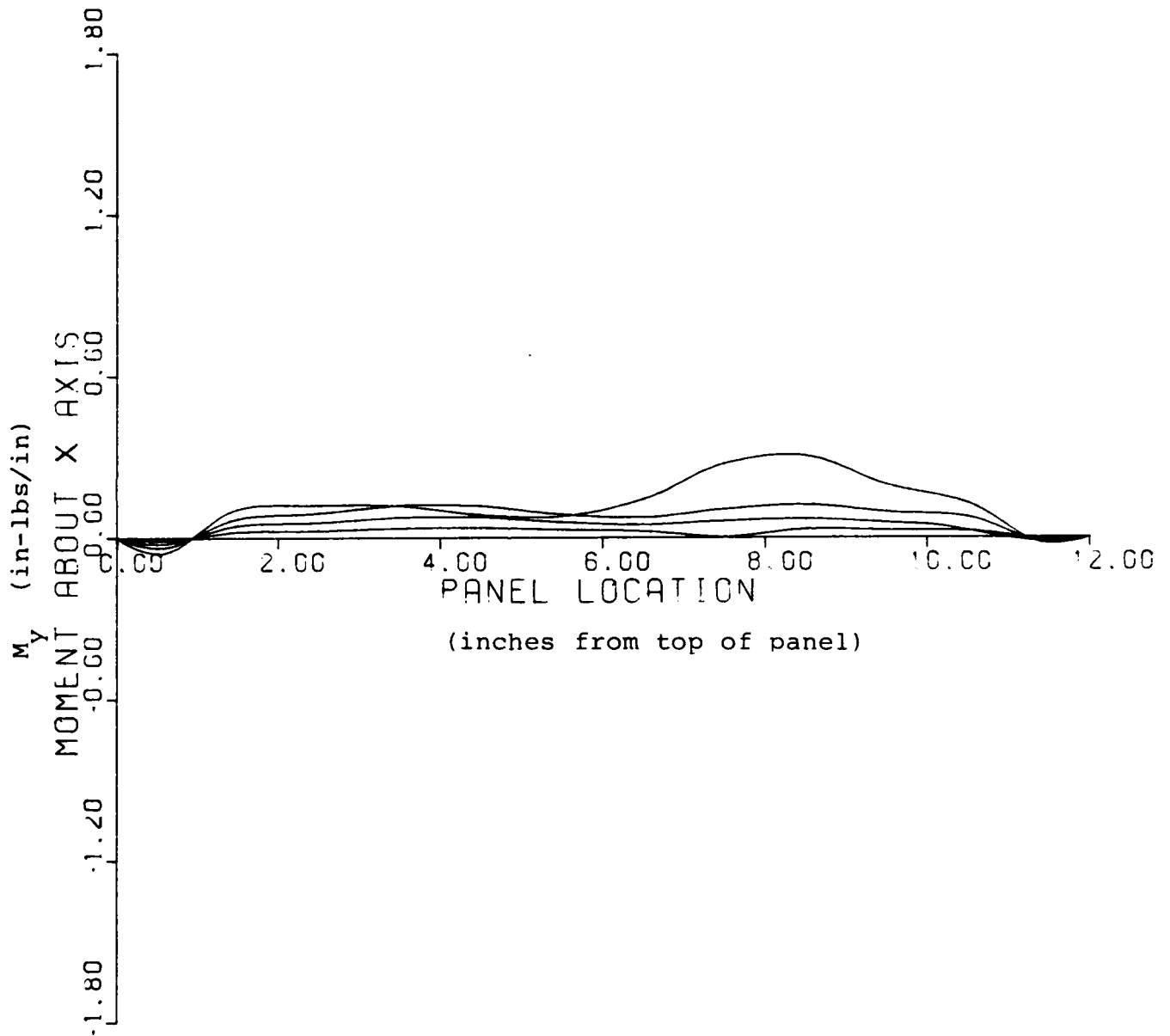


FIGURE 52: Moment Resultant Profiles

$[90, +45, -45, 0]_s$

M_x 2.5 Inches From Top of Panel

Load Levels Increase Away From Horizontal Axis

Load Levels (lbs/in) are 56, 106, 156, 215.9

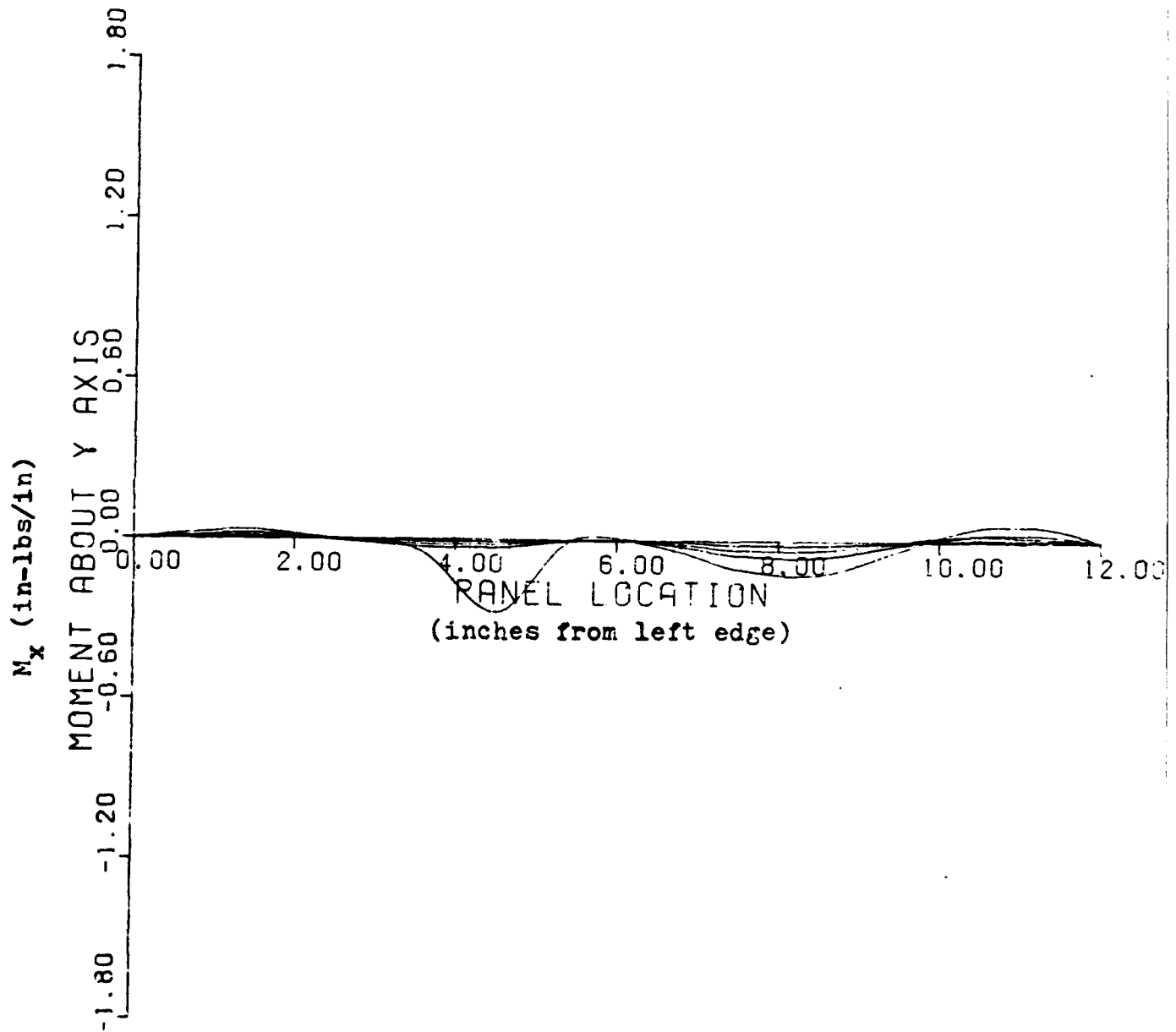


FIGURE 53: Moment Resultant Profiles

$[90, +45, -45, 0]_s$

M_x 4.5 Inches From Top of Panel

Load Levels Increase Away From Horizontal Axis

Load Levels (lbs/in) are 56, 106, 156, 215.9

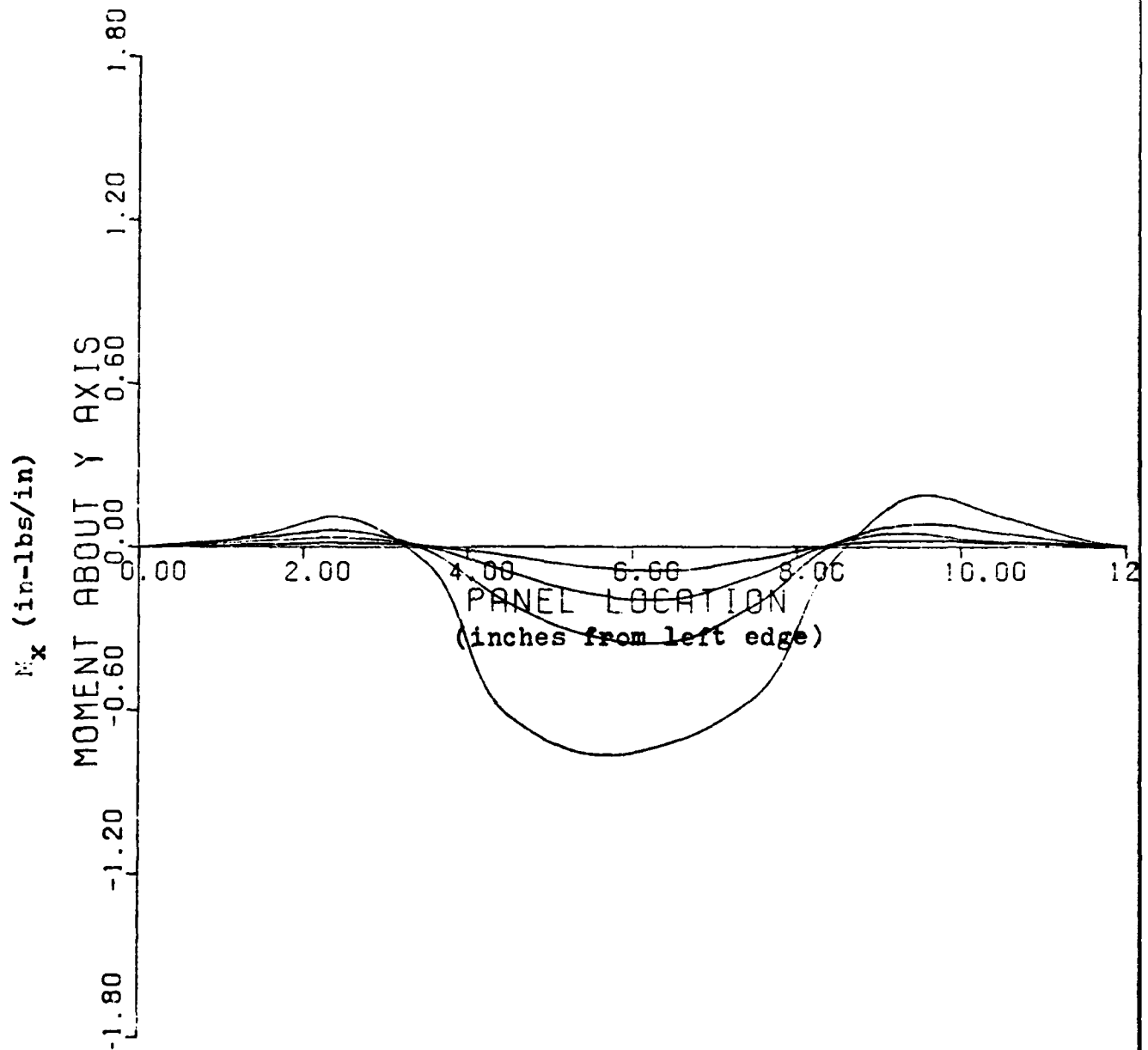


FIGURE 54: Moment Resultant Profiles

$[90, +45, -45, 0]_s$

M_x 7.5 Inches From Top of Panel

Load Levels Increase Away From Horizontal Axis

Load Levels (lbs/in) are 56, 106, 156, 215.9

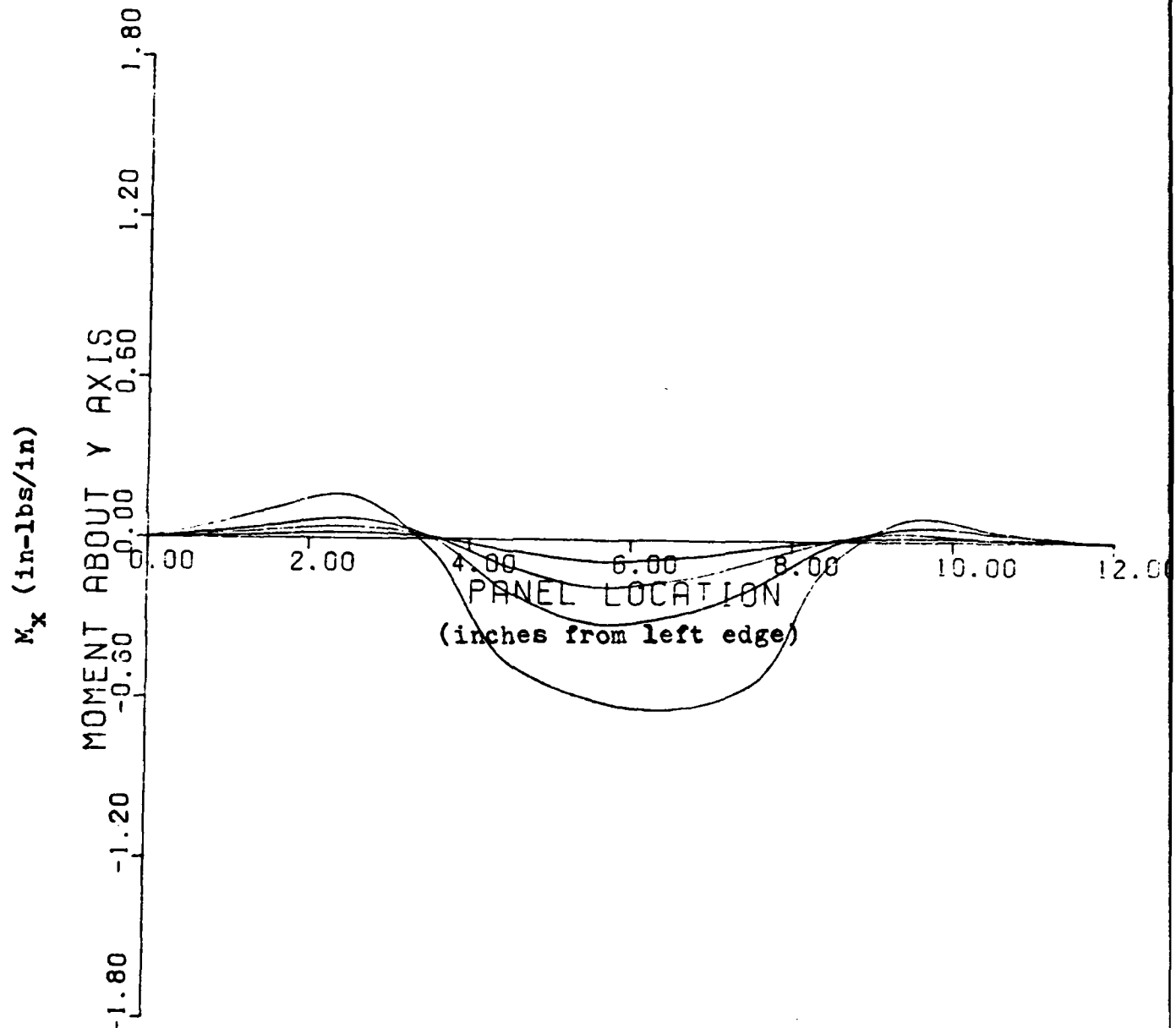


FIGURE 55: Moment Resultant Profiles

$[90, +45, -45, 0]_s$

M_x 9.5 Inches From Top of Panel

Load Levels Increase Away From Horizontal Axis

Load Levels (lbs/in) are 56, 106, 156, 215.9

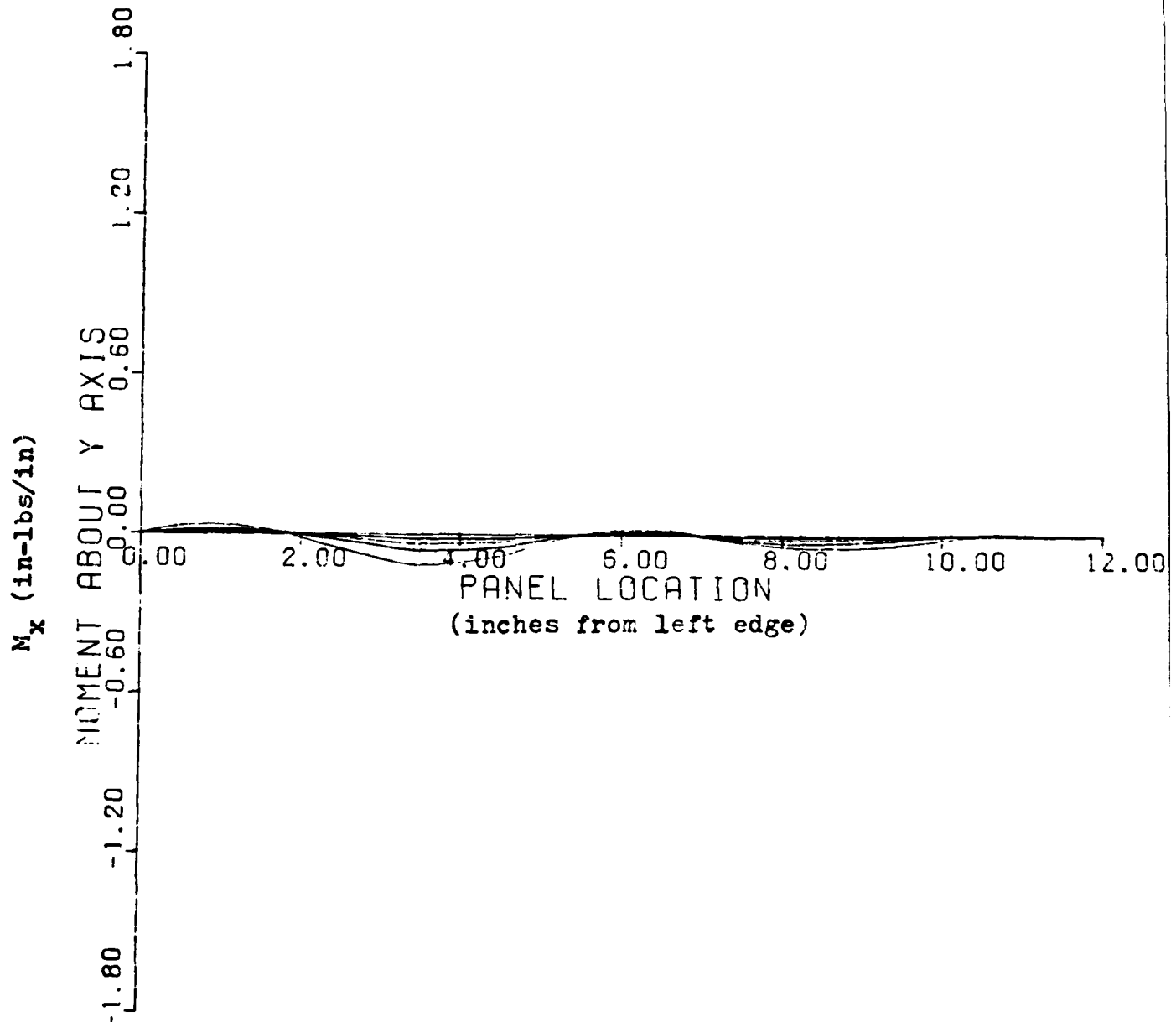


FIGURE 56: Moment Resultant Profiles

$[90, +45, -45, 0]_s$

M_y 2.5 Inches From Left edge of Panel

Load Levels Increase Away From Horizontal Axis

Load Levels (lbs/in) are 56, 106, 156, 215.9

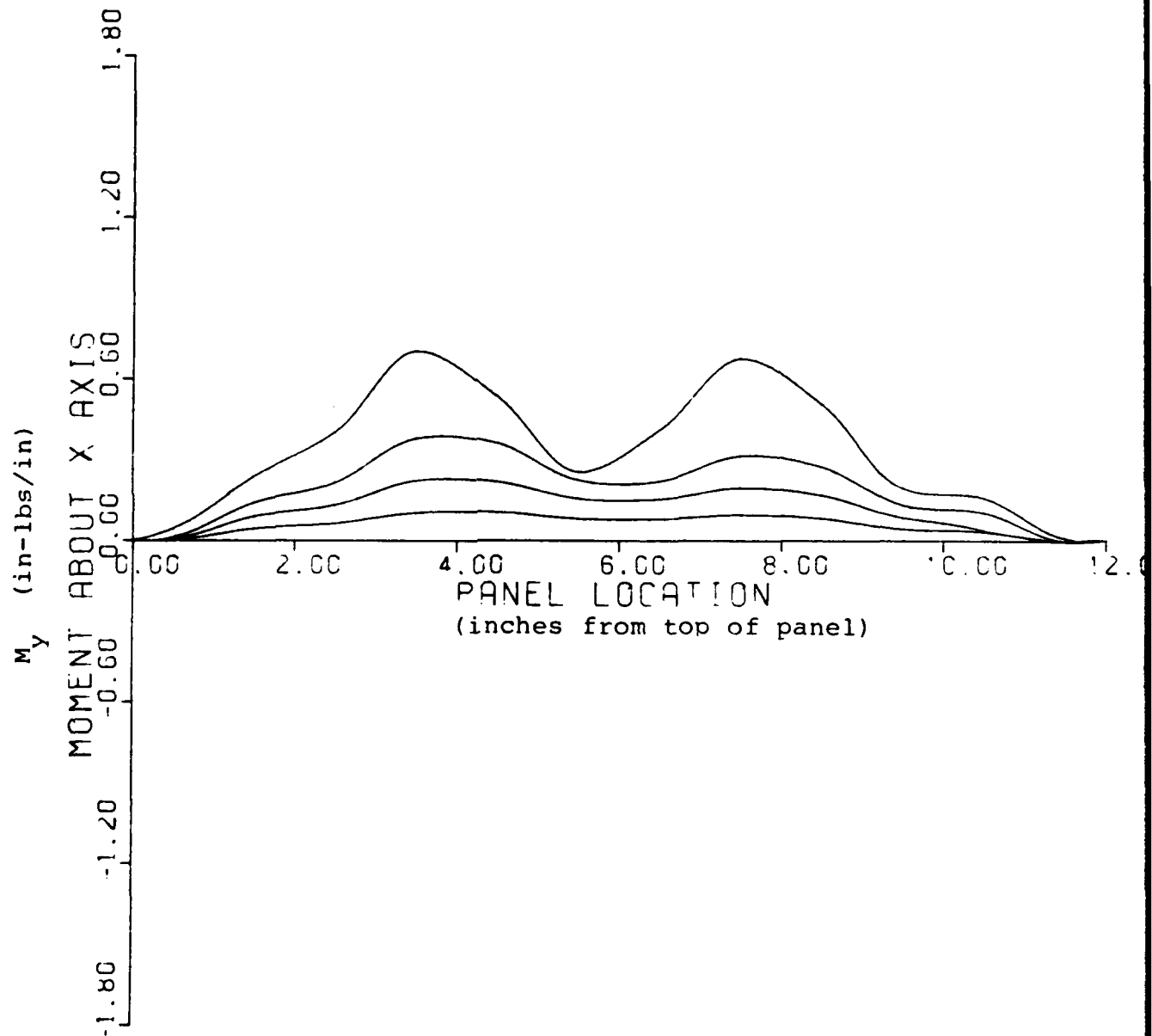


FIGURE 57: Moment Resultant Profiles

[90, +45, -45, 0]_s

M_y 4.5 Inches From Left edge of Panel

Load Levels Increase Away From Horizontal Axis

Load Levels (lbs/in) are 56, 106, 156, 215.9

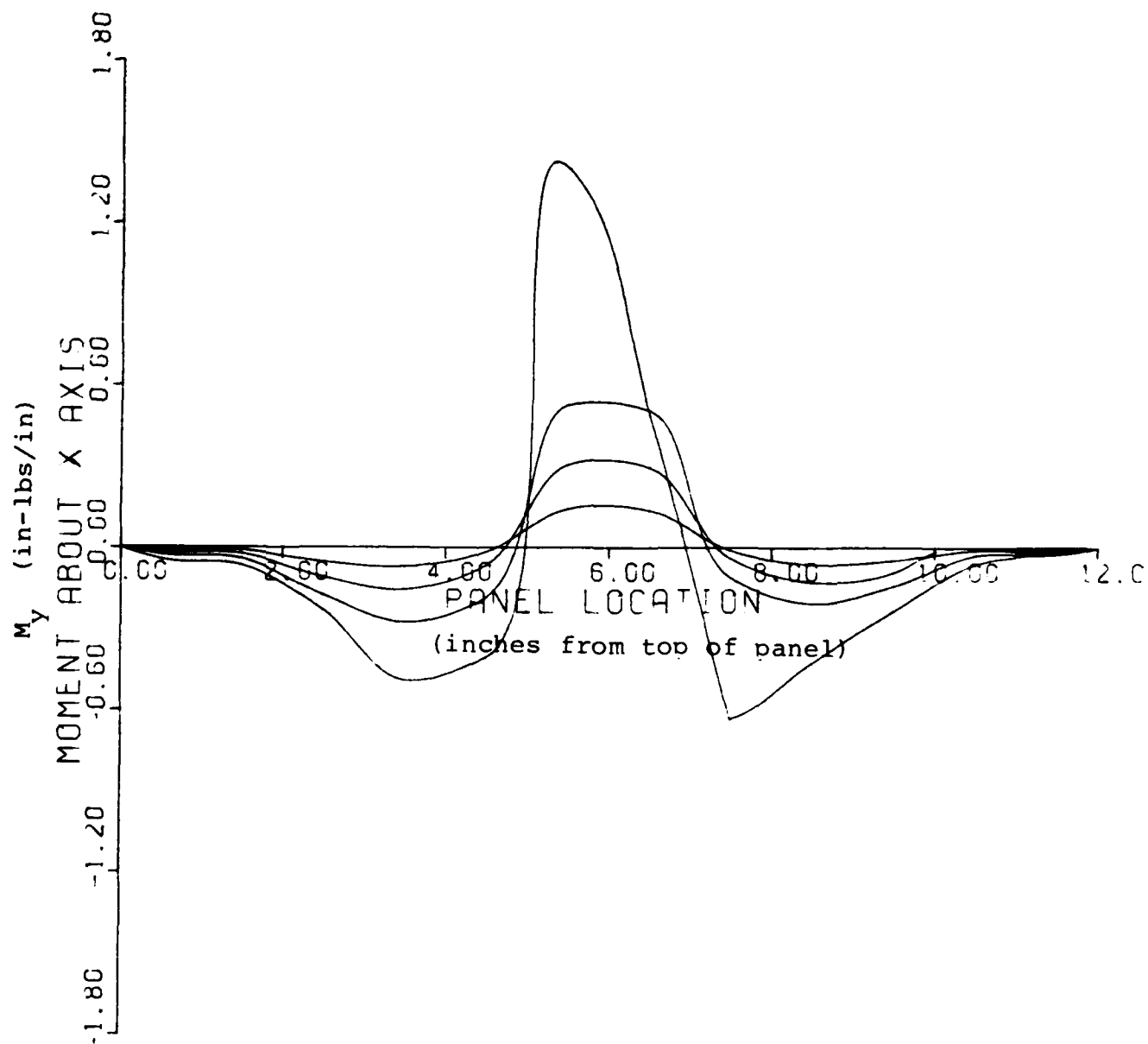


FIGURE 58: Moment Resultant Profiles

$[90, +45, -45, 0]_s$

M_y 7.5 Inches From Left edge of Panel

Load Levels Increase Away From Horizontal Axis

Load Levels (lbs/in) are 56, 106, 156, 215.9

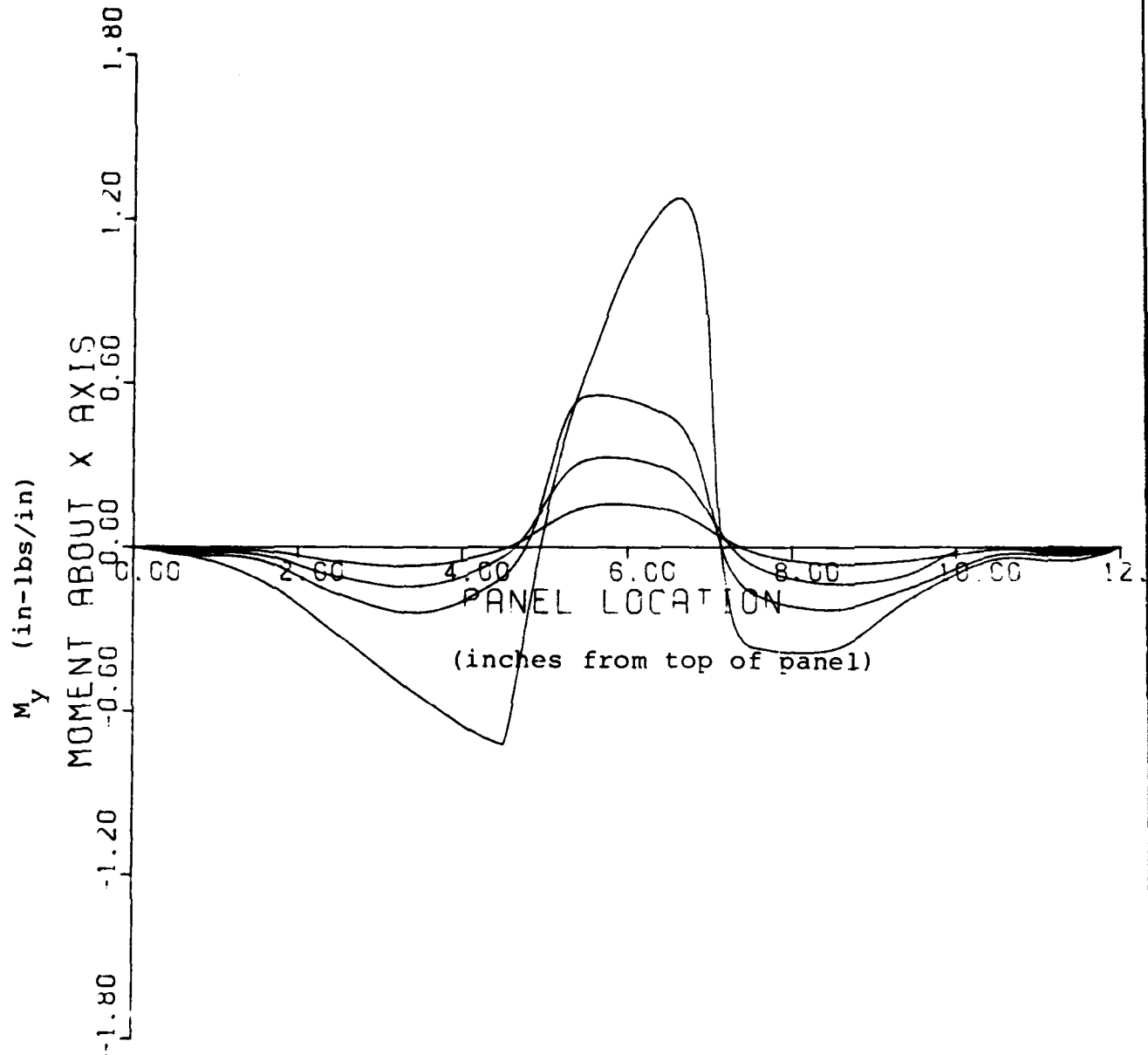


FIGURE 59: Moment Resultant Profiles

[90, +45, -45, 0]_s

M_y 9.5 Inches From Left edge of Panel

Load Levels Increase Away From Horizontal Axis

Load Levels (lbs/in) are 56, 106, 156, 215.9

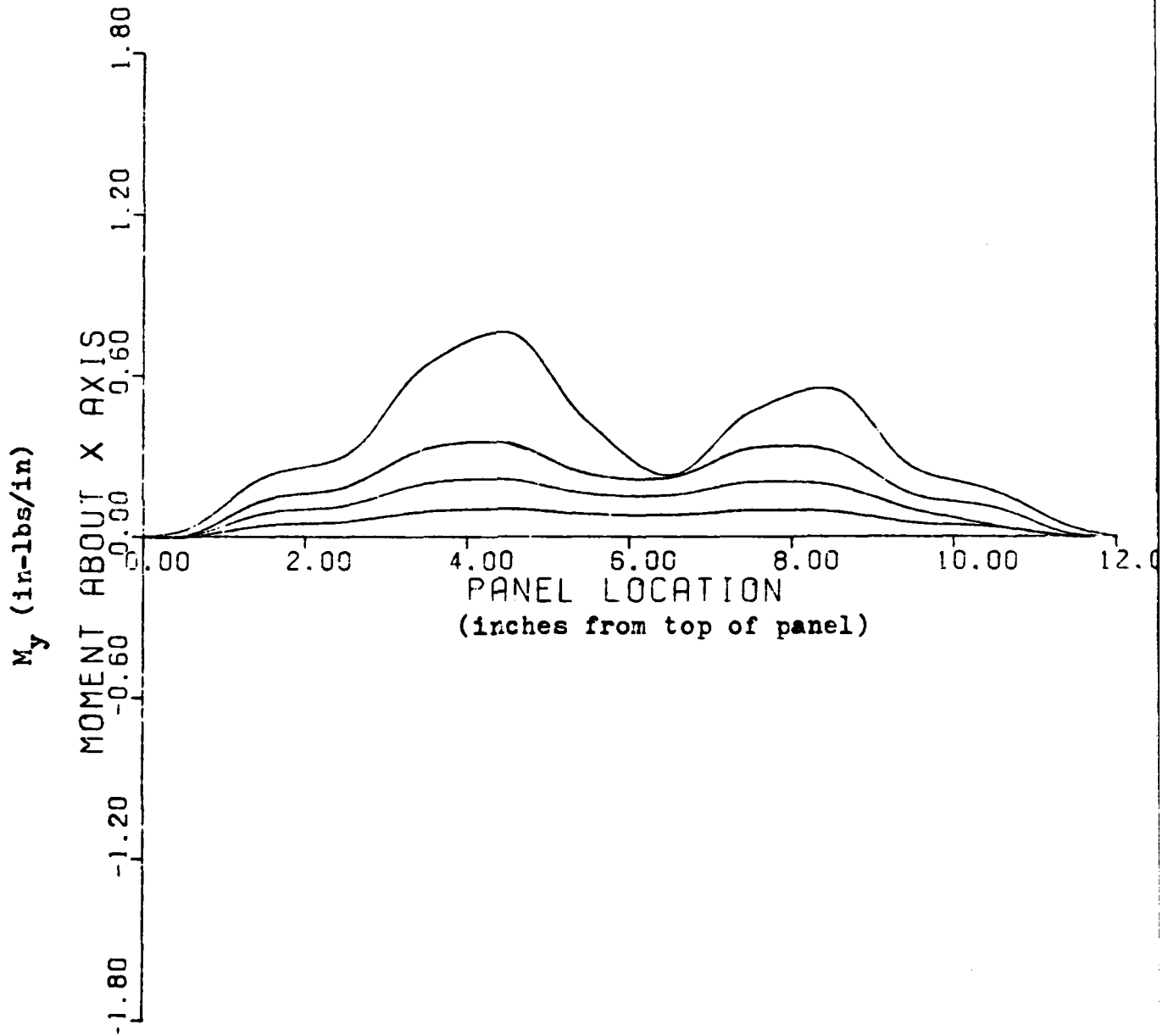


FIGURE 60: Moment Resultant Profiles

This corresponds to the symmetric radial displacement profiles previously shown. At the collapse load the symmetry of the moment resultant is lost. The trough that appeared in the displacement contours and was easily seen in the displacement profiles can once again be seen easily in the moment resultant profiles. Figures 45 through 48 show how the maximum moment resultant (M_x) goes from the upper left of the panel to the lower right at the collapse load. Likewise, Figures 49 through 52 show the M_y resultant at various rows down the panel and likewise indicate the trough of maximum concentrations at collapse. These eight figures correspond to the displacement trough seen in the displacement contours (Figure 35) of a $[0, +45, -45, 90]_s$ panel with a small cutout. Figures 52 through 60 show the same phenomena and correspond to the displacement contours shown in Figure 38. In recalling how the D_{22} term affected the radial displacements of the troughs in the two panels, an examination of the magnitude of the moment resultants is warranted.

In comparing the moment resultants for the different panels at the same location (i.e. Figure 45 with Figure 53, 46 with 54, etc.) one can notice a difference in the magnitude of the moment resultants. In comparing the moment resultant about the y axis (M_x) one notices that the magnitude of the moments for $[0, +45, -45, 90]_s$ panel is greater than the $[90, +45, -45, 0]_s$ panel. However, in comparing the moment about the y axis (M_y) the opposite is true. The moment

resultants for the $[90, +45, -45, 0]_s$ panel is larger than $[0, +45, -45, 90]_s$ panel. This can be accounted for by the bending stiffness matrix. In the two different ply layups the D_{11} and D_{22} terms are swapped (See Appendix B). In the $[0, +45, -45, 90]_s$ panel the D_{11} term is roughly 4 times the D_{22} term. This accounts for the way the magnitudes in the M_x and M_y moment resultants switch in the panels. Also the moment about the x axis (M_y) is less than the moment about y axis (M_x) for a given curvature in the $[0, +45, -45, 90]_s$ ply layup while the opposite is true for the $[90, +45, -45, 0]_s$ ply layup. This also can be seen in comparing Figures 45 through 60.

Why these troughs of displacements and moments appear can be explained by the eigenvectors of panels. Figures 61 and 62 is the eigenvector of the various panels with 2 inch by 2 inch cutouts. Figure 61 is the eigenvector plot of the $[0, +45, -45, 90]_s$ panel. One will notice that a trough of inward radial displacements run from the upper left to the lower right of the cutout. The eigenvector plot of the $[0, -45, +45, 90]_s$ panel is not shown however it is the same as Figure 61 except the trough of inward displacements is now oriented from the upper right to the lower left of the cutout. Figure 62 is the eigenvector plot of the $[90, +45, -45, 0]_s$ panel with a 2 inch by 2 inch cutout. Notice that the trough of negative displacement goes from the upper right to lower left of the cutout. In reviewing Figures 34 to 60 one can see

W Component of Eigenvector of $[0, +45, -45, 90]_s$ Panel
With a 2 Inch by 2 Inch Cutout

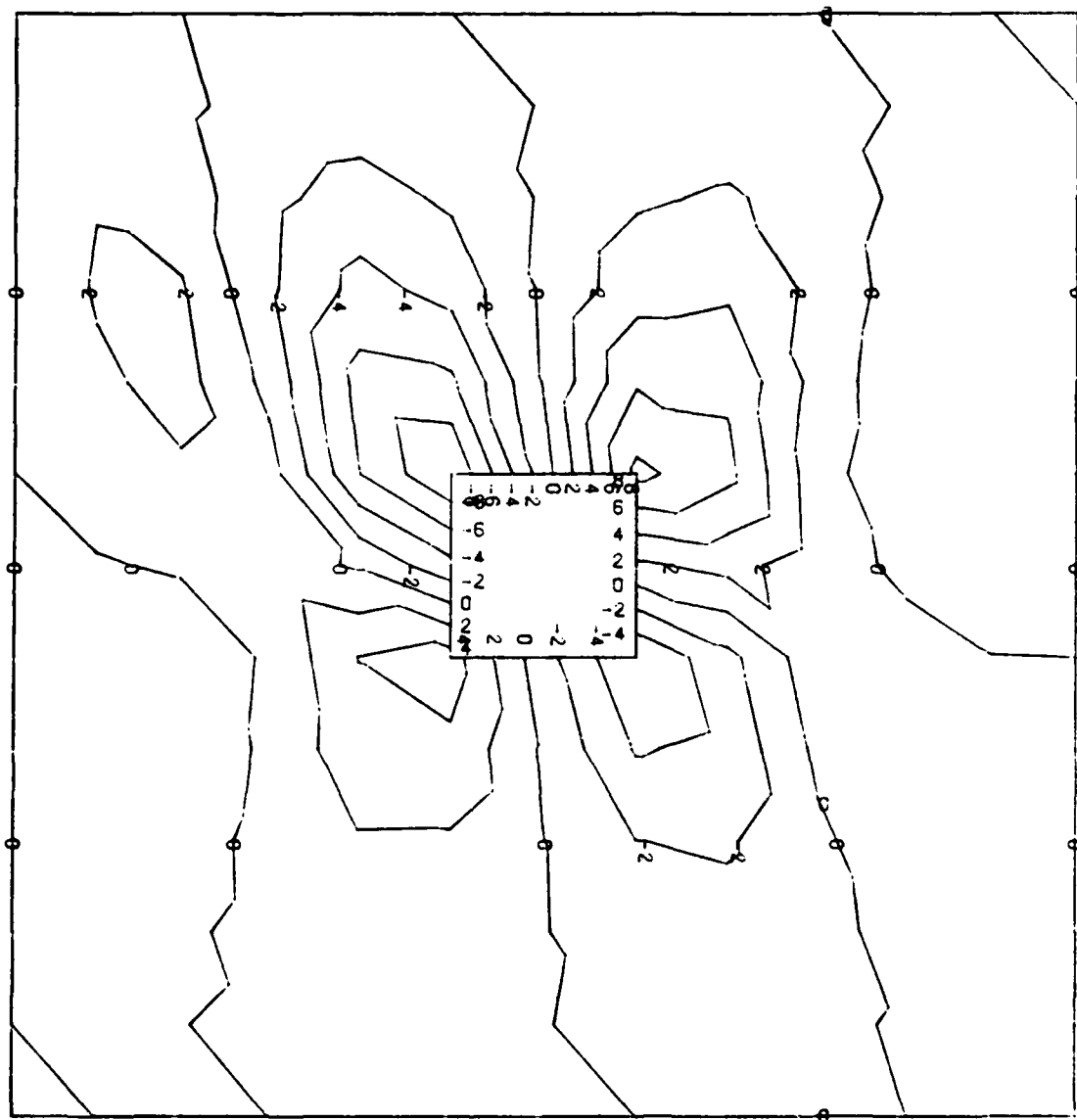


FIGURE 61: Eigenvector Contours

W Component of Eigenvector of $[90, +45, -45, 0]_s$ Panel
 With a 2 Inch by 2 Inch Cutout

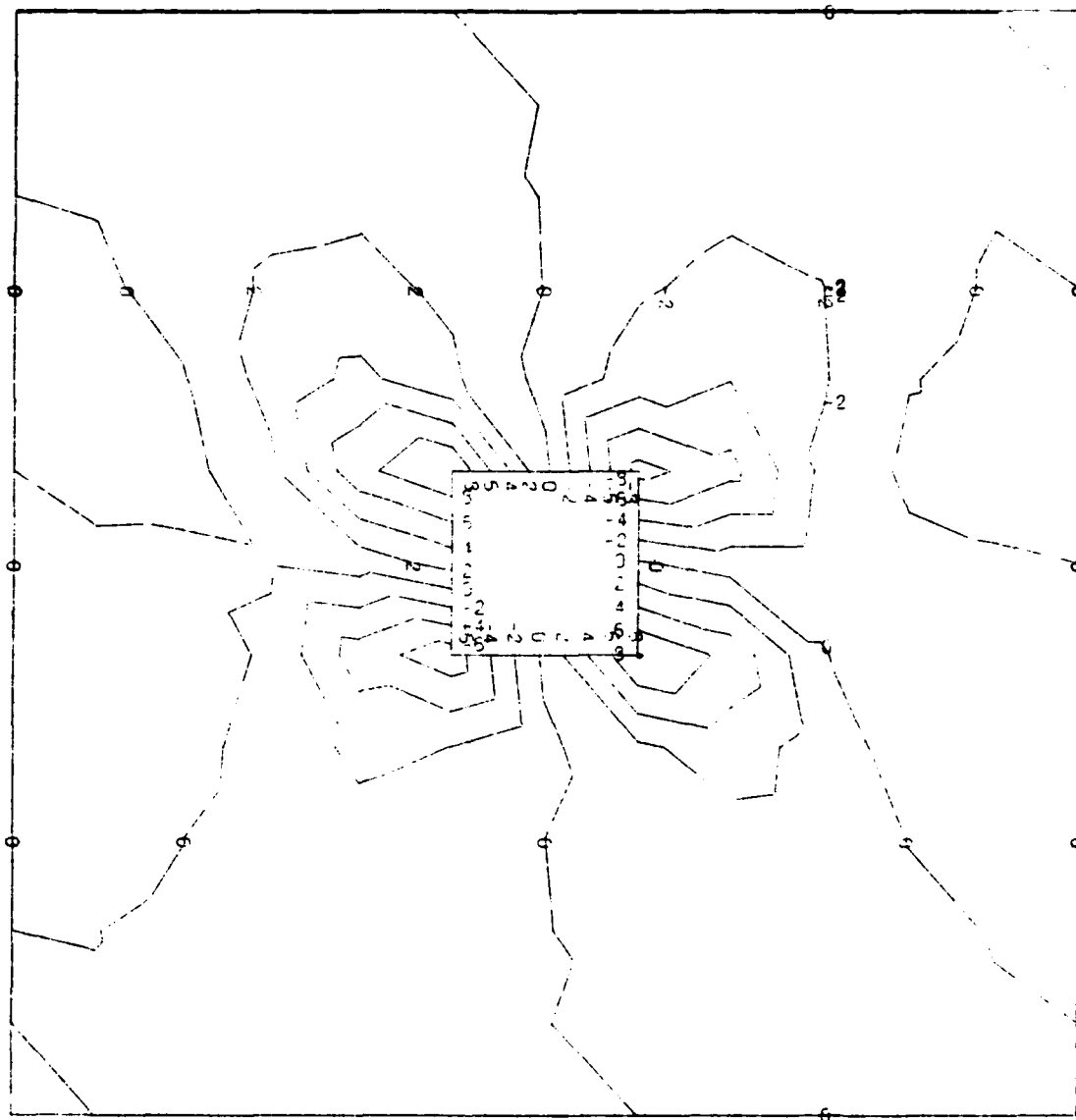


FIGURE 62: Eigenvector Contours

the history of the displacement pattern, that is how it develops and the shape as the load level is increased from zero up to collapse for the various panels with 2 inch by 2 inch cutouts.

As the load level is increased the radial displacements and moment resultants build symmetrically with respect to the horizontal and vertical axis of symmetry on the panel. As the collapse load is approached the panel has absorbed as much energy as it can. The displacement contours and the moment resultants are near their maximum and are still symmetric. When the load level is increased, that is more potential energy is added to the panel, the panel has reached its limit point and, therefore, in order to absorb more energy the displacement pattern shifts to that of the secondary loading path (the eigenvector) to absorb the additional energy. This was evident in all the displacement contour plots at the collapse load for all the panels analyzed with a 2 inch by 2 inch cutout as can be seen by comparing Figures 34 through 38 to Figures 61 and 62 for the respective panels.

Now that the effects of a small cutout have been examined with respect to the displacement patterns and moment resultants, the effect of the larger cutout (4 inch by 4 inch) will be examined. Figures 63 and 64 are the displacement contours of the radial displacements at 78.5 lbs/in and collapse load (131.2 lbs/in) respectively for the $[0, +45, -45, 90]_s$ panel with a 4 inch by 4 inch cutout. Likewise,

Load Level 78.5 lbs/in

Maximum Displacement = .042 inch

Ply Layup $[0, +45, -45, 90]_s$

Contour Levels Are In 10^{ths} of Maximum Displacement

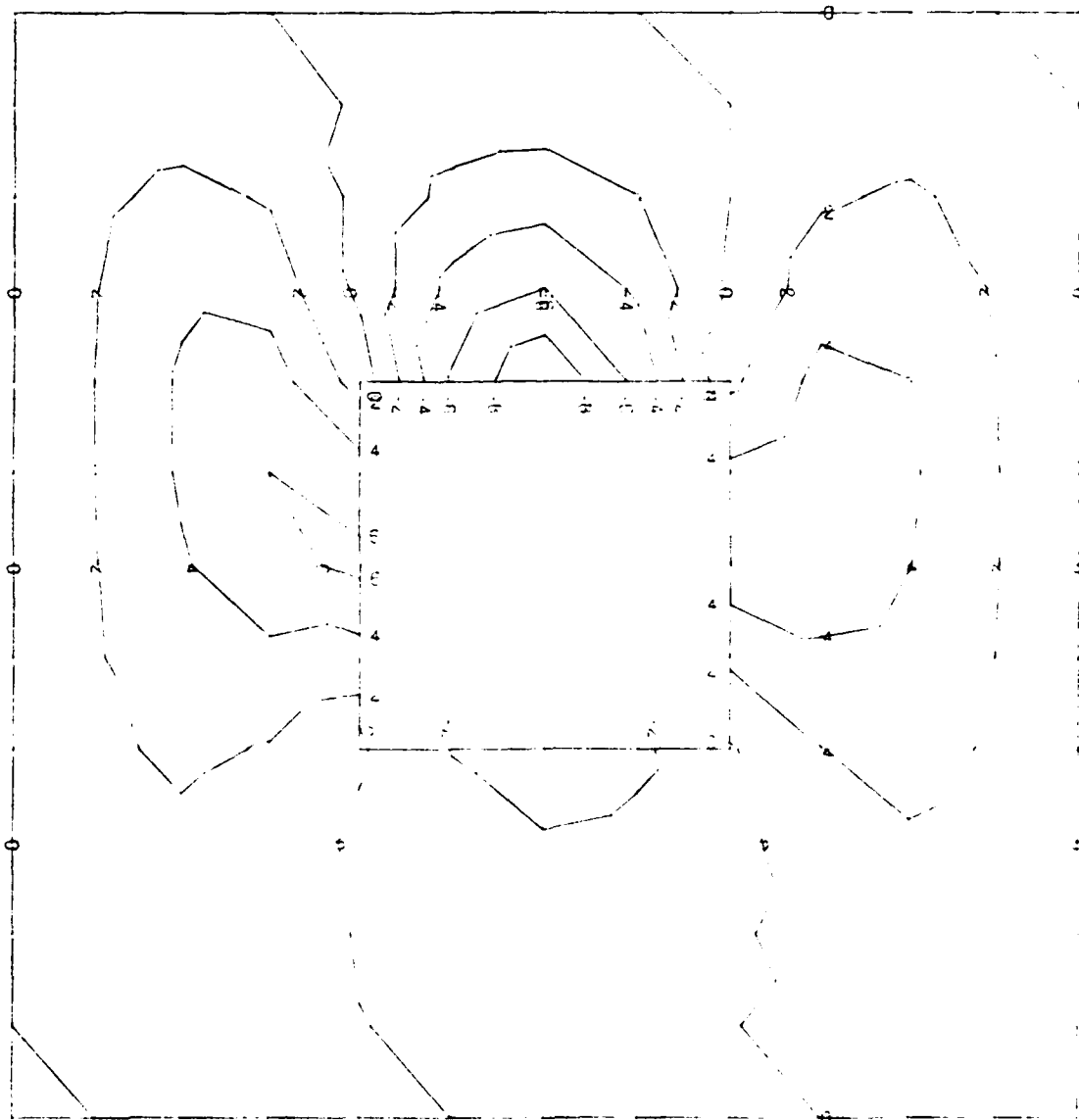


FIGURE 63: W Component Displacement Contours

Load Level 113.2 lbs/in

Maximum Displacement = .084 inch

Ply Layup $[0, +45, -45, 90]_s$

Contour Levels Are In 10^{ths} of Maximum Displacement

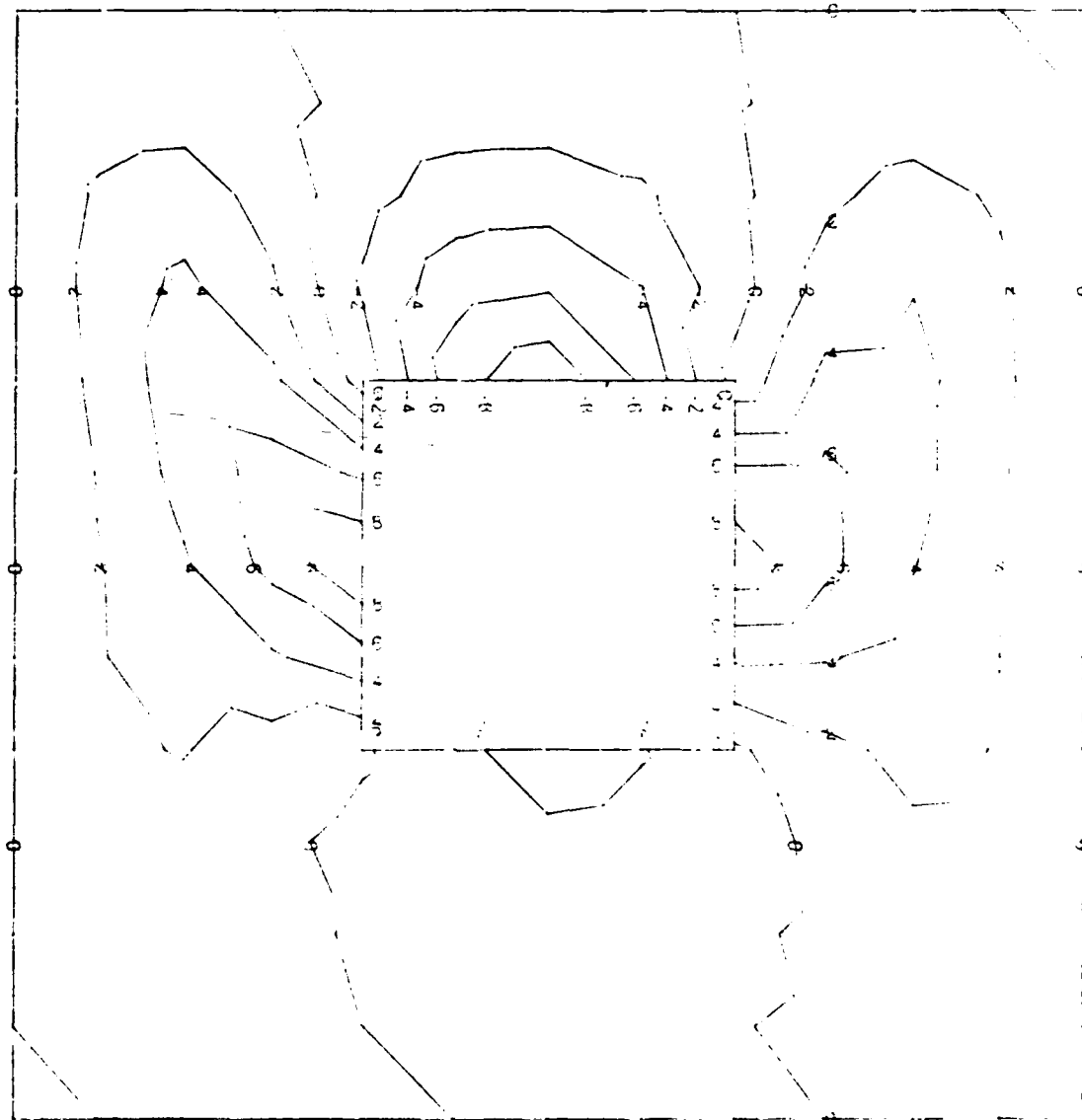


FIGURE 64: W Component Displacement Contours

Load Level 78.5 lbs/in

Maximum Displacement = .042 inch

Ply Layup $[0, -45, +45, 90]_s$

Contour Levels Are In 10^{ths} of Maximum Displacement

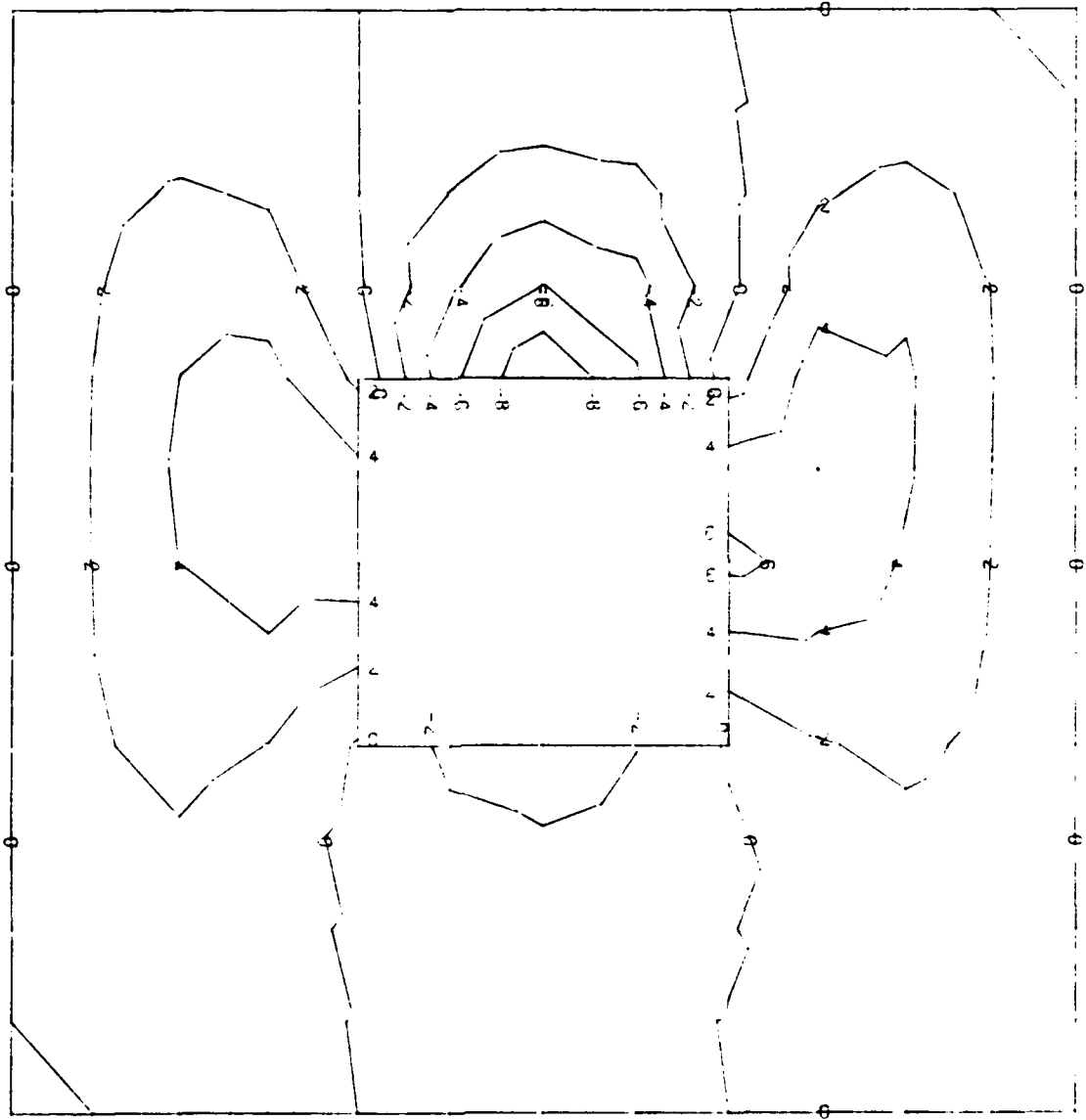


FIGURE 65: W Component Displacement Contours

Load Level 113.2 lbs/in
 Maximum Displacement = .084 inch
 Ply Layup $[0, -45, +45, 90]_s$
 Contour Levels Are In 10^{ths} of Maximum Displacement

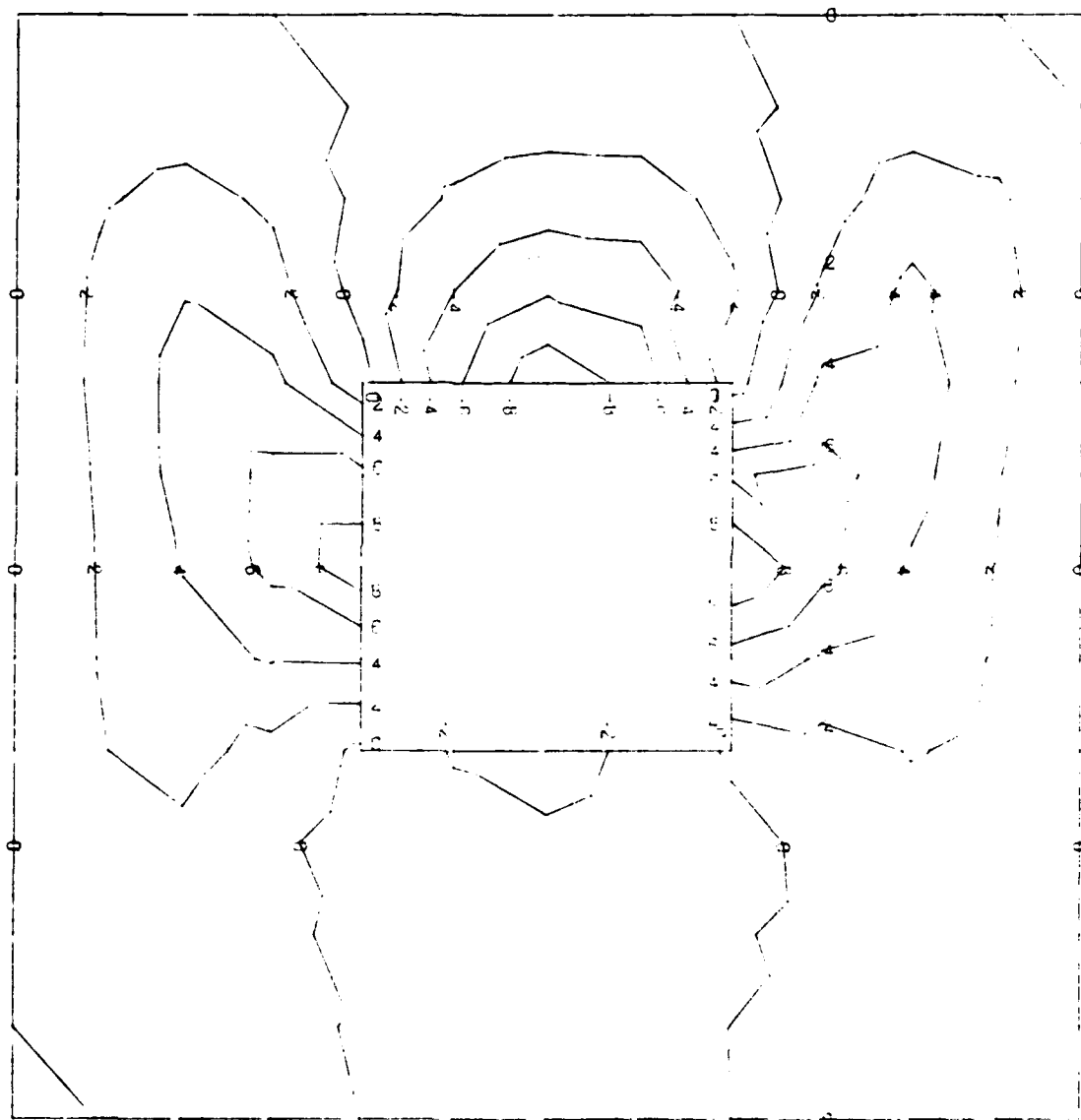


FIGURE 66: W Component Displacement Contours

Figures 65 and 66 are at the same corresponding load levels but for the $[0, -45, +45, 90]_s$ panel. In studying these four figures it can be seen that with a larger cutout the displacement pattern at collapse is more symmetric about the circumferential and longitudinal axis than the similar panel with the smaller cutout. This is because the larger cutout produces the bending effects earlier and the moment change is more spread out, therefore, a more symmetric displacement pattern. However, the slight amount of non-symmetry that is shown at the center of the cutouts vertical edges can be seen to change sides when the ply layup is changed by switching the 45° plies. This same thing was experienced with the smaller cutouts. The moment resultants follow the radial displacements as would be expected.

Figure 67 is the w component eigenvector contour plot of the $[0, +45, -45, 90]_s$ panel with a 4 inch by 4 inch cutout. In comparing the eigenvector plot to the displacement contours at collapse there is very little similarity. In essence, when the panel collapsed it did not go into the shape of the eigenvector as the panels with the smaller cutouts did. If the panel absorbs energy primarily through its axial stiffness (the uncut panel and small cutouts) then the displacement field at collapse is eigenvector oriented. However, if the panel absorbs energy through both the axial and bending stiffness then the displacement field is not

W Component of Eigenvector of $[0, +45, -45, 90]_s$ Panel
With a 4 Inch by 4 Inch Cutout

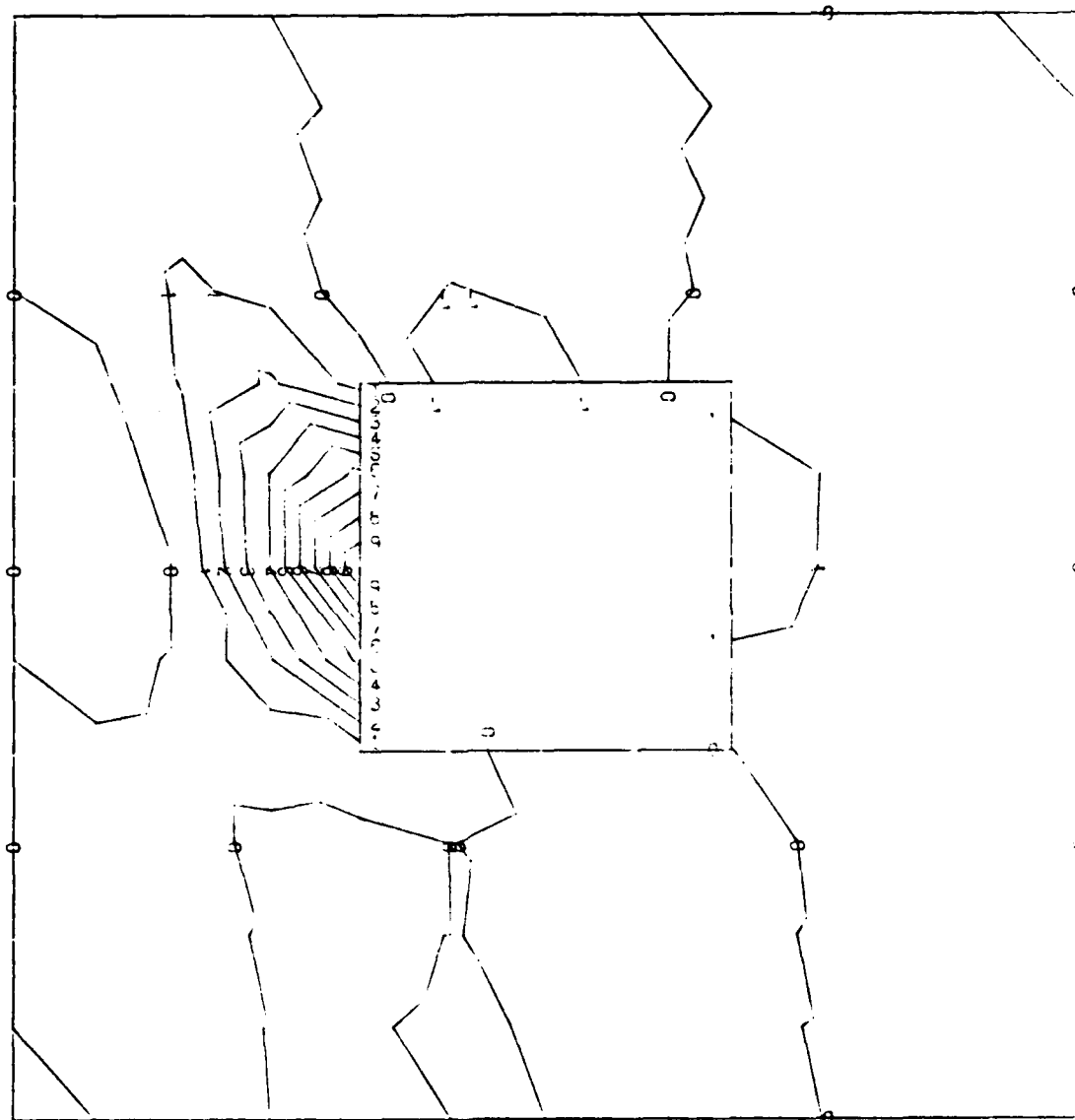


FIGURE 67: Eigenvector Contours

eigenvector oriented. This difference can also be explained by comparing the amounts of radial displacements.

Furthermore, the panels with the small cutouts all had radial displacements less than the thickness of the panel (.04 inches). The largest radial displacement in the panels with a small cutout was .037 inches and that was on the panels with the zero degree outside plies. On the other hand, the panels with the larger cutouts (4 inch by 4 inch) had radial displacements of .084 inches which is over twice the panels thickness. Therefore, the displacement field generated by the 2 inch by 2 inch cutout is not going to have that great of an effect on the nonlinear collapse mode since the radial displacements are small (less than the panels thickness). Therefore, at collapse the panel will behave almost linearly and will have the shape of the linear bifurcation while the radial displacements for the panel with the large cutout are over twice the panel thickness, their effect on the nonlinear collapse analysis will be greater. With these large displacements (greater than the panels thickness) the nonlinear effect of the cutout on the collapse analysis dictates the collapse displacement pattern. This pattern is symmetric and there is no shift to the secondary loading path, that is it followed the secondary loading path from the start. The nonlinearity of the presence of the 4 inch by 4 inch cutout is felt by the panel throughout its loading history while the nonlinearity of the smaller 2 inch by 2 inch cutout does not effect the panels displacement pattern as much.

The final item studied relative to panels with cutouts was a change in the boundary conditions. In all the previous panels studied, the boundary conditions were: (1) clamped on the top with a u free, (2) clamped on the bottom with no free DOF, and (3) u , v , and rotation about u free on the sides. A $[0, +45, -45, 90]_s$ panel with the small cutout (2 inch by 2 inch) was chosen to see the difference in the boundary conditions would create a drastic change. The change in boundary conditions was that v would be fixed on the sides of the panel with u and the rotation about u still free. The boundary conditions for the top and bottom of the panel remained the same.

Figures 68 and 69 are the plots of the displacement contours in the radial direction for the load levels of 81 lbs/in and at the collapse of 222.3 lbs/in. In comparing Figures 68 and 69 to Figures 34 and 35 there is very little difference and these are the corresponding load levels on the same panels with just the change in the boundary conditions. The panel with the v DOF fixed on the sides had a collapse load of 222.3 lbs/in with a top edge displacement of .0104 inches and a maximum radial deflection of .036 inches. All of these values are within 3% of the same values when v was free. Since there are such small radial displacements involved, and the nonlinear collapse analysis is close to the linear bifurcation analysis, the changing of the v DOF in the boundary condition on the panel with the small cutouts had an insignificant

Load Level 81 lbs/in

Maximum Displacement = .0084 inch

Ply Layup $[0, +45, -45, 90]_s$

Contour Levels Are In 10^{ths} of Maximum Displacement

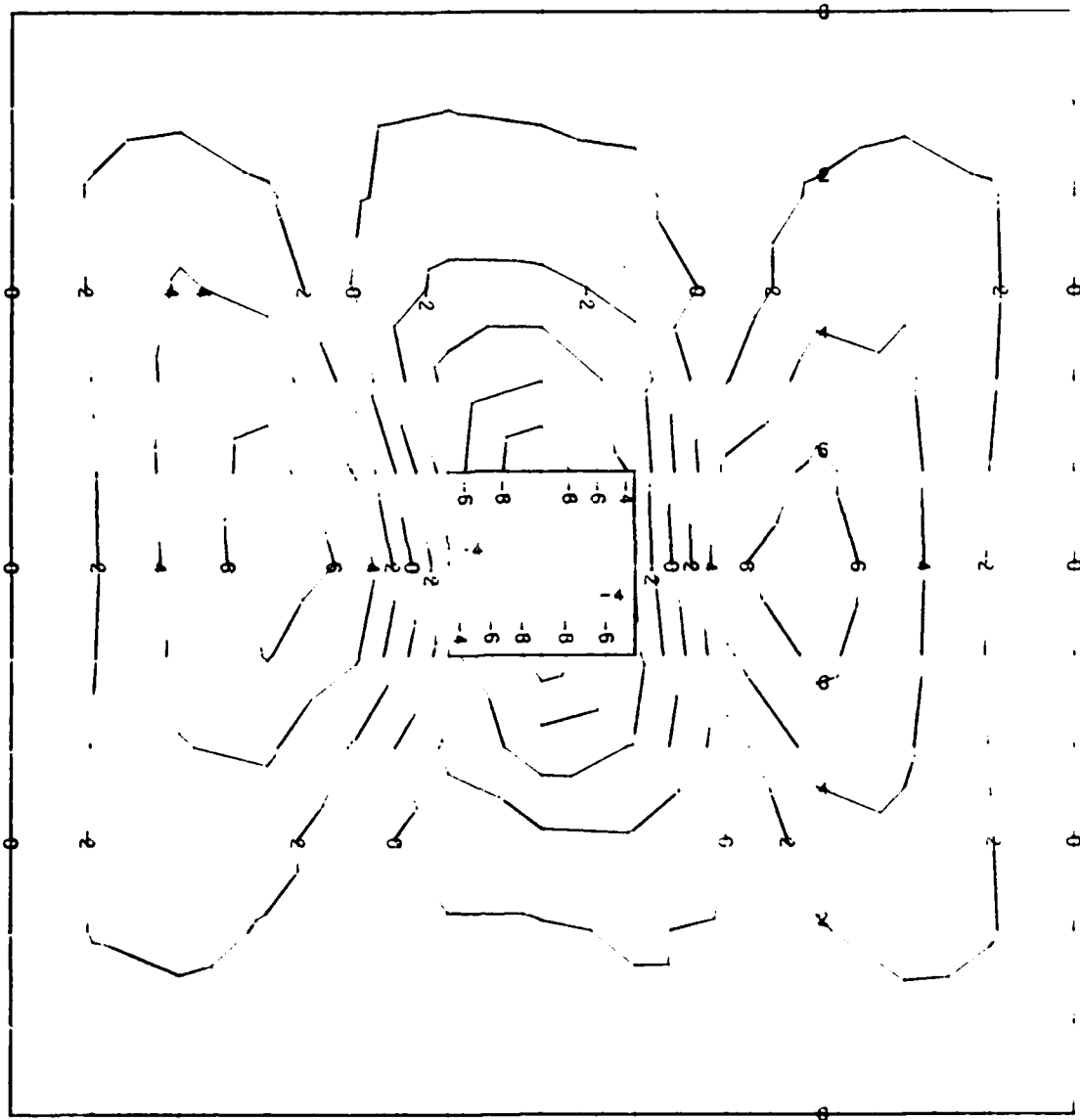


FIGURE 68: W Component Displacement Contours

Load Level 222.3 lbs/in

Maximum Displacement = .036 inch

Ply Layup $[0, +45, -45, 90]_s$

Contour Levels Are In 10^{ths} of Maximum Displacement



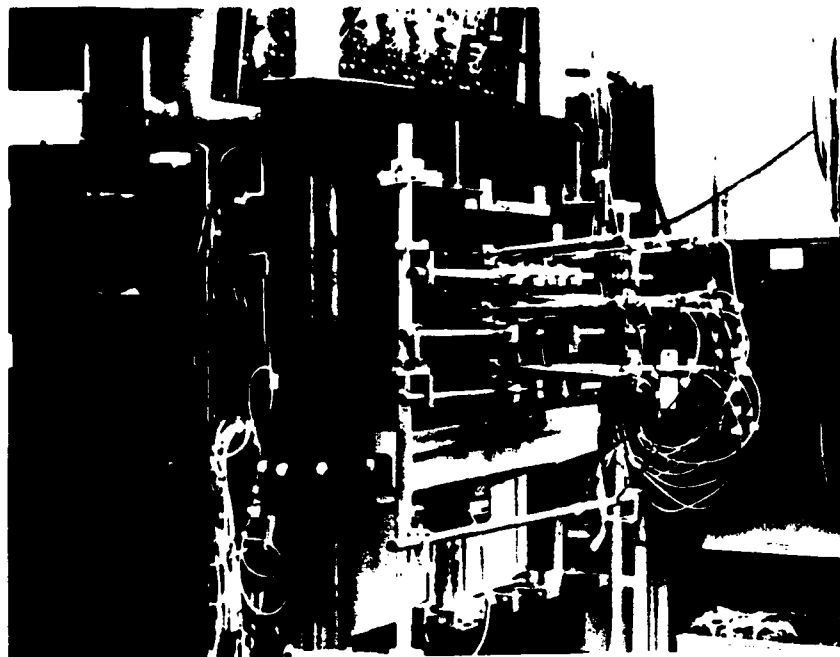
FIGURE 69: W Component Displacement Contours

effect on the panel. However, the effect would probably be greater on the larger cutouts with the larger displacements. However, this was not studied.

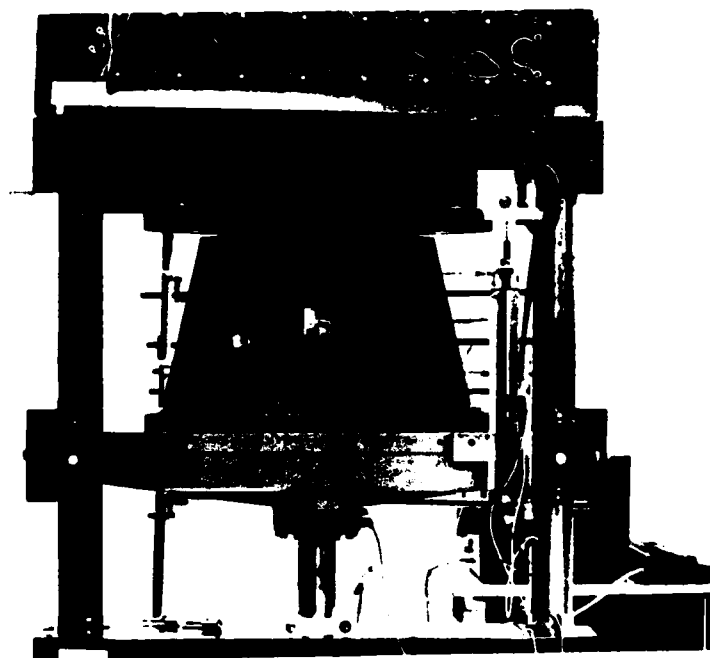
Experimental Analysis Versus Analytical Study

Since the previous sections of this study were purely analytical and some unexpected displacement patterns appeared on the panels with small cutouts, the author was able to have conducted a series of experiments on panels with small cutouts. Four different panels, with two different ply layups, were chosen. Two panels with a $[0, -45, +45, 90]_s$ layup and two panels with a $[90, -45, +45, 0]_s$ layup were studied. The Air Force Flight Dynamics Laboratory conducted the experimentation. The experimental setup and testing procedure were the same as previously used by M. L. Becker in reference [3]. There was a slight modification made in the loading platform which can be readily seen by comparing Figure 70 to the figures in reference [3].

The panel was loaded with incremental load steps so that a visual analysis could be made at various load levels. The author could see the symmetric displacement fields being generated by close observation at the lower load levels and this corresponded to the pattern shown in the analytical studies at the same load levels. As the collapse load was approached, the author heard a loud snap as the panel shifted



Front View of Panel with LVDT



Rear View of Panel

FIGURE 70: Experimental Setup



Front View of Panel



Rear View of Panel

FIGURE 71: Radial Displacements of Panel At Collapse

the displacement patterns. The large displacement patterns generated at the collapse load are shown in Figure 71 and are the same shape that were analytically predicted. A matrix of Linear Variable Displacement Transducers (LVDT) were arranged around the cutout and over the panel's surface in order to measure radial displacements. Therefore, it was possible to compare several discretely located points. The top edge displacement and five discrete points on the panel were chosen for comparison between the analytical and experimental displacements.

The two $[0, -45, +45, 90]_s$ panels' displacements were averaged in the following comparisons since they had the largest displacements and any error in the finite element model would be magnified. Figure 72 is the plot of the total load versus top edge displacements. As can be readily seen in the figure, the model using STAGS is stiffer than the actual panel. This same phenomena was evidenced earlier in the comparisons of the experimental panel with surface imperfections and was expected. The experimental panel had a collapse load of 2121 pounds which is 18% lower than the collapse load of 2592 pounds predicted by STAGS. The experimental panel had the largest top edge displacement because of the increased flexibility. STAGS predicted only 47% of the actual panels top edge displacement.

Figures 73 through 76 are the plots of the radial displacements of four discrete points on the panel. The point

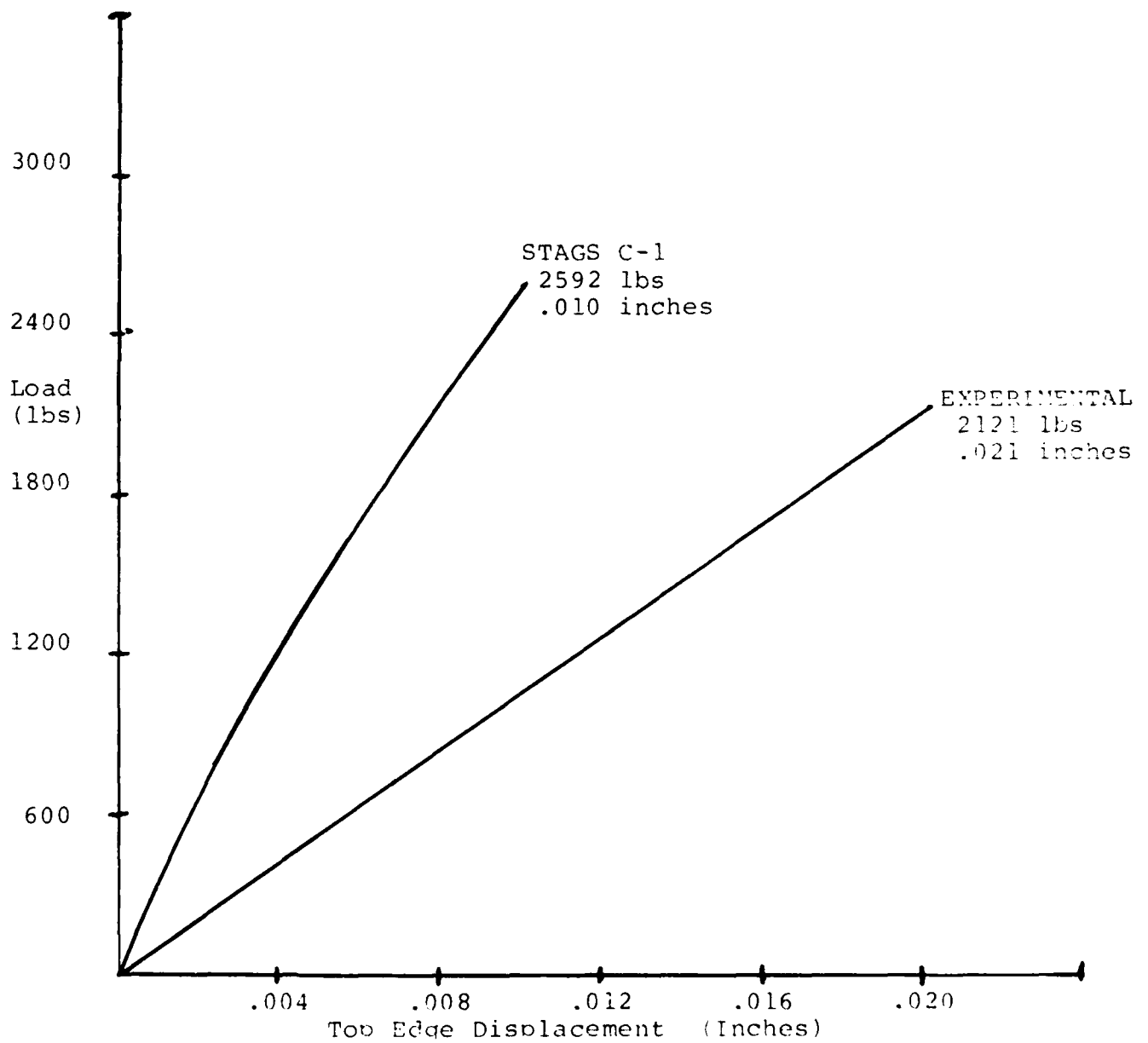


FIGURE 72: Load Versus Top Edge Displacement

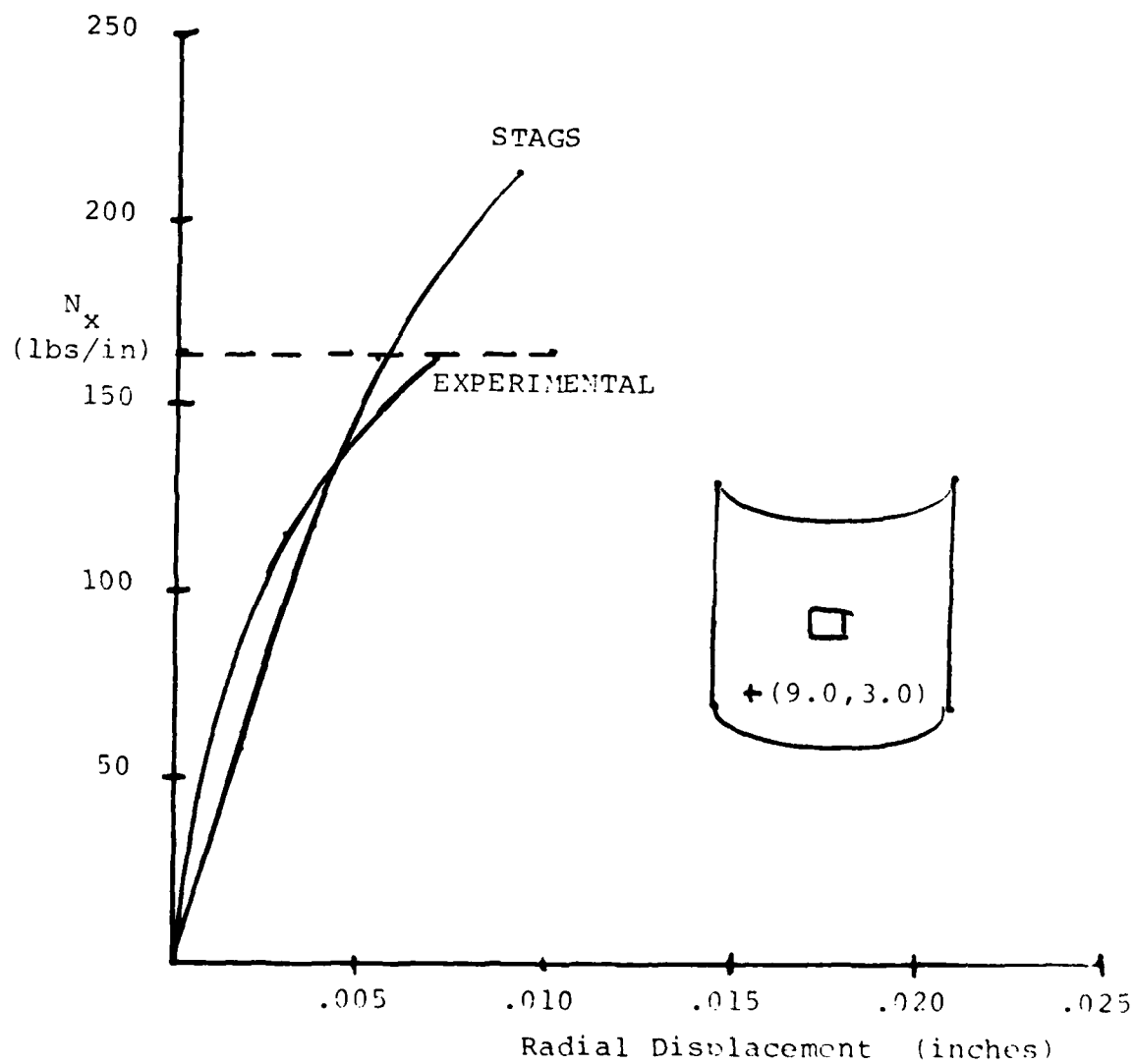


FIGURE 73: Load Versus Radial Displacement

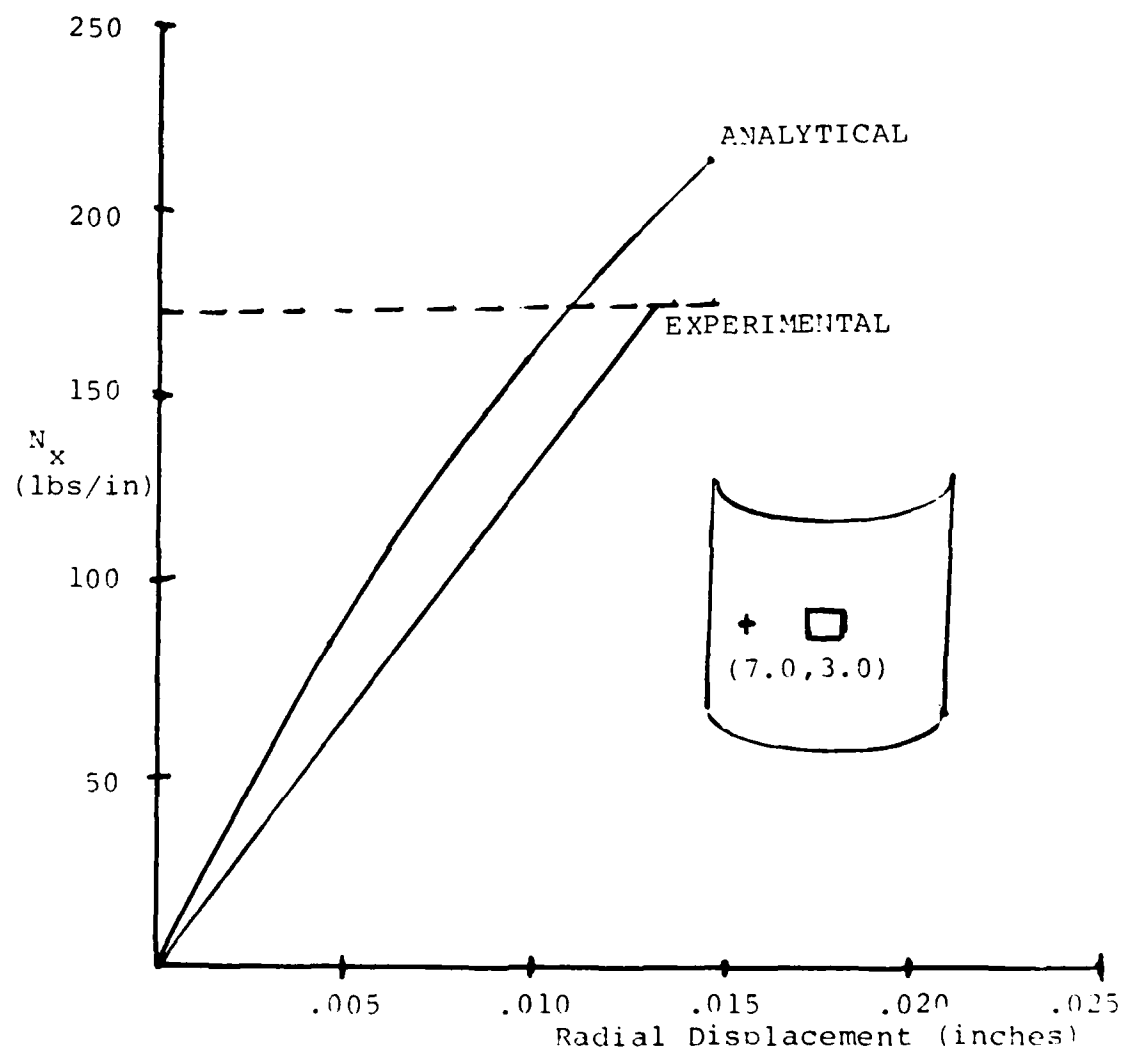


FIGURE 74: Load Versus Radial Displacement

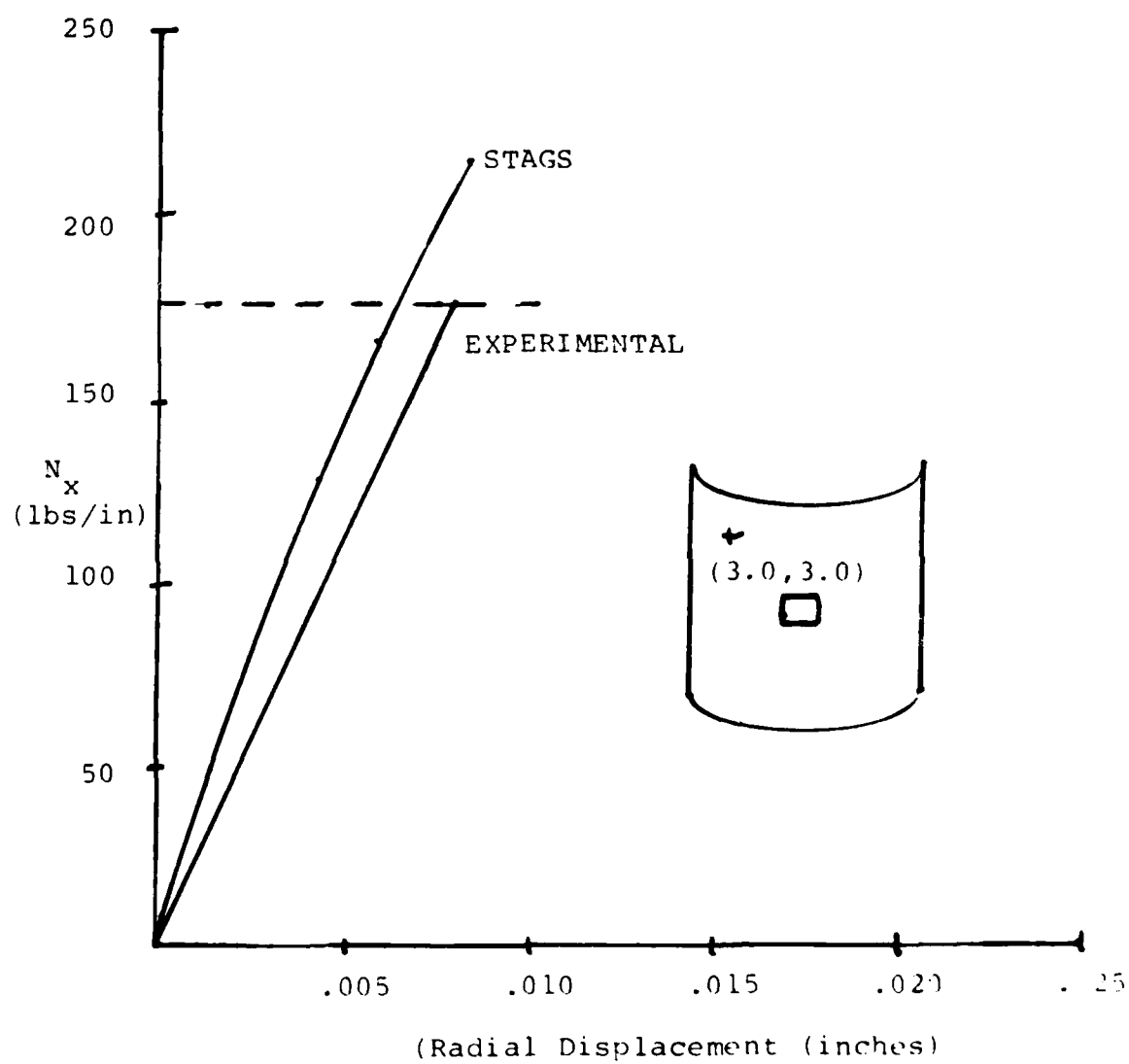


FIGURE 75: Load Versus Radial Displacement

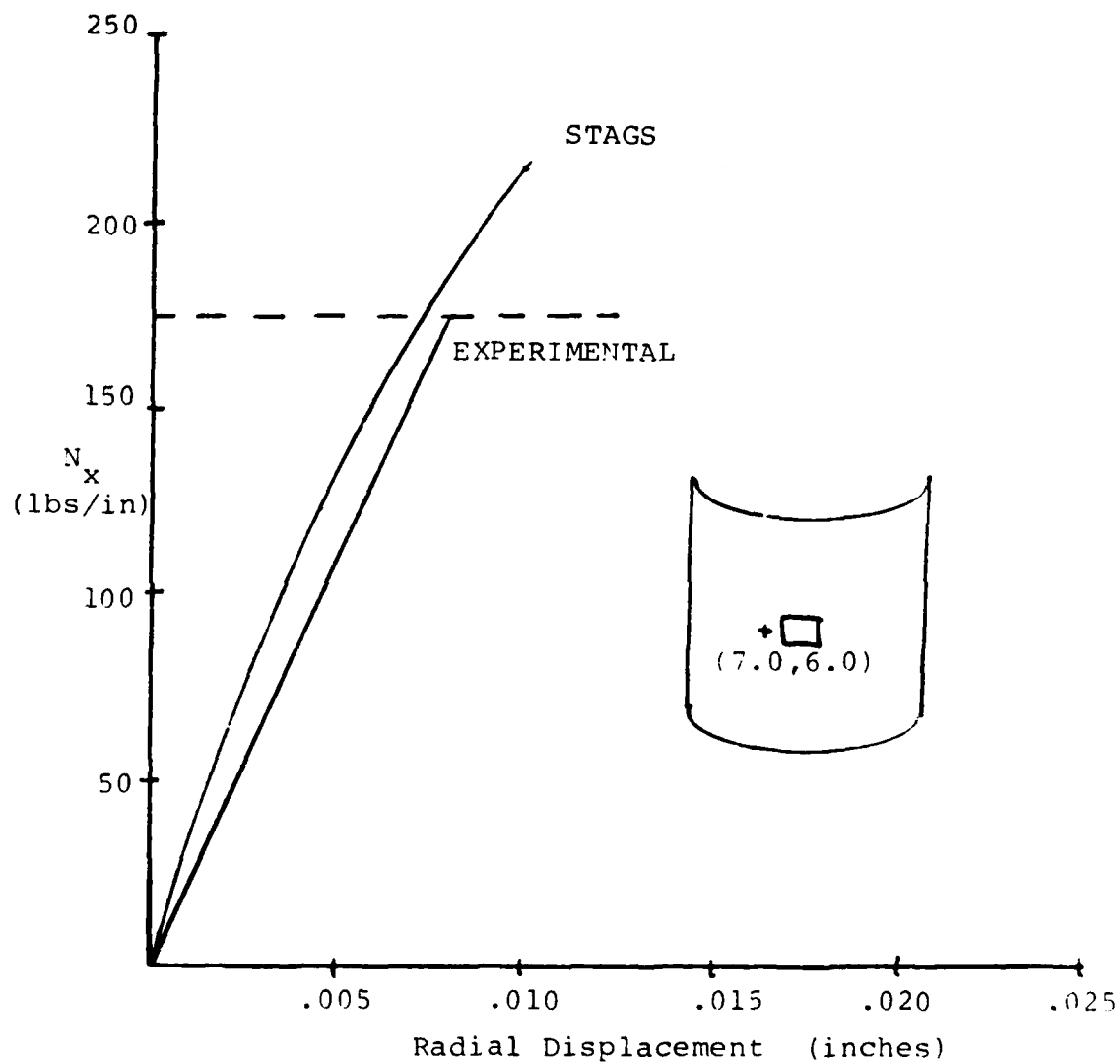


FIGURE 76: Load Versus Radial Displacement

of interest is indicated in the insert of each plot. The comparison of the radial displacements in these figure is best done at equal load levels.

By studying these figures, they show that the analytical results produced by the STAGS compare excellantly with the experimental results in the radial displacements. Figures 74 through 76 show that the displacements were relatively linear in STAGS for these selecteed points. The experimental analysis verified this. In Figure 73, the selected point showed a fairly large amount of nonlinearity in the analytical plot. The experimental test showed the same nonlinearity of this point, and the model with STAGS once again compared favorably in both displaying the nonlinearity as well as the magnitude of the displacement. For this point, the experimental panel displayed a little more nonlinearity in the radial displacements than STAGS did. However, STAGS showed more flexibility (e.g. at 100 lbs./in) during the lower load levels for this discrete point than the experimental panel. Therefore, as the load level increases, and the nonlinearity of the displacements for the experimental panel becomes greater, the two curves will intersect and at the higher load levels STAGS had the greatest stiffness. The end result is that with these two combined effects the radial displacement predicted analytically for this point are very close to the experimental displacements.

Figures 74 through 76 are the plots of discrete points which did not exhibit a great amount of nonlinearity. However, at all of these points the model was stiffer than the experimental panel which was expected.

The last point to be compared was the lower left corner of the cutout and is shown in Figure 77. Figure 77 shows that the experimental displacement is large at this point. Therefore, a greater coupling effect is resulting at this point than is present in the analytical analysis. The reader should observe that the radial displacement is 30% greater than the thickness of the panel in the experimental analysis. The analytical model did show that there would be the greatest amount of nonlinearity at this particular point as well as the largest radial deflections. The experimental panel verified this fact.

Overall, the experimental study gave the same results as the analytical study. The unexpected displacement pattern that appeared in the analytical study was verified by the experimental analysis. The model employed with STAGS did an excellent job in predicting the magnitude of the radial displacement and compared very favorably with the experimental analysis. The experimental analysis has verified the analytical study of a panel with small cutout.

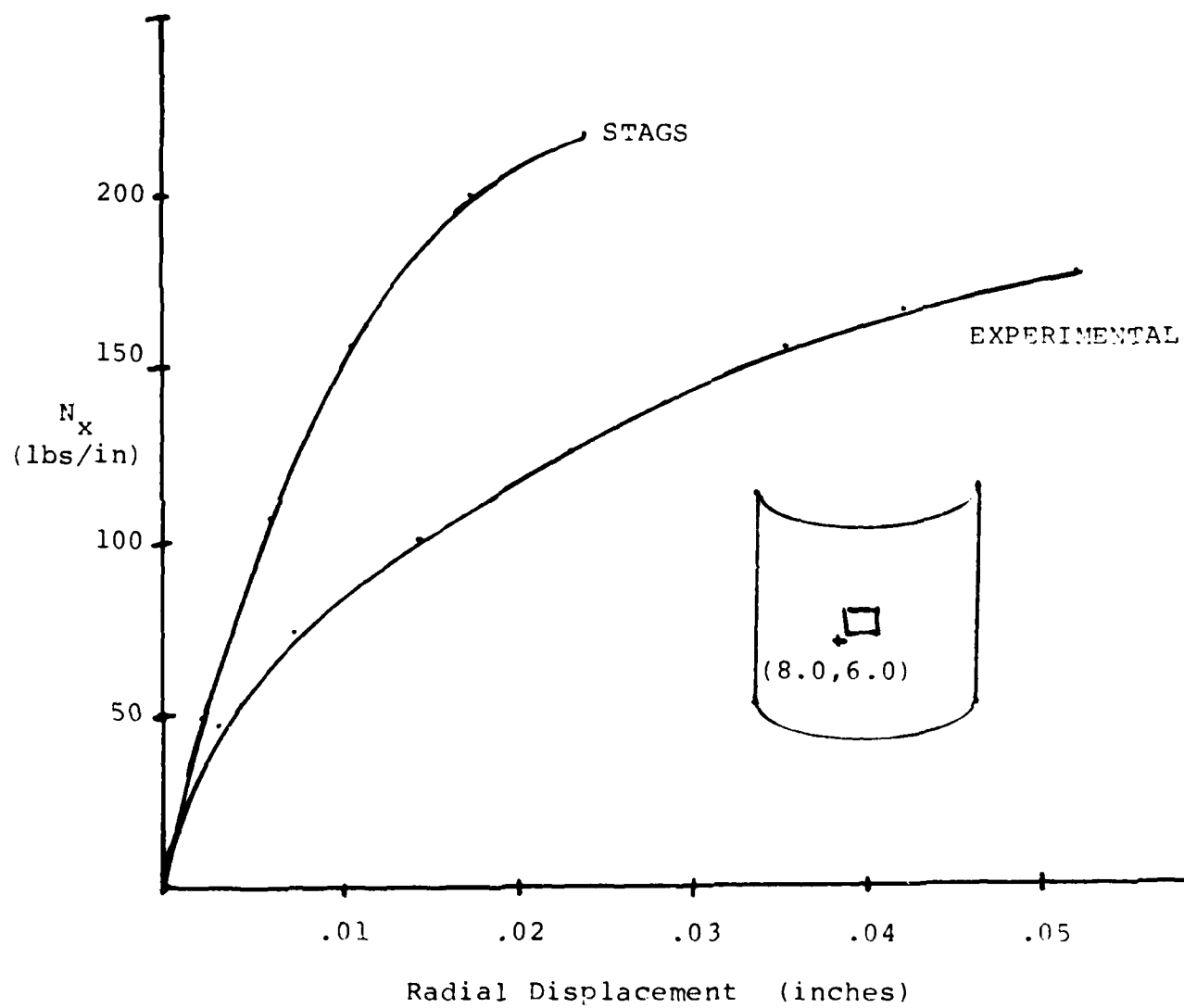


FIGURE 77: Load Versus Radial Displacement

Conclusions

The following statements and conclusions are based on the analysis presented in this paper:

1. In different element comparisons it was observed that the γ DOF in the 411 element is not needed in a linear analysis. However, for a nonlinear collapse analysis this extra DOF is necessary for compatability between elements when modelling a curved panel with flat elements undergoing relatively large rotation.

2. STAGS C-1, with a 411 element of one square inch or less, can accurately model a composite panel with surface imperfections or cutouts. The surface imperfection cannot be smaller than the span of 2.8 elements for each half sine wave.

3. Using the nonlinear collapse analysis in STAGS C-1 with the 411 element, analytical top edge displacements and collapse load agrees quite well with experimental data obtained for a composite panel with accurately measured surface imperfections. There has to be enough measurements made on a panel to accurately predict the shape and size of the surface imperfection in order that it may be modeled.

4. The number of surface imperfections that a panel has affects the magnitude of the collapse load. With no imperfections a panel will have the collapse load of the linear bifurcation. As the number of imperfections is

increased the collapse load decreases, this was based upon 9 surface imperfections for the panels analyzed. After that, as the number of imperfections is increased the level collapse load is increased.

5. The displacement pattern in the radial direction of the panels with the surface imperfections followed the initial shape of the imperfection. The radial inwards displacements were of a greater magnitude than the outward displacements at collapse.

6. A surface imperfection in the shape of the eigenvector does not produce the lowest collapse load.

7. The collapse characteristics of composite panels are dependent on the ply layup and the size of the cutouts.

8. Small cutouts (less than 5% of the panel surface area) have a displacement pattern, at the collapse load, that is different than the larger cutouts. The smaller cutouts displacement pattern will build symmetrically about the circumferential and longitudinal axis of symmetry and at the collapse load, snap into the displacement pattern of the eigenvector. The larger cutout had a displacement pattern that stayed fairly symmetric at collapse and was close to the isotropic collapse pattern.

9. The load bearing capability of a composite panel is very sensitive to the presences and size of a cutout.

10. Changing the vertical boundary conditions in the circumferential direction on a composite panel with the small cutout had a negligible effect on the load bearing capability and displacement pattern.

11. The radial displacements from the analytical study of panels with small cutouts compared extremely favorably with the experimental displacements.

12. The finite element model and the results of the analytical study of panels with small cutouts has been verified experimentally.

BIBLIOGRAPHY

1. Wilkens, D. J. "Compression Buckling Tests of Laminated Graphite-Epoxy Curved Panels," AIAA Paper 74-32, Presented at the AIAA 12th Aerospace Sciences Meeting, Washington, D.C., January 30-February 1, 1974.
2. Sobel, L. H., Weller, T. and Agarwal, B. L. "Buckling of Cylindrical Panels," Computer and Structures, 6: 29-35 (February, 1976).
3. Becker, M. L., Palazotto, A. N., and Khot, N. S. "Instability of Composite Panels," Journal of Aircraft, 18: 739-743, (September, 1981).
4. Almroth, B. O. "Influence of Edge Conditions on the Stability of Axially Compressed Cylindrical Shells," AIAA Journal, 4: 134-140, (January, 1966).
5. Tvergaard, V. "Buckling of Elastic-Plastic Cylindrical Panel Under Axial Compression," International Journal of Solid Structures, 13: 957-970, (1977).
6. Rehfield, L. W. and Hallauer, W. L. "Edge Restraint Effect on Buckling of Compressed Curved Panels," AIAA Journal, 6: 187-189, (January, 1968).
7. Viswanathan, A. V. and Tamekuni, M. Elastic Buckling Analysis for Composite Stiffened Plates and Other Structures Subjected to Biaxial Inplane Loads. NASA CR-2216. Washington, D.C.: National Aeronautics and Space Administration, September 1973.
8. Bauld, N. R., Jr. and Khot, N. S. "A Numerical and Experimental Investigation of the Buckling Behavior of Composite Panels," Computer and Structures, 15: 393-403, (April, 1982).
9. Satayamurthy, K., Khot, N. S., and Bauld, N. R., Jr. "An Automated, energy Based, Finite Difference Procedure for the Elastic Collapse of Rectangular Plates and Panels," Computer and Structures, 11: 239-249, (March, 1980).

10. Bauld, N. R., Jr. Experimental and Numerical Analysis of Axially Compressed Circular Cylindrical Fiber Reinforced Panels with Various Boundary Conditions. AFWAL-TR-81-3158. Wright-Patterson AFB, Ohio: Air Force Wright Aeronautical Laboratory, August 1981.
11. Bauld, N. R., Jr. and Satayamurthy, K. Collapse Load Analysis for Plates and Panels. AFFDL-TR-79-3038. Wright-Patterson AFB, Ohio: Air Force Flight Dynamics Laboratory, May 1979.
12. Cervantes, J. A. and Palazotto, A. N. "Cutout Reinforcement of Stiffened Cylindrical Shells," Journal of Aircraft, 16: 203-208, (March, 1979).
13. Starnes, James H., Jr. and Rouse, Marshall. "Postbuckling and Failure Characteristics of Selected Flat Rectangular Graphite-Epoxy Plates Loaded in Compression," AIAA Paper 81-0543, Presented at the 22nd Structures, Structural Dynamics and Materials Conference, Atlanta, Georgia, April 6-8, 1981.
14. Starnes, James H., Jr., Knight, Norman F., Jr., and Rouse, Marshall. "Postbuckling Behavior of Selected Flat Stiffened Graphite-Epoxy Panels Loaded in Compression," AIAA Paper 82-0777, Presented at the 23rd Structures, Structural Dynamics and Material Conference, New Orleans, Louisiana, May 10-12, 1982.
15. Thomas, K. and Sobel, L. H. Evaluation of the STAGS C-1 Shell Analysis Computer Program. WARD-10881. Madison PA: Westinghouse Advance Reactors Division, August 1981.
16. Almroth, B. O., Brogan, F. A., and Stanley, G. M. Structural Analysis of General Shells Volume II User Instructions for STAGS C-1. LMSC-D633837. Applied Mechanics Laboratory, Lockheed Palo Alto Research Laboratory, January 1981.
17. Almroth, B. O. and Brogan, F. R. Numerical Procedures for Analysis of Structural Shells. AFWAL-TR-80-3129. Wright-Patterson AFB, Ohio: Air Force Wright Aeronautical Laboratory, March 1981.
18. Jones, R. M. Mechanical of Composite Materials. Washington, D.C.: Scripta Book Company, 1975.
19. Brush, D. O. and Almroth, B. O. Buckling of Bars, Plates, and Shells. New York: McGraw-Hill, Inc., 1975.

18. Jones, R. M. Mechanical of Composite Materials. Washington, D.C.: Scripta Book Company, 1975.
19. Brush, D. O. and Almroth, B. O. Buckling of Bars, Plates, and Shells. New York: McGraw-Hill, Inc., 1975.
20. Owen, D. R. J. and Hinton, E. Finite Elements in Plasticity Theory and Practice. Swansea, U.K.: Pineridge Press Limited, 1980.
21. Almroth, B. O., Stern, P., and Bushnell, D. Imperfection Sensitivity of Optimized Structures. AFWAL-TR-80-3128. Wright-Patterson AFB, Ohio: Air Force Wright Aeronautical Laboratory, March 1981.

APPENDICES

APPENDIX A

User Problems With STAGS-1 and STAPL

This appendix is to supplement the users manual for STAGS and to help overcome some of the problems this author encountered in using STAGS on the ASD Cyber computers. In doing this thesis the author ran into five basic problems in using the computer code. Each problem will be addressed and briefly explained how they were overcome.

The first problem encountered in this project was to trigger the nonlinear branch of the computer code. If the imperfection is too small to cause rotations the nonlinear branch of STAGS will not be triggered. However, it will appear from the output that the imperfection has triggered the nonlinear branch of STAGS. A quick and easy way to check whether it has triggered is to plot the determinate of the stiffness matrix versus applied load. The determinate should approach zero when nonlinear collapse is going to occur. If the nonlinear branch has not been triggered there are two possible ways to correct this. The first is to simply increase the amplitude of the imperfection. The second is to apply a point load with a zero load factor increment so it will not increase in magnitude when the load step is incremented. One or two small point loads will usually help trigger the nonlinear branch. However, problems were encountered when too many point loads were used in trying to

model different shapes of imperfections because the stiffness matrix became very unstable and collapse would occur at a very small load.

After the nonlinear branch was triggered two problems arose almost simultaneously exceeding the mass storage limit of the Cyber and the restart capability of STAGS. To extend the mass storage of the Cyber an additional job control card was necessary. This was accomplished by adding the job control card command "Limit, 7000" prior to STAGS 1 (Figure A1). The restart problem is not that simple. There are three data cards for STAGS that must be correct for the restart capability to work. The first is the B1 data card. The post processing switch IPost 1 can be defaulted to zero in which only the last three load steps will be available for restart or if any other positive integer is used all load steps will be available for restart. The second card is the D1 strategy parameter card. NSEC must be selected to be smaller than the CPU seconds requested on the job control card. If the run is a restart from a previous run then ISTART must be the load step that you want to restart, insuring that the load step was saved from the previous run with the IPOST 1 parameter. The third card in this sequence is the C1 Load Multiplier record. For a restart to occur STLD(1) must agree with the load desired from the load step selected by ISTART (See Figure A2). One other problem that is unique to the Cyber operating system is which computer should do the job,

CSA or CSB? When a job goes to CSA the time field requested by the user on the job control card is cut in half. This leads to problems on restart because NSEC on the D1 data card is not halved. Therefore, the job will usually terminate without the program having a normal flow. This can be avoided by either specifying to use CSB or insuring that NESC is less than half of the CPU time requested on the job card. This is accomplished by routing the Batch Stream to Input. The final item on restart is TAPE 22 must be saved from the previous run and reattached in order to get a restart. Make sure that when it is reattached that it is made a local file because the program will try to write on it. See Figure A1 for a listing of the job card and Figures A2 and A3 for example listings of the data deck. In the control cards both TAPE 22 and TAPE 21 are saved as permanent files and the data deck will begin a new case saving the solution data every third step and terminating after 3300 seconds.

The next problem that was encountered was using the plot routine that is associated with STAGS, known as STAPL. The version of STAPL was previously altered by another user before I received it and the Update tape was lost. The previous user modified STAPL so that it could only be used on the Calcomp 1038. Figure A4 is an example data deck for STAPL, plotting 12 different plots. STAPL requires that TAPE 21 and TAPE 22 be saved and that the B1 card for STAGS 1 save the model geometry and primary solution data. STAPL can

either be run in conjunction with STAGS or it can be run separately from it. I did it both ways. In running STAPL in conjunction with STAGS you need to know before hand what load steps and items you want to plot. You will have to return TAPES 2, 10, 11, 12, 13, and 14 prior to executing STAPL. The plot file will be generated on TAPE 47 and all you have to do is route it to the plotter. If you are going to run STAPL separately, TAPES 21 and 22 will have to be reattached prior to executing. Note that in STAPL none of the secondary solution data that was plotted could be verified. I do not think that it is operational. I only had success with the primary solution data.

The last problem I had was the computer operators at AFIT and their working schedule. Many times the output from STAGS is long and will either be terminated by the operator before it is done printing or will sit in the output queue a day or so before it is printed. With the extremely long files (over 160 record blocks) that need to be saved for either restart or plotting, I could not tie up the file space waiting for the output to be printed. The way around this is to rewind the output and route it to a remote output file. When the job is complete, you can view the output by batching it locally and paging it or using one of the text editors. After viewing, route the output to the central site (TID=C) for printing. This way you can view your output without having

the hard copy in your possession. This works very well over the weekends when the computer centers are closed or when the line printer is down.

The last thing I would like to discuss to help the future user of STAGS is some of the different parameters in the STAGS data deck. In viewing Figures A2 and A3, the two data decks are identical through the M2A card, shell geometry. Most of the data cards are self explanatory and the users' manual does a very good job of explaining the card sequence. There were a few cards that caused some confusion for me and I would like to try to prevent a future user from the same confusion.

The first thing to remember is that in the STAGS Data Decks something that is not specified defaults to zero. This can save a lot of time since a lot of the parameters will not have to be input. However, a small mistake can also be very confusing. This will occur when the user thought he input a data field into the computer correctly and the output generated was not expected or there is a different error printed. Therefore, a careful check of the data deck, remembering the default value is zero, will prevent a lot of wasted time.

There were two cards in the data decks that were confusing. They were the D1 Strategy Parameter card and oddly enough the I2 Material Property card. The D1 card has three items on it that are used in the nonlinear solution

algorithm and they require some consideration when choosing them. In the I2 card, the requested Poissons ratio was a different notation than used by most authors.

The three parameters on the D1 cards that are used in the nonlinear solution algorithm are NCUT, NEWT, and DELX. NCUT is the number of times that the solution algorithm can cut the step increment. To pick a good value for this one needs to consider his initial step increment and what he would like as his final step increment. Then NCUT can be calculated by figuring the number of times you have to half the initial step increment in order to reach the final increment. For example, with an initial load step of 10 and NCUT equal to 4 the final load step would be 1.25.

The next parameter to be considered is NEWT. NEWT is the number of times the stiffness matrix can be refactored when there are convergence problems. There is no real easy way to pick a value of NEWT to be used without having some idea of the solution. If the solution is linear, then only one factoring is needed. The greater amount of nonlinearity in the solution the higher the number of refactoring is needed. One should remember though that the general flow for STAGS is to refactor the stiffness matrix first and then cut the step size. Therefore the three factors, NEWT, NCUT, and step size are all tied together. One should also remember that it is very expensive to refactor a large stiffness matrix.

The third factor on the D1 card that also has an effect on the nonlinear solution algorithm is DELX. This is the maximum value that any DOF can have between successive iterations. That is, it is the convergence factor used with the nonlinear algorithm. In essence, DELX is the parameter that dictates the amount of error (residual error) that you want in any given load step and also triggers the program as to whether there are convergence difficulties or not depending on the number of iterations done at that load step. Therefore, all three of the parameters are dependent on the others and only careful consideration and an idea of the solution will be able to lead to good choices.

The last parameter that lead to any confusion was the requested Poisson ratio on the I2 Material Properties card. Most authors in composite material texts and papers use the following relationship between the different Youngs Modulus and Poisson ratio:

$$E_1 = \frac{\nu_{12}}{\nu_{21}} E_2 \quad (1A)$$

However, STAGS has a different relation. It is given as:

$$E_1 = \frac{\nu_{21}}{\nu_{12}} E_2 \quad (2A)$$

In comparing the relations, it can be seen that the Poisson ratios have been switched. When working with STAGS be very careful not to confuse which ratio they want input and which relationship you are usually familiar with. It is just a change of notation for Poisson ratio that is used. Be careful and the best of luck in using STAGS.

TCJ,T3800,IO15000,CM150000. D710554,B0X4279.
LIMIT,7000.
BEGIN,NOSFILE.
ATTACH,STAGS1,ID=D820138,MR=1.
GET,NAP55,ID=JANISSE.
STAGS1,NAP55.
ATTACH,STAGS2,ID=D820138,MR=1.
RETURN,STAGS1.
STAGS2.
REWIND,TAPE22.
REQUEST,NAP5522,PF.
COPY,TAPE22,NAP5522.
REWIND,NAP5522.
CATALOG,NAP5522,RP=180.
REQUEST,NAP5521,PF.
REWIND,TAPE21.
COPY,TAPE21,NAP5521,RP=180.
REWIND,OUTPUT.
ROUTE,OUTPUT,DC=PR,TID=16.

FIGURE A1

STATIC NONLINEAR ANALYSIS 0,+45,-45,90_s

C	8 PLYS .005 INCHES THICK
C	[0,+45,-45,90] PANEL
3,1,3,3	\$B1 NONLINEAR STATIC ANALYSIS
1,0	\$B2 1 SHELL 0 ELEMENTS
1,3,1,3	\$B3 1 MATERIAL 1 SHELL WALL
1.0,10.0,6.0E2	\$C1 LOAD MULTIPLIER RECORD
0,3300,10,10,0,0.000001,1.0	\$D1 STATEGY PARAMETERS
13,13	\$F1 13 ROWS 13 COLUMNS
1,0	\$I1 MATERIAL NUMBER
20.5E06,0.0212439,.75E06,0.0,	
1.0,1.3E06,1.0	\$I2 MATERIAL PROPERTIES
1,1,8	\$K1 WALL CONFIGURATION
1,.005,0.0	\$K2 PLY MATERIAL, THICKNESS,
1,.005,45.0	ORIENTATION
1,.005,-45.0	
1,.005,90.0	
1,.005,90.0	
1,.005,-45.0	
1,.005,45.0	
1,.005,0.0	
5	\$K2 END OF ALL 8 PLYS
0.0,12.0,0.0,57.297795,12.0	\$M1 CYLINDRICAL SHELL UNIT
1,1	\$M2 SHELL GEOMETRY
6.0,28.65,4.0,19.1,.04	\$M5 SHELL WALL RECORD
411	\$M6 IMPERFECTION RECORD
0,0,0,0	\$N1 ELEMENT NUMBER
100,000	\$P1 USER DEFINED BC
110,100	\$P2 U FREE ON TOP
000,000	\$P2 U, V, RU FREE RT SIDE
110,100	\$P2 CLAMPED ON BOTTOM
1	\$P2 U, V, RU FREE LEFT SIDE
1,1.0	\$Q1 1 LOAD SYSTEM
1.0,2,1,1	\$Q2 1 LOAD SET SYSTEM A
1,1,1,0	\$Q3 LOAD DEFINITION
	\$R1 PRINT OUTPUT

FIGURE A2: Data Deck For Panel With Imperfection

STATIC NONLINEAR ANALYSIS 4X4 CUTOUT 0,+45,-45,90_s

C	8 PLYS .005 INCHES THICK
C	[0, +45, -45, 90] _s PANEL
3,1,3,3	\$BI NONLINEAR STATIC ANALYSIS
1,0	\$B2 1 SHELL 0 ELEMENTS
1,0,1,0	\$B3 1 MATERIAL 1 SHELL WALL
1.0,10.0,6.0E2	\$C1 LOAD MULTIPLIER RECORD
0,3300,10,10,0,0.0000001,1.0	\$D1 STATEGY PARAMETERS
13,13	\$F1 13 ROWS 13 COLUMNS
1,0	\$I1 MATERIAL NUMBER
20.5E06,0.0212439,.75E06,0.0,	
1.3E06,1.0	\$I2 MATERIAL PROPERTIES
1,1,8	\$K1 WALL CONFIGURATION
1,.005,0.0	\$K2 PLY MATERIAL, THICKNESS,
1,.005,45.0	ORIENTATION
1,.005,-45.0	
1,.005,90.0	
1,.005,90.0	
1,.005,-45.0	
1,.005,45.0	
1,.005,0.0	
5	\$K2 END OF ALL 8 PLYS
0.0,12.0,0.0,57.2957795,12.0	\$M1 CYLINDRICAL SHELL UNIT
1,0	\$M2 SHELL GEOMETRY
411,0,0,1	\$M5 SHELL WALL RECORD
5,9,5,9	\$N1 ELEMENT NUMBER
0,0,0,0	\$N8 4X4 CUTOUT IN CENTER
100,000	\$P1 USER DEFINED BC
110,100	\$P2 U FREE ON TOP
000,000	\$P2 U, V, RU FREE RT SIDE
110,100	\$P2 CLAMPED ON BOTTOM
1	\$P2 U, V, RU FREE LT SIDE
1,1,0	\$Q1 1 LOAD SYSTEM
1.0,2,1,1	\$Q2 1 LOAD SET SYSTEM A
1,1,1,0	\$Q3 LOAD DEFINITION
	\$R1 PRINT OUTPUT

FIGURE A3: Data Deck For Panel With Cutout

PLOT OF 4X4 CUTOOUT

12,1,6.0,0,0,0
2,1,-1,0,1,15,0,3
.5,0.,0.,28.65,10.,10,3,3
3.0,6.0,9.0
3.0,6.0,9.0
2,1,-1,0,1,15,0,4,0,0,-1
2,1,-1,0,1,15,0,5,0,0,-1
2,1,-1,0,1,15,0,6,0,0,-1
2,1,-1,0,1,30,0,3,0,0,-1
2,1,-1,0,1,30,0,4,0,0,-1
2,1,-1,0,1,30,0,5,0,0,-1
2,1,-1,0,1,30,0,6,0,0,-1
2,1,-1,0,1,62,0,3,0,0,-1
2,1,-1,0,1,62,0,4,0,0,-1
2,1,-1,0,1,62,0,5,0,0,-1
2,1,-1,0,1,62,0,6,0,0,-1

FIGURE A4: Data Deck For STAPL

APPENDIX B

1. Composite Material Parameters
2. Reduced Stiffness Matrix
3. Transformed Stiffness Matrices
4. Extensional Stiffness Matrices
5. Bending Stiffness Matrices

NOTE: All of the panels used in this study had symmetric ply layup, therefore, there is no coupling stiffness matrix (B_{ji}).

1. Material Properties used:

$$E_1 = 20.5 \times 10^6 \text{ psi}$$

$$E_2 = 1.3 \times 10^6 \text{ psi}$$

$$\nu_{21} = .0212$$

$$\nu_{12} = .335$$

$$G = .75 \times 10^6 \text{ psi}$$

$$\text{Note: } \nu_{12} = \frac{E_1}{E_2} \nu_{21}$$

2. Reduced Stiffness Matrix $[Q_y]$.

$$\begin{bmatrix} 20.644 & .43766 & 0. \\ & 1.309 & 0. \\ \text{Sym} & & .75 \end{bmatrix} \times 10^6 \text{ lbs/in}$$

3. Transformed Reduced Stiffness Matrix.

$$[\bar{Q}_{ij}]^0 = [Q_{ij}]$$

$$[\bar{Q}_{ij}]^{90} = \begin{bmatrix} 1.309 & .43766 & 0. \\ & 20.644 & 0. \\ \text{sym} & & .75 \end{bmatrix} \times 10^6 \text{ psi}$$

$$[\bar{Q}_{ij}]^{\pm 45} = \begin{bmatrix} 6.457 & 5.322 & \pm 4.833 \\ & 6.457 & \pm 4.833 \\ \text{sym} & & 5.269 \end{bmatrix} \times 10^6 \text{ psi}$$

4. Extensional Stiffness Matrices $[A_{ij}]$.

The $[A_{ij}]$ is the same for the $[0, +45, -45, 90]_s$, $[0, -45, +45, 90]_s$ and $[90, +45, -45, 0]_s$ ply layup. It is:

$$\begin{bmatrix} .34867 & .11539 & 0. \\ & .34867 & 0. \\ \text{sym} & & .12038 \end{bmatrix} \times 10^6 \text{ lbs/in}$$

The $[A_{ij}]$ is the same for the $[90, 0]_{2s}$ and $[0, 90]_{2s}$ panels, which is:

$$\begin{bmatrix} .43906 & .0175 & 0. \\ & .43906 & 0. \\ \text{sym} & & .03 \end{bmatrix} \times 10^6 \text{ lbs/in}$$

5. Bending Stiffness Matrices $[D_{ij}]$.

$$[D_{ij}]_{[0, +45, -45, 90]_s} = \begin{bmatrix} 77.594 & 12.109 & 4.823 \\ & 19.724 & 4.823 \\ \text{sym} & & 13.767 \end{bmatrix} \quad \text{in-lbs}$$

$$[D_{ij}]_{[0, -45, +45, 90]_s} = \begin{bmatrix} 77.594 & 12.109 & -4.823 \\ & 19.1724 & -4.823 \\ \text{sym} & & 13.767 \end{bmatrix} \quad \text{in-lbs}$$

$$[D_{ij}]_{[90, +45, -45, 0]_s} = \begin{bmatrix} 19.724 & 12.189 & 4.823 \\ & 77.594 & 4.823 \\ \text{sym} & & 13.767 \end{bmatrix} \quad \text{in-lbs}$$

$$[D_{ij}]_{[90, -45, +45, 0]_{2s}} = \begin{bmatrix} 19.724 & 12.189 & -4.823 \\ & 77.594 & -4.823 \\ \text{sym} & & 13.767 \end{bmatrix} \quad \text{in-lbs}$$

$$[D_{ij}]_{[90, 0]_{2s}} = \begin{bmatrix} 39.137 & 2.341 & 0. \\ & 77.717 & 0. \\ \text{sym} & & 4.00 \end{bmatrix} \quad \text{lbs-in}$$

$$[D_{ij}]_{[0, 90]_{2s}} = \begin{bmatrix} 77.717 & 2.341 & 0. \\ & 39.137 & 0. \\ \text{sym} & & 4.00 \end{bmatrix} \quad \text{lbs-in}$$

Vita

Thomas C. Janisse was born on 12 April 1951 in Detroit, Michigan. He graduated from Utica High School in 1969 and attended the United States Air Force Academy Preparatory School which he completed in 1970 and graduated from the United States Air Force Academy in June of 1974 with a B.S. in Engineering Mechanics. He was commissioned as a 2nd Lieutenant in the USAF and attended Undergraduate Pilot Training at Williams AFB AZ. Upon completion of Undergraduate Pilot training, he served as an aircrew member as a C141 pilot at Charleston AFB, SC until January of 1979. He was then assigned back to Williams AFB, AZ as an Instructor Pilot in the T-37. He entered the School of Engineering, Air Force Institute of Technology in June 1981.

Permanent Address: 52138 Staffordshire
Utica, Michigan 48087

UNCLASSIFIED

SECURITY CLASSIFICATION OF THIS PAGE (When Data Entered)

REPORT DOCUMENTATION PAGE		READ INSTRUCTIONS BEFORE COMPLETING FORM
1. REPORT NUMBER AFIT/GAE/AA/82-15	2. GOVT ACCESSION NO. AD-A124 739	3. RECIPIENT'S CATALOG NUMBER
4. TITLE (and Subtitle) A PARAMETRIC STUDY OF SURFACE IMPERFECTIONS AND SMALL CUTOUTS IN A COMPOSITE PANEL		5. TYPE OF REPORT & PERIOD COVERED MASTER'S THESIS
7. AUTHOR(s) Thomas C. Janisse Capt. USAF"		6. PERFORMING ORG. REPORT NUMBER
9. PERFORMING ORGANIZATION NAME AND ADDRESS Air Force Institute of Technology (AFIT-EN) Wright-Patterson AFB, Ohio 45433		8. CONTRACT OR GRANT NUMBER(s)
11. CONTROLLING OFFICE NAME AND ADDRESS		10. PROGRAM ELEMENT, PROJECT, TASK AREA & WORK UNIT NUMBERS
14. MONITORING AGENCY NAME & ADDRESS (if different from Controlling Office)		12. REPORT DATE December 1982
		13. NUMBER OF PAGES 165
		15. SECURITY CLASS. (of this report) UNCLASSIFIED
		15a. DECLASSIFICATION/DOWNGRADING SCHEDULE
16. DISTRIBUTION STATEMENT (of this Report) Approved for public release; distribution unlimited		
17. DISTRIBUTION STATEMENT (of the abstract entered in Block 20, if different from Report)		
18. SUPPLEMENTARY NOTES Approved for public release: IAW AFR 190-17. <i>Lynn E. Wolaver</i> LYNN E. WOLAVER Dean for Research and Professional Development Air Force Institute of Technology (AIC) Wright-Patterson AFB OH 45433 6 JAN 1983		
19. KEY WORDS (Continue on reverse side if necessary and identify by block number) Composite Materials STAGS C-1 Composite Panels Cutouts Nonlinear Analysis Graphite-Epoxy Composites Bifurcation Analysis Plates and Shell Analysis Finite-Elements		
20. ABSTRACT (Continue on reverse side if necessary and identify by block number) See reverse side		

DD FORM 1473

1 JAN 73

EDITION OF 1 NOV 65 IS OBSOLETE

UNCLASSIFIED

SECURITY CLASSIFICATION OF THIS PAGE (When Data Entered)

UNCLASSIFIED

SECURITY CLASSIFICATION OF THIS PAGE(When Data Entered)

A finite element computer code, STAGS C-1, was used to study the effects surface imperfections and cutouts have on the load bearing capability and the displacement patterns of a graphite-epoxy panel. A nonlinear collapse analysis was conducted on two different ply layups each with five different surface imperfection patterns. In addition three different ply orientations were studied each having two different size cutouts (a two inch by two inch square and a four inch by four inch square).

The nonlinear branch of STAGS C-1 uses a energy technique using the nonlinear stiffness matrix that was generated by using the Sanders' strain displacement equations. STAGS did a very good job in calculating the collapse load and displacements of a panel with surface imperfections when compared with an experimentally tested panel.

It was found that as the number of surface imperfections is increased, the collapse load decreases until there are nine surface waves. After that, the collapse load increases with increasing imperfections. An imperfection pattern that models the linear bifurcation eigenvector did not have the lowest collapse load as was believed. The displacement pattern followed the initial surface imperfections in all cases.

The collapse characteristics of composite panels are dependent on the ply layup and size of the cutout. Small cutouts had a displacement pattern that was not expected and is different than the larger cutouts. Changing the vertical boundary conditions on the panel with the small cutout had a negligible effect.

UNCLASSIFIED

SECURITY CLASSIFICATION OF THIS PAGE(When Data Entered)

END